PhD thesis

by

mgr inż. Piotr Olesik

The effect of addition of glassy carbon particles at different grain size on properties of heterophase HDPE matrix composites made by FDM 3D-printing

Supervisor: dr hab. inż. Mateusz Kozioł, prof. Pol. Śl.

Co-supervisor: dr inż. Tomasz Pawlik

KATOWICE 2023

Politechnika Śląska

Wydział Inżynierii Materiałowej

Katedra Technologii Materiałowych

Politechnika Śląska

Składam najszczersze podziękowania dla wszystkich osób, które wsparły mnie w realizacji pracy doktorskiej.

W szczególności chciałbym podziękować Panu ***Profesorowi Dr hab. Michałowi Żelechowerowi****, dzięki któremu mogłem podjąć się pracy naukowej i zawsze służył wsparciem i radą.*

Dziękuję również Pani ***Profesor Dr hab. Inż. Anicie Olszówce-Myalskiej****, za liczne rozmowy i słowa wsparcia oraz zainteresowanie moim rozwojem naukowym.*

Dziękuję również ***Centrum Materiałów Polimerowych i Węglowych PAN****, a w szczególności* ***Pani Dr hab. inż. Urszuli Szeludze*** *oraz* ***Dr inż. Marcinowi Godzierzowi*** *za pomoc w przeprowadzaniu badań oraz wspaniałą współpracę.*

Chciałbym podziękować moim promotorom ***Profesorowi Dr hab. Inż. Mateuszowi Koziołowi*** *oraz* ***Dr Inż. Tomaszowi Pawlikowi****, z którymi współpraca była czystą przyjemnością i bez których praca ta nigdy by nie powstała.*

Serdecznie dziękuję moim przyjaciołom, rodzinie i znajomym, a w szczególności ***Michałowi, Beacie, Aleksandrowi, Agnieszce N. oraz Jakubowi****, którzy zawsze byli gotowi wysłuchać mnie w trudnych chwilach.*

Na koniec dziękuję ***moim rodzicom, Bożenie i Adamowi****,*
którym dedykuję tą pracę.

Table of contents

1. Theoretical background:

1.1. Glassy carbon

1.1.1. Characteristics

Glassy carbon (GC) or vitreous carbon (VC), a unique form of carbon with an amorphous atomic structure, has gained significant attention in various scientific fields due to its exceptional properties and versatile applications. Its good temperature stability, low density, and excellent mechanical and electrical properties make it a valuable material for a wide range of scientific and technological advancements [1]. The term "glassy carbon" was first introduced in 1962 by Yamada and Sato [2]. Back then it referred to "gas-impermeable, not impregnated carbon". Nowadays, it is defined as non-graphitizing amorphous carbon, most often obtained from pyrolysis of phenol-formaldehyde resin [1], [3]. However, it should not be mistaken with other amorphous forms of carbon such as carbon black, activated carbon or carbon dots, due presence of sp^2 hybridization of carbon atoms in glassy carbon structure. The most up to date GC structure model is characterized by curved carbon sheets comprising pentagons, hexagons, and heptagons, along with occasional closed particles and densely packed bunches (Fig. 1) [4], [5]. So far, this explains the unique combination of GC properties. The properties of glassy carbon are presented in Table 1.

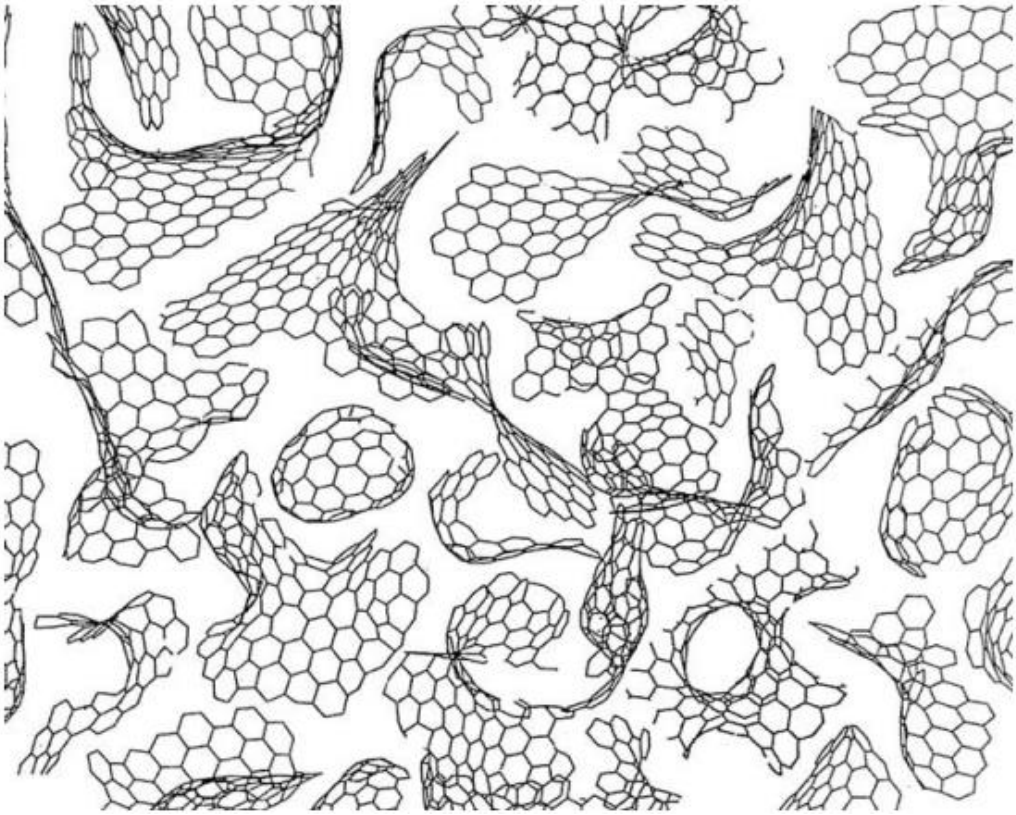

Figure 1 Schematic structure of glassy carbon [4]

Table 1 Properties of glassy carbon

Property	Value
Young's modulus	20 – 40 GPa [3]
Hardness	82.8 HV [6] 4 Moss [2]
Density	1.30-1.55 g/cm^3 [7], [8]
Electrical conductivity	~200 S/m [9]
Thermal expansion coefficient	(2.0–3.4) ×10^{-6} K^{-1} [7]
Thermal conductivity	~10 Wm^{-1}K^{-1} [8]
Refractive index	1.87 (for 620 nm) [10]

Glassy carbons are produced through the pyrolysis of polymer precursors rich in carbon, typically carried out in an inert atmosphere composed of gases such as Ar or N_2 [3], [11]. Glassy carbon is described in the literature as occurring in three alternative forms: bulk or monolithic [12], [13], foams or reticulated vitreous carbon (RVC) [14], [15] and powder or spheres [16]. All mentioned forms can be manufactured at different parameters and from different polymers. In case of bulk GC, Origo et. al [12] obtained monoliths from furfuryl alcohol resin polymerized with different acids as catalysts: *p*-toluenesulfonic monohydrate (PTLS), hydrochloric, sulfuric, nitric, and phosphoric and then carbonized the ingredients at 1200˚C/2h in N_2 atmosphere. They show that different catalysts usage during resin curing leads to different value and morphology of porosity. Similar approach with furfuryl alcohol resin was showed by Passador et. al [17], however lower temperature (1000˚C) and shorter time (30 min) was used. For carbon foams, the high porosity is developed due to usage of blowing agents or supporting spatial structures. Tadyszak and Litowczenko et. al [14] proposed a method of obtaining carbon foams from sucrose as a carbon source and NH_4Cl as a blowing agent. They pyrolysed the ingredients at 1100˚C/2h in Ar atmosphere. Cellular structure was obtained. By changing a ratio between sucrose and ammonium chloride, different strength and thickness of the cell walls can be obtained. In contrast, Myalski and Hekner [15] presented a method in which glassy carbon from phenol-formaldehyde resin was made. The carbon foam was obtained by infiltrating polyurethane foams with different ppi (pores per inch). In this approach a pyrolysis was performed in stages with different heating rates, which ensures distribution and separation of all the compounds in the precursor material. In case of GC powder or spheres two approaches can be found. The first one uses dry spraying process to form particles and spheres. Levendis

and Flagan [16] showed a procedure in their publication of obtaining particles with diameters from few micrometres up to 200µm. In their study, they sprayed mixture of furfuryl alcohol in acetone with various blowing agents. The final carbonization was held at 1500 K in N_2 atmosphere. The second approach is simple milling of monolithic GC [18] or RVC [19]. The reported particles sizes were approximately 100µm and 160µm, respectively.

1.1.2. *Applications of glassy carbon*

The glassy carbon has a range of potential applications. In the reviews [1], [3], [20], the usage in the biomedical, pharmaceutical, electronic, micro- and nanomanufacturing and energy sectors were described. The GC's applications have evolved as a potential material for specialized crucibles [7]. However, how Uskoković described in his historical review [1], currently, the most popular use is in electrochemistry, with special reference to electrodes [21]. One of the first described use of GC as an electrode was in 1965 by Zittel and Miller [22], when they used it in voltammetry. They proposed this material due to its high chemical resistance to strong acids and oxidizing agents. Over the years, the GC established its presence in chemistry as reliable material, i.e., Simka et al. [23] used GC as a counter electrode in investigating black TiO_2 coating doped with Ni and Cu as a working electrode. The widespread usage of GC electrodes even motivates the investigations on corrosion under electrochemical oxidative conditions, which occur under oxygen-involving reactions like oxygen reduction reaction (ORR) and oxygen evolution reaction (OER) [24]. Also, a popular procedure in electrochemistry is surface modification of GC electrodes. This broadens up the usage of GC, e.g., detection of organic compounds [25], catalyst for fuel-cells [26] or energy storage [27]. The biomedical applications are the second popular research topic concerning GC applications. Most of them revolve around sensing and detection using GC electrodes; however, some of them utilize biocompatible property of GC (Fig. 2) for tissue engineering [28], [29] or drug delivery [30].

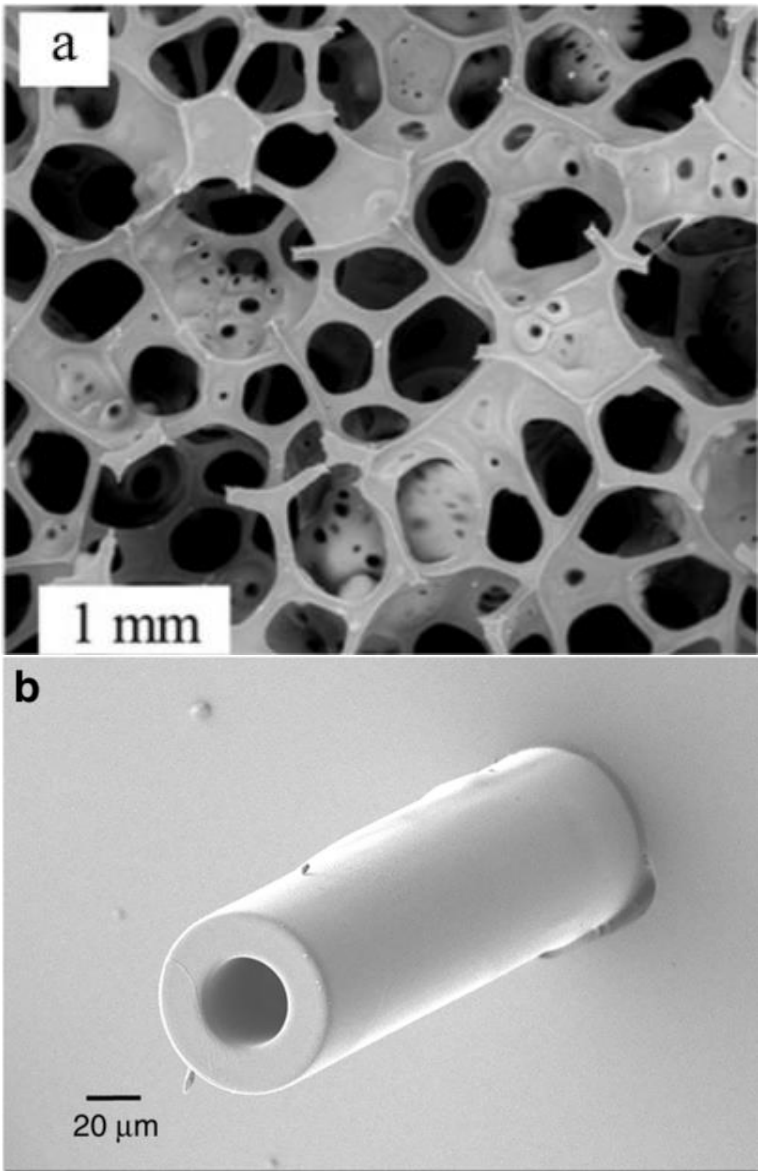

Figure 2 Examples of GC applications in medicine: a) tissue scaffold [29]*, b) microneedle* [30]

1.1.3. Glassy carbon composites

The niche application of glassy carbon that can be observed in research fields is a participation in composite materials. GC can be utilized as reinforcing component, enhancing properties of the composite. Several distinct types of composites containing GC can be found (Fig. 3). Historically, the first two research was made by Hokoa et al., presenting the composites of GC with graphite [6] and diamond [31]. In those publications, GC is used as a matrix for respectively graphite and cluster diamond particles. The composites exhibit lower coefficient of friction (CoF) than base material and self-lubricating property. In the next years, the two main groups of composites, where GC was used as a reinforcement, can be distinguished – metal matrix composites (MMCs) and polymer matrix composites (PMCs).

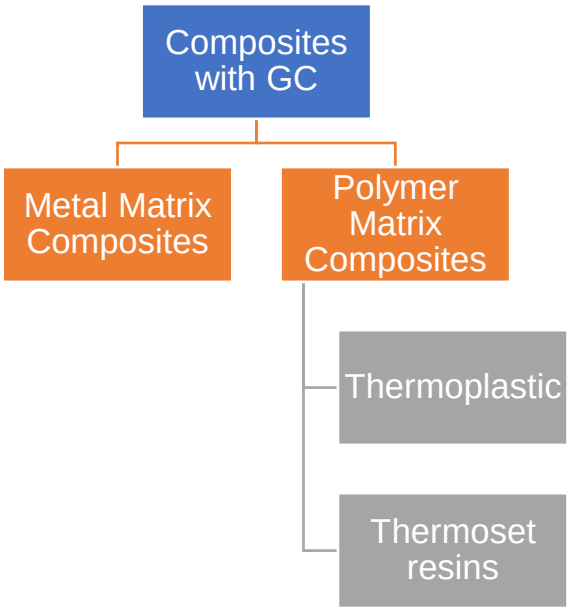

Figure 3 Types of composites with GC

In case of MMCs, the several different matrices were used with both glassy carbon particles and foams as a reinforcement. Probably, the biggest contribution in this topic is from teams of Olszówka-Myalska et al. and Myalski et al., where magnesium matrix composites [18], [32]–[35] and aluminium matrix composite [36]–[38] was investigated. For the magnesium-based composites, the ones reinforced with particles and carbon foam were obtained and impact on properties and wear resistance was investigated. The authors proposed material for biomedical applications which contribute to mentioned previously trend [33]. They showed that GC can improve hardness, compressive strength, and wear resistance of pure magnesium. However, the manufacturing procedure (gravity casting/pressure die casting) highly affects the obtained properties. In case of aluminium matrix composites, the authors investigated GC as skeleton reinforcement for wear applications. In their research, glassy carbon as coating for alumina foam and as RVC was obtained [37], [39]. The glassy carbon decrease wear rate and CoF of aluminium alloy matrix. Also, the temperature profile on cast iron pin used in one research is also lower due to self-lubricating properties of glassy carbon. For MMCs, Juszczyk et al. [40] present the research, in which the composites with GC particles in CuSn10 and CuSn10PTi2 was investigated. The composites prepared with powder metallurgy and stir casting was examined and in both cases improved tribological properties. In some cases, even quick stabilization of CoF is visible.

For the PMCs, several research of thermosets resin based [15], [41]–[44] and thermoplastic based [13], [17], [19], [45]–[48] composite can be found in literature. The first research of Pusz et al. [43], in which epoxy resin with 10 wt.% of GC was examined, the increase of thermal stability and stiffness was reported. Later, Szeluga et al. [42] reported epoxy resin composites with GC and multi-walled carbon nanotubes (MWCNTs). The composites with 10 wt.% of GC exhibit higher tensile strength and significantly lower resistivity, while composites with GC and MWCNT has lowest value of resistivity and increase of T_g. The use of GC skeleton (foam derived) reinforcement for epoxy resin was reported by Myalski et al. [15], in which an increase of compressive strength was reported. Recently, Myalski and Posmyk [49] reported use of composite coating phenolic resin with GC (30 wt.%) on steel push rod of the internal combustion engine. The composite coating proves to protect sliding contacts against seizure in case of lubrication failure at unit pressures up to 8 MPa in laboratory tests, which extends the last stage of flight time of the aircraft. Also, Szeluga and Myalski et al. [44] showed epoxy-based composites with GC skeleton reinforcement with comparison to powder reinforcement. They showed that skeleton reinforcement allows to obtain similar tribological properties like composites reinforced with 10 wt.% of GC particles. Finally, Kumar and Sharma [41] showed result where GC was incorporated to 3D printing application. They used photo-crosslinkable poly(ethylene glycol) diacrylate (PEGDA), which is biocompatible polymer for tissue engineering. The addition of GC once again decreased wear force, hence friction coefficient, and wear of produced parts with only up to 5% of GC. Also, the increase of mechanical properties was reported.

The research on GC as reinforcement for thermoplastic polymers is quite a recent interest. In 2019, Santos and Passador et al. published research where the increase of tensile strength and young's modulus for low-density polyethylene (LDPE) was reported [19]. Later, Oyama and Passador et al. reported a use of GC in LDPE anti-static packing. They reported a significant decrease of resistivity and water-vapor permeability with increase of tensile strength [17]. Passador et al. reported related results for PP/EVA blend and poly(hydroxybutyrate-co-hydro-xyvalerate) (PHBV) [47], with similar results as for LDPE. In the case of tribological application, Myalski, Olesik and Godzierz examined PA6/GC composites. From this research, the increase of hardness and decrease of CoF [46]. Also, presence of GC particles promotes debris formation in PA6, which is beneficial for wear resistance, especially after recrystallization of α-phase.

1.2. HDPE composites

1.2.1. *Ceramic reinforcements*

High-Density Polyethylene (HDPE) is a versatile thermoplastic known for its strong molecular structure and high strength-to-density ratio. It is widely used in various industries due to its excellent chemical resistance, good impact resistance, and low moisture absorption properties. HDPE is commonly found in applications such as plastic bottles, pipes, containers, and packaging materials. Even more advanced uses such as bearings, prosthetic components, electrical insulation, or conductive layers can be found [50]–[52]. However, due to its lower strength and stiffness, in comparison to more advanced polymers, i.e.: polyamide (PA), Polyoxymethylene (POM), polyether ether ketone (PEEK), those applications are limited. To improve the desired properties of HDPE, the various fillers or reinforcements can be used. Depending on potential application a different reinforcement type can be used. For example, most study use ceramic particulates or fibres such as: hydroxyapatite [51], alumina [51], [53], zirconia [54], [55], nanoclay [56] or glass fibres [57] to increase both mechanical strength and wear resistance of HDPE. Even the use of natural reinforcements (not always ceramic) is reported by scientists. Salem et al. [58] researched the addition of MoS_2, cuttlebone and red coral to increase wear resistance after hygrothermal aging. They conclude that MoS_2 and red coral decrease both CoF and wear rate for HDPE composites under water lubricated friction. On the other hand, Mazur and Kuciel et al. [59] reported over twice high improvement on tensile strength and 6-times improvement of flexural strength by addition of basalt fibres to green HDPE more than double the improvement in tensile strength and a six-fold improvement in flexural strength after the addition of basalt fibres to green HDPE. The improvement in strength was even after 30 days of hydrothermal aging. The above-mentioned features are important for medical applications and wear applications. However, HDPE composites can exhibit more sophisticated properties. Kaczmarek and Królikowski et al. [60] reported piezoelectric composites of HDPE and MDPE (medium-density PE) with aluminosilicates (Sillikolloid P87) for microelectronic applications. They produced thin films of composites that, in case of HDPE-based material, exhibit piezoelectric charge density at 300 pC/cm^2 for non-oriented samples and 500 pC/cm^2 for oriented ones. Another example is HDPE composites with magnetic and gamma ray shielding properties reported by Reda et al. [61]. They prepared nanocomposites with α-Fe_2O_3 and Al particles using melt-mixing, followed by hot-pressing. The material has a soft-magnetic properties and higher mass attenuation of γ-ray than neat HDPE. Antibacterial

composites with nanoclay and nano silver was presented by Sanchez-Valdes [62]. The composites exhibit 99% of E. coli growth inhibition and ~80% for A. nigger bacteria.

1.2.2. Carbon fillers

Noticeably researched reinforcements for HDPE are carbon-based ones, such as carbon nanotubes, graphite or graphene and graphene oxides [48], [56], [63], [64]The HDPE-carbon composites often exhibits good wear properties and enhances both electrical and thermal conductivity of neat HDPE. In last 20 years, around 400 publications containing “HDPE” and “carbon” keywords can be found on Scopus [21]. For the wear application, composites reinforced with carbon-based materials most often exhibit a combination of low specific wear rate with an increase of mechanical properties such as tensile strength and Young’s modulus. Kamel and Dabees et al. reported HDPE/MWCNT composite for gears [65]. They obtained high thermal stability and mechanical strength at 2.5 wt% addition of MWCNT. Also, they reported decrease of mass wear loss and lower or even lack of deformation of spun gear in compared to neat HDPE. Faisal [66] showed composite with graphene oxide (GO) for orthopaedic implants, which exhibit higher fatigue life and lower wear depth than neat HDPE. Dong and Yuan et al. [67] reported a self-lubrication ability of HDPE composites with 1.5 wt% of graphene nanoplatelets. They suggest that an optimal amount of carbon nanofiller is needed to exhibit a stable formation of a tribo-film under dry and water-lubricated conditions against Si_3N_4 ball. Another mechanism of friction presented Tangpong et al. in [68], [69] where silane coated carbon nanofibers were used. They evaluated wear performance in dry condition against stainless steel ball. They concluded that decrease of CoF and specific wear rate was a result of matrix cracking prevention by carbon fibres. In the case of conductive polymer-matrix composites (CPC), the aim is to obtain a conductive percolation path that can effectively transfer electric charges. For the HDPE/graphite, Zhang et al. [70] reported the volume content at which formation of conductive path was achieved (percolation threshold) – it was about 20%. However, Hoang et al. [71] showed composites with MWCNT with percolation threshold at around 1.2 vol%. Such composites can be applied to microelectronic applications. Another example of composites with increased conductivity usage might be weld joints. Mamunya et al. [72] presented a HDPE composite with segregated carbon black and micrometric carbon fibres. They used the pyroresistive properties of carbon fillers to achieve composite welded joint with enhanced heating kinetics for resistance welding.

1.2.3. 3D printing of HDPE

Due to the rapid development of 3D printing technique, more and more materials is investigated for this technolgy, and more applications can take advantage from it. For thermoplastic materials, the most popular method is Fused Deposition Modeling (FDM). In this method a thermoplastic filament is fed by an extruder into a hot end. Then is pushed through heated nozzle and deposited on (usually also heated) bed. Nowadays, the accessibility of FDM 3D printed is higher than ever, allowing manufacturing in all fields. From in-home at demand elements (i.e., doorknobs, hooks, containers) to medium scale production (i.e., board games elements, face cover masks). Even more advanced applications in automotive, medicine, sport, or architecture [73] are possible. One of the examples can be found in the research of Haryńska et al. [74], in which biocompatible polyester was evaluated for cytotoxicity. They confirmed that material is a valid choice for tissue engineering. The other can be a review of Cholleti [75], where several different Polyvinylidene Fluoride (PVDF) based composites are described. However, one of the most interesting materials for FDM filaments is HDPE. This quite common material still is not easily available on a large market of FDM filaments. The reason is many defects and challenges that come when HDPE is printed. Mülhaupta et al. [76] published work in which they describe many challenges in printing HDPE. The most important challenges are adhesion to build plate (heated bed) and warping (lifting of print's corners or edges during printing, Fig. 4a). In their work, they showed that most popular build plate surfaces do not work for HDPE and specially designed surfaces are necessary. Nonetheless, there is noticeable interest of many scientists in 3D printing HDPE and HDPE-based composites. Barba et al. [77] reported a HDPE composite filament with grafted cellulose fibres. They achieved 25% increase in Young's modulus for the filament and showed example 3D printouts. Vidakis and Petousis et al. [78] published work in which they examined HDPE/nanoTiO_2 composites that were 3D printed. The material exhibited enhanced mechanical strength (both tensile and flexural) with hardness increase. Also, FDM 3D printing of HDPE composites with carbon fillers was reported. Kumar and Doddamani et al. [79] investigated HDPE/MWCNT composites for a 3D printing. They reported an overheating issue (Fig. 4c) in 3D printing and an increase of tensile strength, Young's modulus, and flexural strength. Also, the thermal stability was enhanced even at low concentrations of carbon filler. Freeman et al. [80] reported a 3D printing HDPE composite with phase-change material (PMC). In their work, the composite with 40 wt% of PMC had a better printability, than pure HDPE, especially concerning print adhesion. Also, their material is capable of thermal energy storage. A research team of Horst et al. [81] presented results of electrical conductivity for various nanocomposites based on most of popular

thermoplastic materials. Among several researched materials HDPE composites with 15 wt.% of carbon black, CNT, and graphite, showed reliably low electrical resistance. In case of wear resistant application, only composites based on ultra-high molecular weight polyethylene (UHMWPE) was found. The research team of Panin et al. [82], [83], presented two studies with 3D printed parts made from blend of UHMWPE, HDPE, and polypropylene (UHMWPE/17wt% HDPE-g-VTMS/12wt% PP). They used modified FDM method, which uses powder rather than filaments. They reported a good tribological properties, which are comparable to parts made by hot-pressing. The 3D printing parameters reported in literature are presented in Table 2.

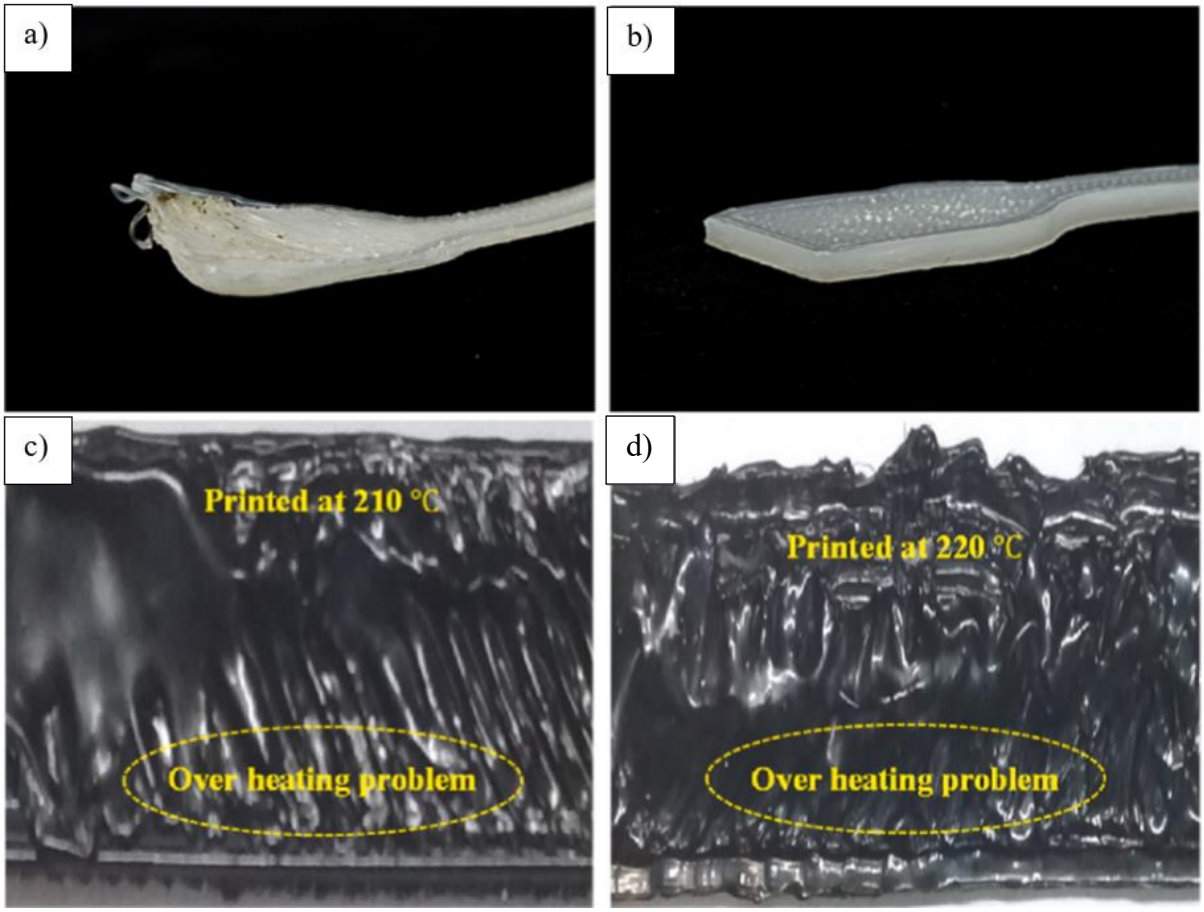

Figure 4 Challenges of 3D printing HDPE: a) warping, b) lack of warping[76]*, c) and d) overheating* [79]

Table 2 3D printing parameters of HDPE filaments – literature reports

Parameter	Value
Filament diameter [mm]	1.75 [78], [80], [81] 2.85 [76], [79]
Temperature [˚C]	200 – 220 [79] 250 [78] 180 – 240 [81] 200 – 240 [76]
Layer height [mm]	0.3 – 0.5 [79] 0.2 [76]
Printing speed [mm/s]	25 – 30 [79] 25 – 150 [76] 10 [81] 20 [80]
Bed surface	SEBS/HDPE plate [76] HDPE plate [80] HDPE tape [84]

1.3. Summary

From above literature review, a few conclusions can be drawn. **First, glassy carbon is still a material that has a great interest among scientists**. The material has the potential to be used in medical application and its potential for use in polymer matrix composites is not still fully recognized. Especially in thermoplastic matrix composites, where **only one research group managed to report producing a material reinforced with it**. Also, **HDPE as potential candidate for medical and microelectronic applications might be a good matrix for making composites filled with glassy carbon.** Moreover, the significant advancement and interest in **3D printing shows a potential for composite filaments based on HDPE and GC**. Basing on trends and various publications, two main types of composites might be considered as a research gap. The first is wear-resistant 3D printing part for medical applications. The second embraces 3D printed elements with enhanced conductivity and/or special physical properties (i.e., piezoelectric properties). Such composites often have **heterophase reinforcements** (at least two different types of reinforcement) to obtain materials with the most suitable properties. The reinforcing phases combination also shows a high scientific potential.

2. Aim of work

With the conclusions from the literature review above as a foundation, the subsequent **thesis of the work** has been formulated:

It is possible to make HDPE/GC composite filaments for FDM 3D printing and to obtain printouts with special tribological and piezoelectric properties.

The aim of the work is ***to perform original research in terms of HDPE-matrix composites containing GC, alone and as heterophase with nano Al_2O_3 and nano SbSI (antimony sulfoiodide), in two aspects:***

1. ***The scientific aspect:***
   - ***Analysing the influence of glassy carbon particles size and distribution on HDPE matrix composite properties, fabricated by FDM 3D printing.***
   - ***Analysing the role of GC as an addition in HDPE matrix composites filled with nano Al_2O_3 and nano SbSI.***
2. ***The practical aspect:***
   - ***Determining technological conditions for fabrication of HDPE/GC composites.***
   - ***Determining technological conditions for fabrication of heterophase HDPE composites containing nano Al_2O_3 and GC, and their wear resistance.***
   - ***Determining technological conditions for fabrication of heterophase HDPE composites containing nano SbSI and GC, and their piezoelectric properties.***

To achieve the above goals, the **research plan** has been developed - presented in Fig. 5. The planned research investigates the impact of GC grain size and distribution on the properties of homogenic and heterophase composites. Two distinct types of GC grain size (micrometric and submicrometric) were employed. The composite for wear application used nano-alumina, one of the most popular materials for wear-based medical applications. The composite intended for microelectronic applications used SbSI nanowires xerogel which was selected due to its reported promising functional performance with various polymer matrices [85]–[88].

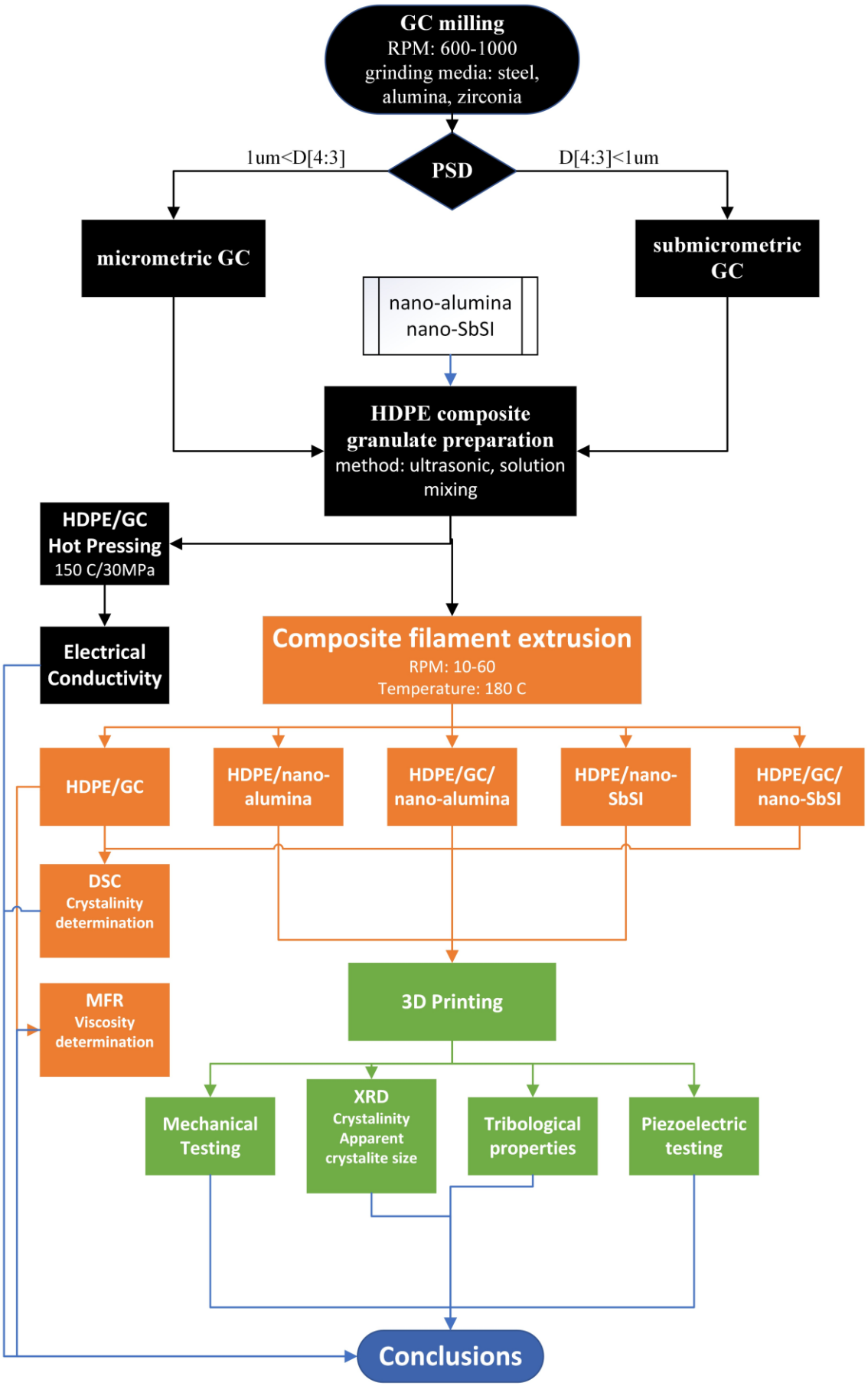

Figure 5 Research experiment plan

3. Experimental part:

3.1. Milling of glassy carbon

3.1.1. Milling methodology

The GC component was prepared by milling methods. The feedstock for preparing the component were fragments of GC foams. The GC foam (Figure 6a) was prepared by prof. Jerzy Myalski via high-temperature pyrolysis. The process of producing GC foams was described in detail in [15]. The obtained GC foams was initially crushed in agate mortar into fine cullet (Figure 6b) and later subjected to milling.

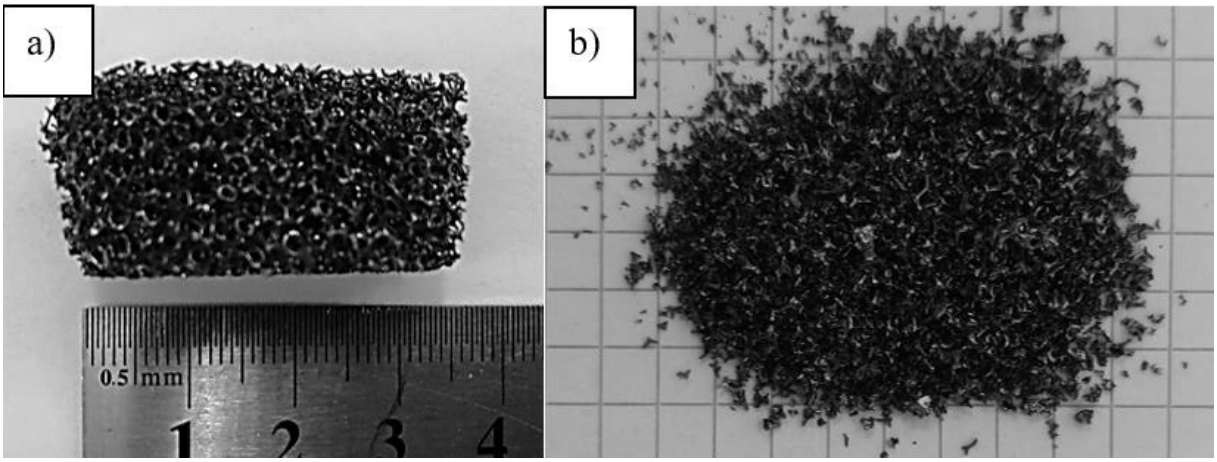

Figure 6 Macrograph of glassy carbon: a) foam, b) crushed foam

A goal of the milling process was to obtain GC powder with two different grain sizes: micrometric and submicrometric. The **micrometric** powder was characterized by the mean diameter ($D_{4/3}$) between 1.0 µm and 20.0 µm. The powder characterized by the mean diameter ($D_{4/3}$) between 0.1µm to 1.0 µm was designed as the **submicrometric** one (sµGC). To achieve a desirable grain size, a different milling approaches was used. Assessed milling procedures was involving a usage of high-energy planetary mill with steel grinding balls, attritor mill with Si_3N_4 grinding balls and high-energy planetary mill with ZrO_2 grinding balls. The equipment used for the research was: Fritsch Pulverisette 6 with steel chamber (V=500 ml), Szegvari Attritor System with Teflon chamber (V=1000 ml) and Fritsch Pulverisette Premium Line 7 with alumina chamber (V=80 ml). The impact of milling parameters such as: time, ball-to-powder ratio, addition of liquid and grinding balls' size were considered. The overall tested milling procedure is presented in Table 3. In this part, parameters were evaluated or adjusted until obtaining desirable grain size of glassy carbon. As a feedstock for milling was used crushed GC foam as mentioned previously, however only for milling to µGC powder. More

specifically, for milling at Pulverisette 6 and Szegvari Attritor. The feedstock for milling to sμGC (at Pulverisette Premium 7) was the μGC powder obtained previously.

Table 3 Milling parameters.

Parameter	Pulverisette 6	Szegvari Attritor	Pulverisette Premium 7
RPM	600	300	1000
Grinding media	10 mm steel	3 mm Si_3N_4	1.75 mm ZrO_2
Ball-to-Powder mass ratio	4:1	2:1	10:1
Condition	Dry	Distilled Water Ethyl alcohol (99.8%)	Dry Ethyl alcohol (99.8%)
Time	0.5h – 2.5h	2.0h – 20.0h	1.0h

3.1.2. Research methodology

The particle size distribution was characterized using laser diffraction method on Malvern MasterSizer3000 device in water conditions. The measuring procedures was as follow:

1. Mixing the powder with 10 ml of distilled water.
2. Deagglomeration in ultrasonic cleaner for 15 min.
3. Addition of deagglomerated mixture to measuring system until achieving 7-9% obscuration rate.
4. Five consecutive measures under mixing with 1250 RPM.
5. Ultrasonic treatment for 5 min in measuring system.
6. Five consecutive measures under mixing with 1250 RPM.

The powders morphology was characterized with use of Hitachi S-3400N and Quanta FEG 250 scanning electron microscopes (SEM). The accelerating voltage was 15 kV and 10kV, respectively. The powder samples were immobilized at conductive substrate with acrylic glue.

The obtained powder density was measured with pycnometer method according to PN-EN ISO 18753:2017-10 standard. The powder density was calculated using following equation:

$$d = \frac{(m_2 - m_1)d_0}{(m_2 - m_1) - (m_4 - m_3)}$$

Where: d – density of glassy carbon powder [g/cm^3], d_0 – distilled water density at 20˚C (0,9982 g/cm^3), m_1 – mass of dry pycnometer [g], m_2 – mass of pycnometer with powder [g], m_3 – mass of pycnometer with water [g], m_4 – mass with pycnometer with water and powder [g]

3.1.3. Results - grain size distribution

The results of grain size distribution are presented at Figures 7-10 and parameters of selected powders are presented in Table 4. In the graph presenting impact of milling time with Pulverisette 6 (Fig. 7) is visible that most optimal is 1.0 h of milling. The prolonging of milling time increases only tendency for powder agglomeration. Similar grain size distribution was obtained by milling for 8h in water condition and 2h in ethyl alcohol at Szegvari Attritor (Fig. 8 and Fig. 9). Comparing these three powders together leads to conclusion that all of them can be used as micrometer glassy carbon powder reinforcement (μGC). However, in this work, powder milled at Szegvari Attritor for 8h in water condition was chosen as most suitable. The decision was motivated by bigger load size and less expensive liquid medium in case of Attritor mills.

The submicrometric glassy carbon powder was made at Pulverisette Premium 7. The impact of milling condition (dry and ethyl alcohol) was investigated. The Fig. 10 shows that usage of alcohol as a milling medium ensured elimination of fraction around 10.0 μm. However, to get desirable effect, the volume ration of ethyl alcohol to GC had to be around 1:0.28. Also, the 1 ml of alcohol had to be added to the bulk every 20 min of milling in order to balance the evaporation effect. In this work, the milling in Pulverisette Premium 7, in ethyl alcohol condition, was chosen as procedure of obtaining submicrometer glassy carbon (sμGC) powder.

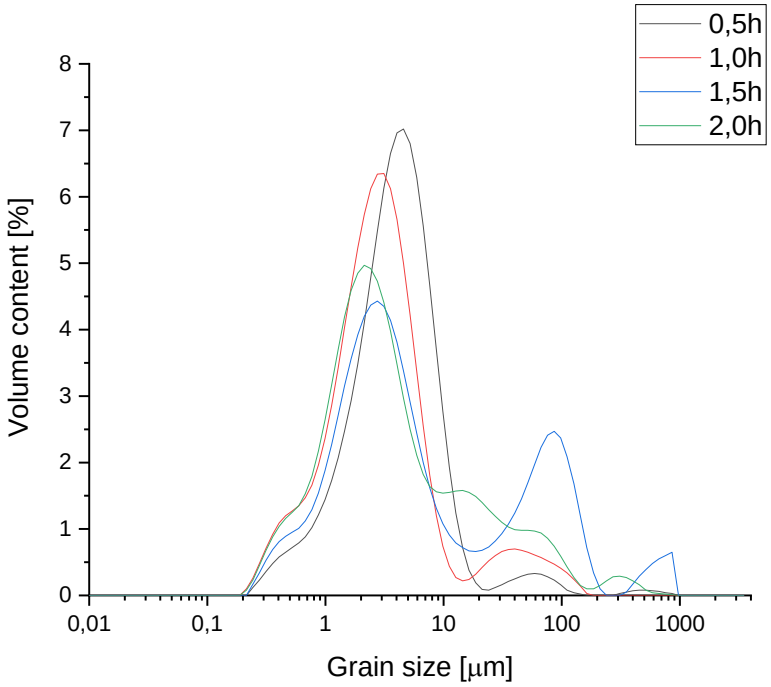

Figure 7 Grain size distribution of GC powder after milling with Pulverisette 6

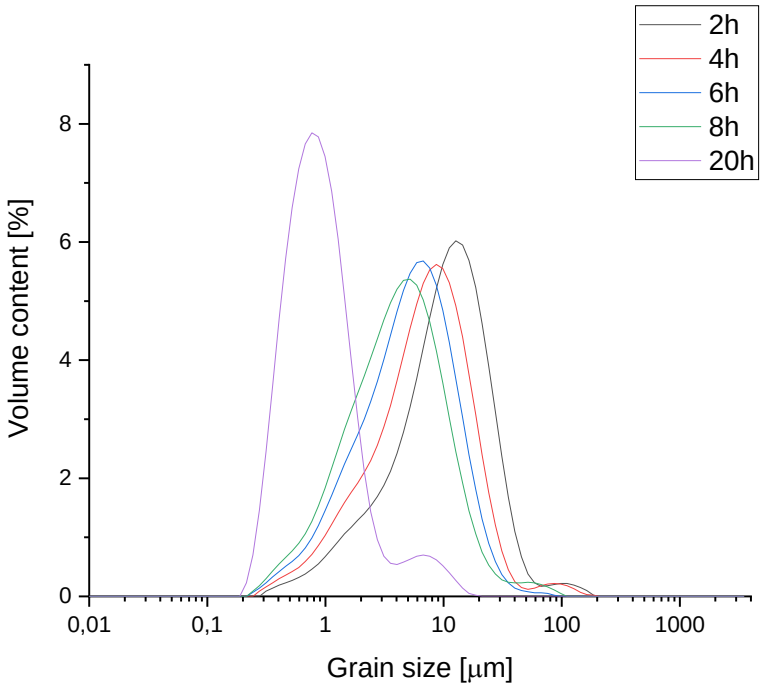

Figure 8 Grain size distribution of GC powder milled with Szegvari Attritor in distilled water.

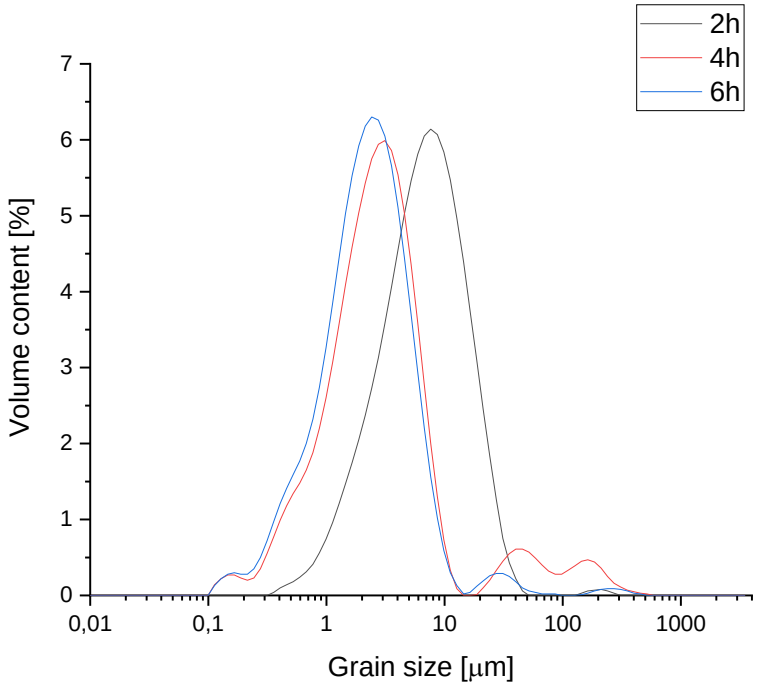

Figure 9 Grain size distribution of GC powder milled with Szegvari Attritor in ethyl alcohol.

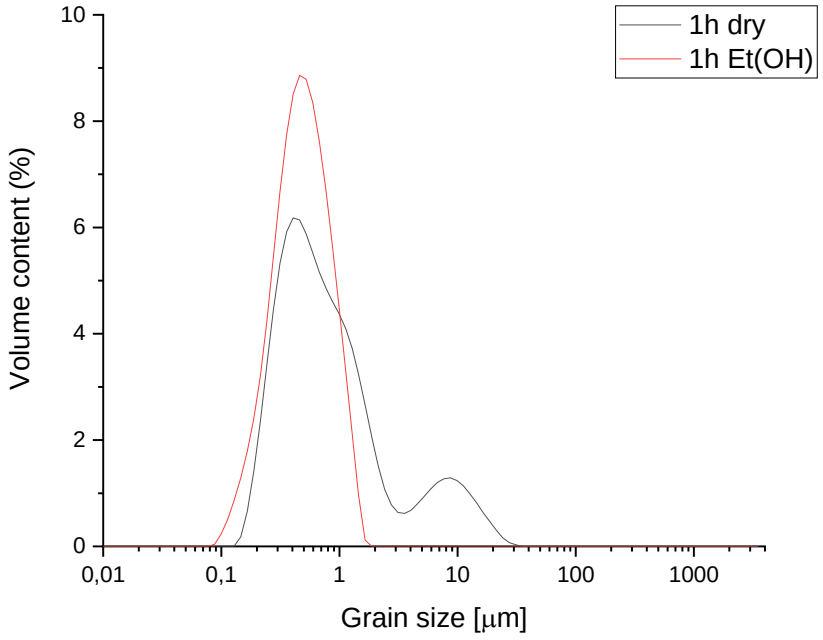

Figure 10 Grain size distribution of GC powder milled with Pulverisette Premium 7

Table 4 Selected GC powders parameters

Sample name	D_{10}* [µm]	D_{50}** [µm]	D_{90}*** [µm]	$D_{4/3}$ [µm]
Attritor 2h in ethyl alcohol	2.11	7.18	19.0	9.77
Attritor 8h in distilled water	1.40	4.21	10.4	5.17
Pulverisette 6 for 1h	0.896	2.82	7.58	5.62
Pulverisette 7 Ethyl alcohol	0.24	0.51	1.02	0.576
Pulverisette 7	0.417	1.54	13.2	4.33

* **the particle diameter particle diameter corresponding to 10% volume on cumulative distribution curve**
** **the median particle diameter**
*** **the particle diameter particle diameter corresponding to 90% volume on cumulative distribution curve**

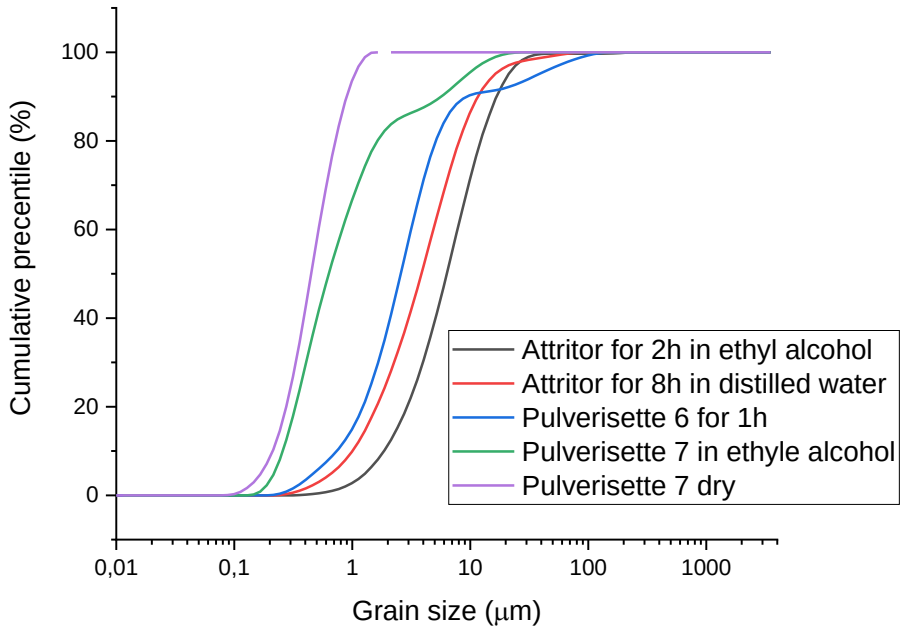

Figure 11 Cumulative curve for selected GC powder

The morphologies of obtained GC powders are presented in Figure 12-13. The particles (grains) show sharp edges and ununiform shape. Such morphology is typical for a brittle nature of amorphous materials, and it is a result of fracturing during milling process. The two-step procedure with smaller grinding balls and presence of ethyl alcohol leads to formation of smaller powder grains. This is caused by two phenomena: an increase in the frequency of collisions between the grinding media and the powder grains, and more efficient (in comparison with the one-step procedure) removal of adhered powder particles from the chamber walls. The latter effect hinders the occurrence of the cushioning phenomenon, which prevents further grinding by reducing ball energy [89]. The measured glassy carbon density was 1.78 g/cm^3, which is slightly higher than usually reported in literature [2], [3].

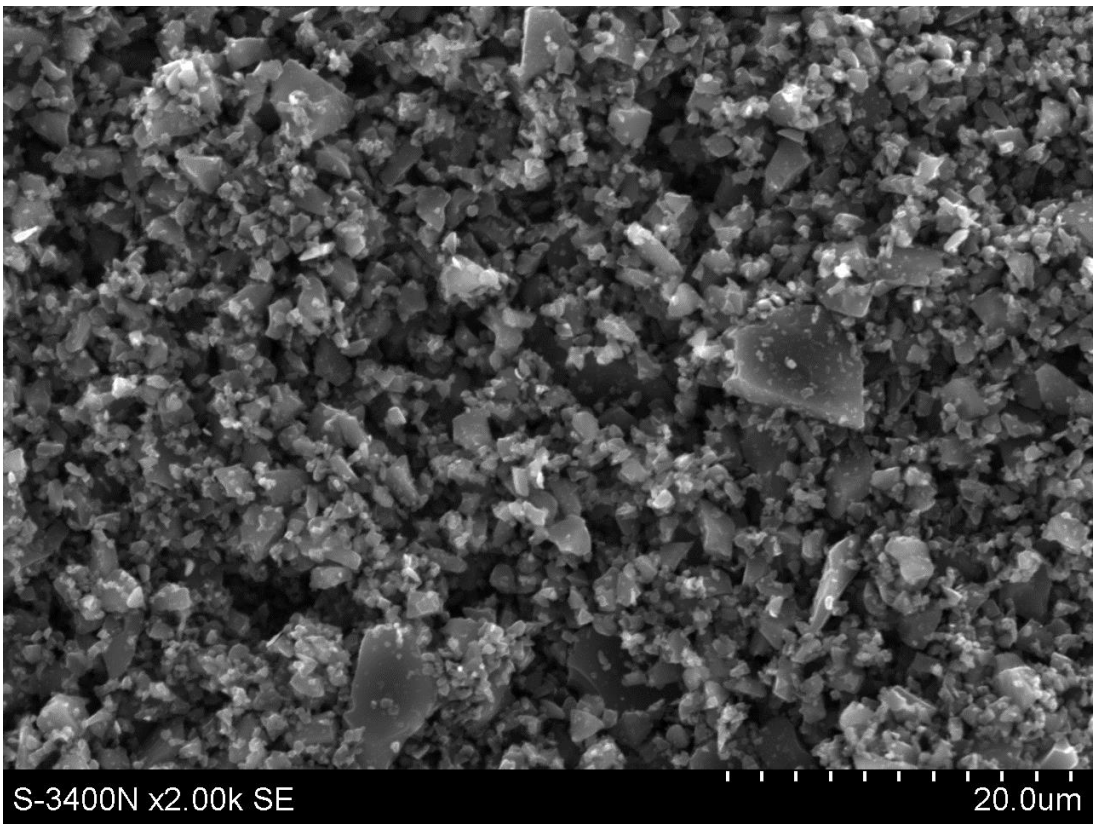

Figure 12 SEM micrograph of micrometric GC powder morphology

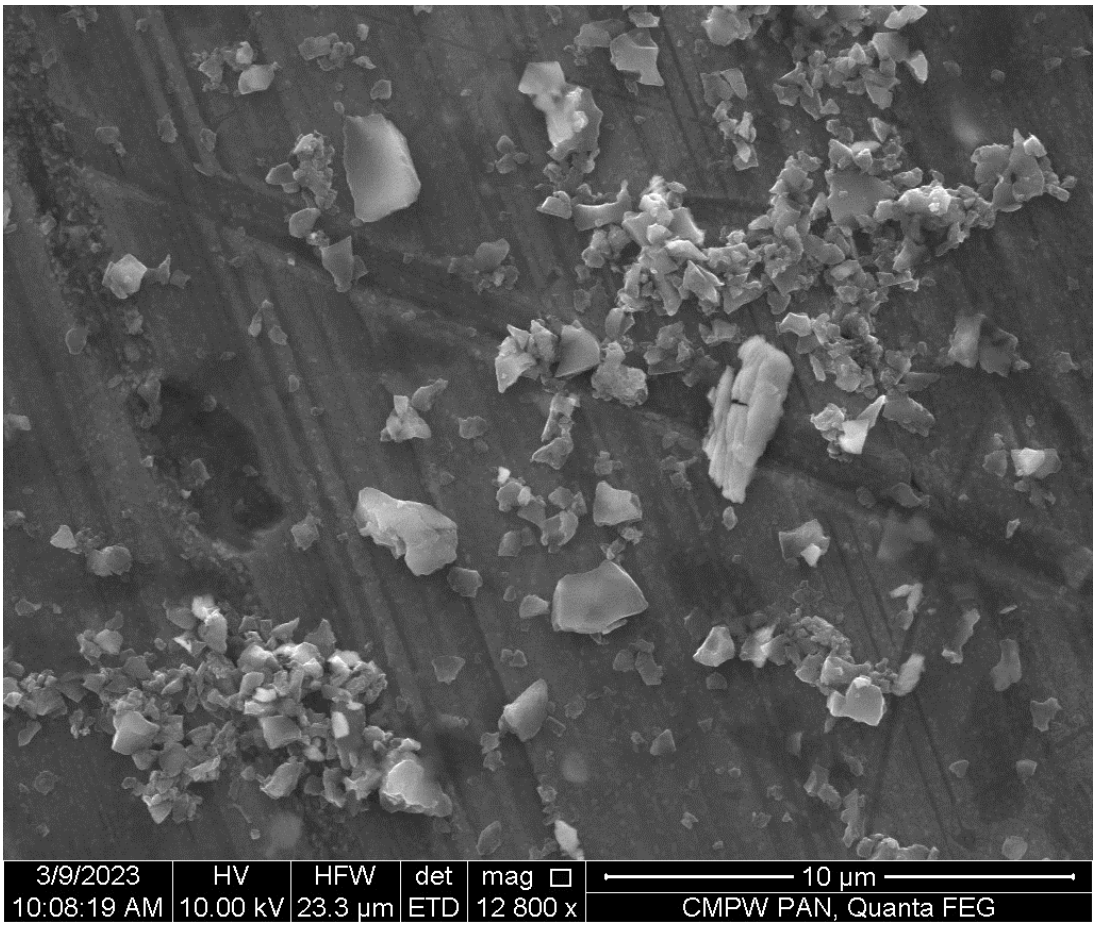

Figure 13 SEM micrograph of submicrometric GC powder morphology

3.2. Composites for tribological applications

3.2.1. Material preparation

The composites containing μGC and sμGC was prepared alongside with composites containing nano-alumina (n-Al_2O_3) and reference neat HDPE. As a matrix for the composites HDPE HIVOREX 2600J (Lotte Chemical, Seoul, South Korea) was used. The properties of the material according to producer are listed in Table 5. For heterophase composite preparation, nano-alumina (product number: 544833, Merck KGaA, Darmstadt, Germany) with <50 nm particle size was used.

Table 5 Properties of HDPE HIVOREX 2600J by Lotte Chemical

Properties	Test method	Value
Melt Flow Index	ASTM D1238	20 g/10 min
Density	ASTM D1505	0.959 g/cm^3
Tensile Stress (Yield)	ASTM D638	24.5 MPa
Tensile Strain (Break)	ASTM D638	> 300%
Flexural Modulus	ASTM D790	1.275 MPa
Notched Izod Impact Strength (23°C)	ASTM D256	0.4 J/m
VICAT Softening Point	ASTM D1525	120˚C

The granulate for extrusion process was prepared by covering HDPE granules with respective powder reinforcements during specially conducted mixing process. The amount of reinforcement necessary to cover a surface of granule was calculated by Eq. 1. Calculations was performed only for μGC powder and basing on that result, the matrix-to-reinforcement volume ratio was set. During mixing, a slight excess of reinforcement material was added to compensate for losses and underestimations. The procedure of mixing HDPE granulate with powder reinforcement was as follow:

1. Weighting the appropriate amount of components.
2. Adding components to a beaker.
3. Filling the beaker with 96% ethyl alcohol until all components soaked.
4. Ultrasonic mixing for 15 min.
5. Pouring the mixture into separate polypropylene container.
6. Drying in 50.0˚C to remove excess of alcohol.

7. Mechanical mixing for 1 minute.
8. Drying in 50.0˚C until alcohol evaporation.

$$M_{\mu GC} = \frac{2\pi}{3}(d_{\mu GC} + d_{HDPE})^2 \rho_{\mu GC} d_{\mu GC} \quad \text{(Eq. 1)}$$

Where: $M_{\mu GC}$ – mass of µGC need to cover one HDPE granule, $d_{\mu GC}$ – diameter of one GC grain (10 µm), d_{HDPE} – diameter of one HDPE granule (3 mm), $\rho_{\mu GC}$ – density of GC

The filament extrusion was conducted at ZAMAK DTR EHP-2x16S twin screw extruder (Zamak Mercator Sp. z o.o., Skawina, Poland). The schematic representation of the extrusion process is given in Fig. 14. The extrusion temperature was 180˚C and nozzle diameter was 1.8 mm. The composition of extruded filaments is shown in Table 6. The prepared filaments (Fig. 15) were used to prepare samples via two alternative methods: FDM 3D printing and hot pressing.

Table 6 Compositions of the composites used for the FDM filaments

Sample	**Volume content [%]**			
	HDPE	**µGC**	**sµGC**	**n-Al_2O_3**
HDPE	100.0	-	-	-
µGC	99.0	1.0	-	-
sµGC	99.0	-	1.0	-
n-Al_2O_3	99.0	1.0	-	-
µGC/n-Al_2O_3	99.0	0.5	-	0.5
sµGC/n-Al_2O_3	99.0	-	0.5	0.5

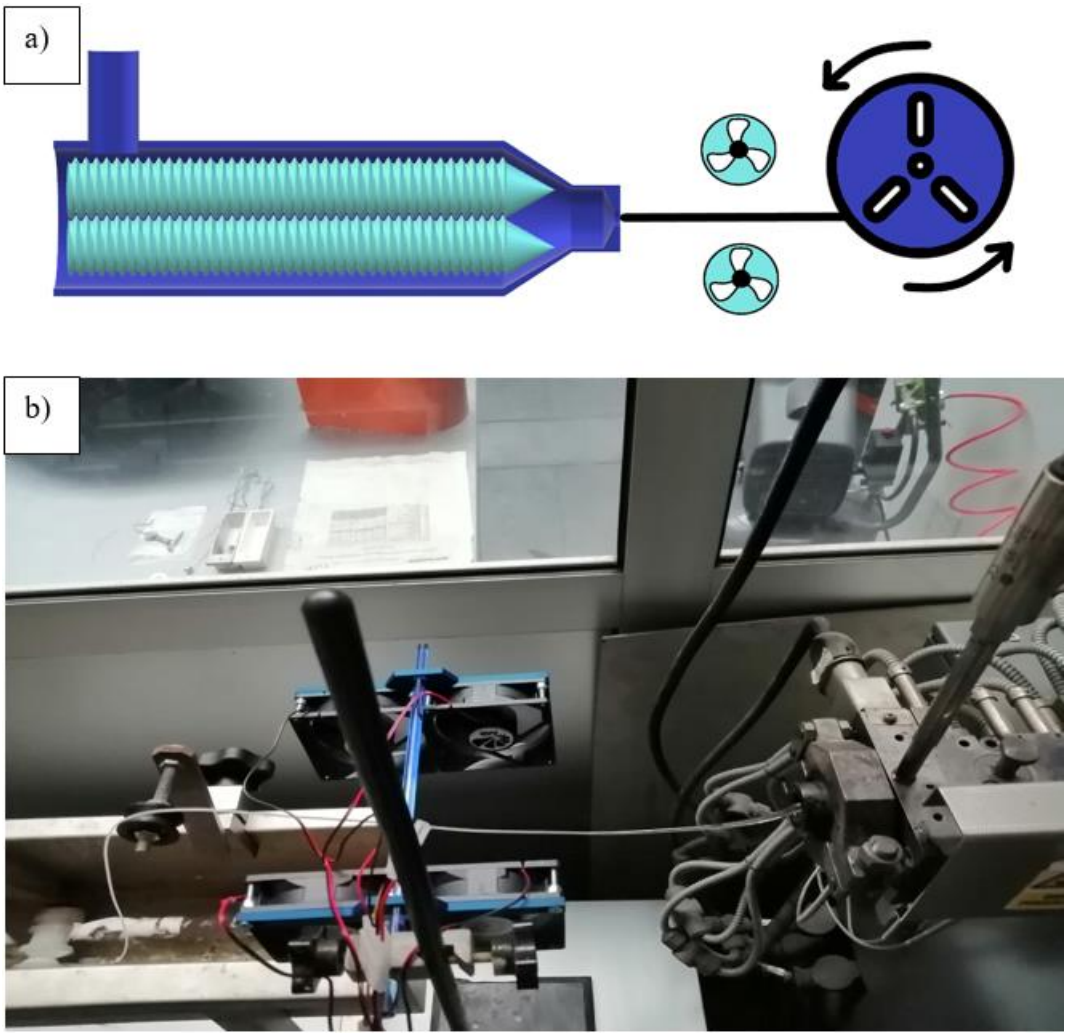

Figure 14 Filament extrusion set up: a) scheme, b) photograph

Figure 15 Examples of extruder filament, from left to right: HDPE, n-Al_2O_3, µGC, sµGC.

The 3D printing process was performed at Original Prusa Mini (Prusa Research a.s., Praga, Czech Republic) with BondTech dual gear extruder upgrade (BondTech AB, Värnamo, Sweden), which are presented in Fig. 16. The parameters of the printing process were optimized to achieve quality necessary to equal to the research tasks. The list presenting challenges during printing process is shown in Table 7. The detailed description on problem solving 3D printing challenges will be presented in *Chapter 3.2.3*. The final printing parameters are presented in Table 8. The g-code for a printer was prepared with use of PrusaSlicer software (version 2.4.0 and newer).

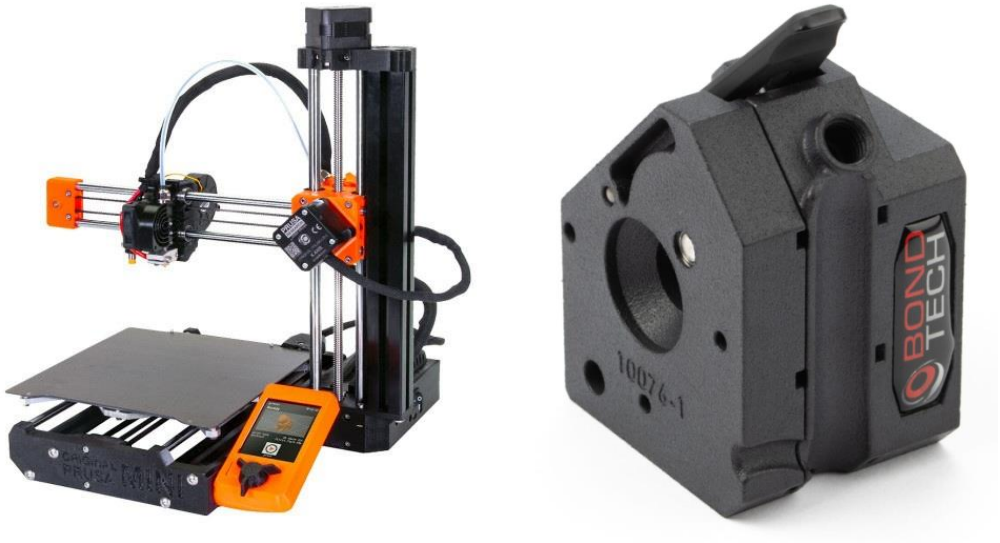

Figure 16 3D printer used in research: Original Prusa Mini (left), BondTech dual gear extruder (right)

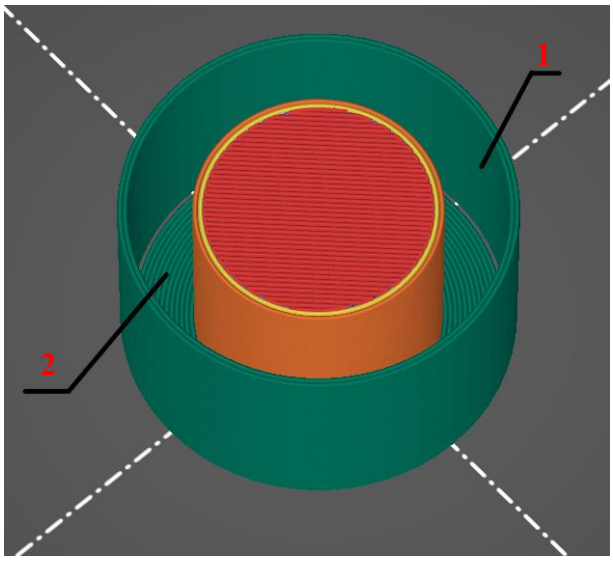

Figure 17 Example of 3D print project visualization: 1 - draft shield, 2 - brim

Table 7 Challenges during printing HDPE and HDPE composites

Problem	Cause	Solution
Under extrusion	Filament slipping at extruder's gear	Upgrade to dual gear extruder
Under extrusion	Low filament diameter (below 1.75 mm)	Increase filament flow rate
Melted infill	Heat concentration in the centre of the print	Increase cooling rate
Cracking during printing	Poor layer adhesion combined with rapid print cooling	Use of draft shielding (Fig.17)
Print detaches during printing	Poor adhesion of PE to common print beds	Use of different bed surfaces
Print warpage	Shrinkage of print	Use of brim (Fig. 17)
Print warpage	Shrinkage of print	Decrease cooling rate
Print warpage	Shrinkage of print	Minimize print surface

Table 8 The FDM 3D printing process parameters

Parameter	Value
Nozzle diameter	0.4 mm
Nozzle temperature	200.0˚C
Bed temperature	85.0˚C
Bed surface	PE tape
Print speed	30.0 mm/s
Feed rate	1.1 – 1.5
Layer height	0.1 mm
Extrusion width	0.45
Cooling rate (Cooling fan speed)	15.0% (40 RPM)
Retraction distance	0.0 mm
Infill ratio	100%
Perimeters count	2.0

The separate set of non-printed samples was produced for tribological tests. The samples were made via hot pressing (HP) in a steel mold. First, the filaments were cut into 5.0 mm pieces and 2.0 g of respective material was added to the mold. The mold was held in 150.0˚C for 2h, until filament was melted. Next, the material was pressed under 30 MPa and hold for 10

seconds under pressure. The sample was left in mold until it cools down to room temperature. The list of all samples subjected to tribological test is presented in Table 9.

Table 9 List of samples' designations

Sample type	3D printed	Hot Pressed
HDPE	HDPE – 3D	HDPE – HP
µGC	µGC – 3D	µGC – HP
sµGC	sµGC – 3D	sµGC – HP
n-Al_2O_3	n-Al_2O_3 – 3D	n-Al_2O_3 – HP
µGC/n-Al_2O_3	µGC/n-Al_2O_3 – 3D	µGC/n-Al_2O_3 – HP
sµGC/n-Al_2O_3	sµGC/n-Al_2O_3 – 3D	sµGC/n-Al_2O_3 – HP

3.2.2. Research methodology

The tensile test of printed samples was performed at Shimadzu AGX-V (Shimadzu Corp. Kyoto, Japan). Test was performed at cross head speed 5 mm/min in ambient condition. The tested samples were HDPE, µGC and sµGC printouts. The tensile strength (R_m) and Young's Modulus (E) were determined. The tested samples are presented at Fig. 18. The results of mechanical test were evaluated using One-way ANOVA variance comparison with post-hoc Fisher's LSD test. The samples' cross-sections were investigated with use of Hitachi S-3400N microscope at 15.0 kV acceleration voltage and in low vacuum conditions.

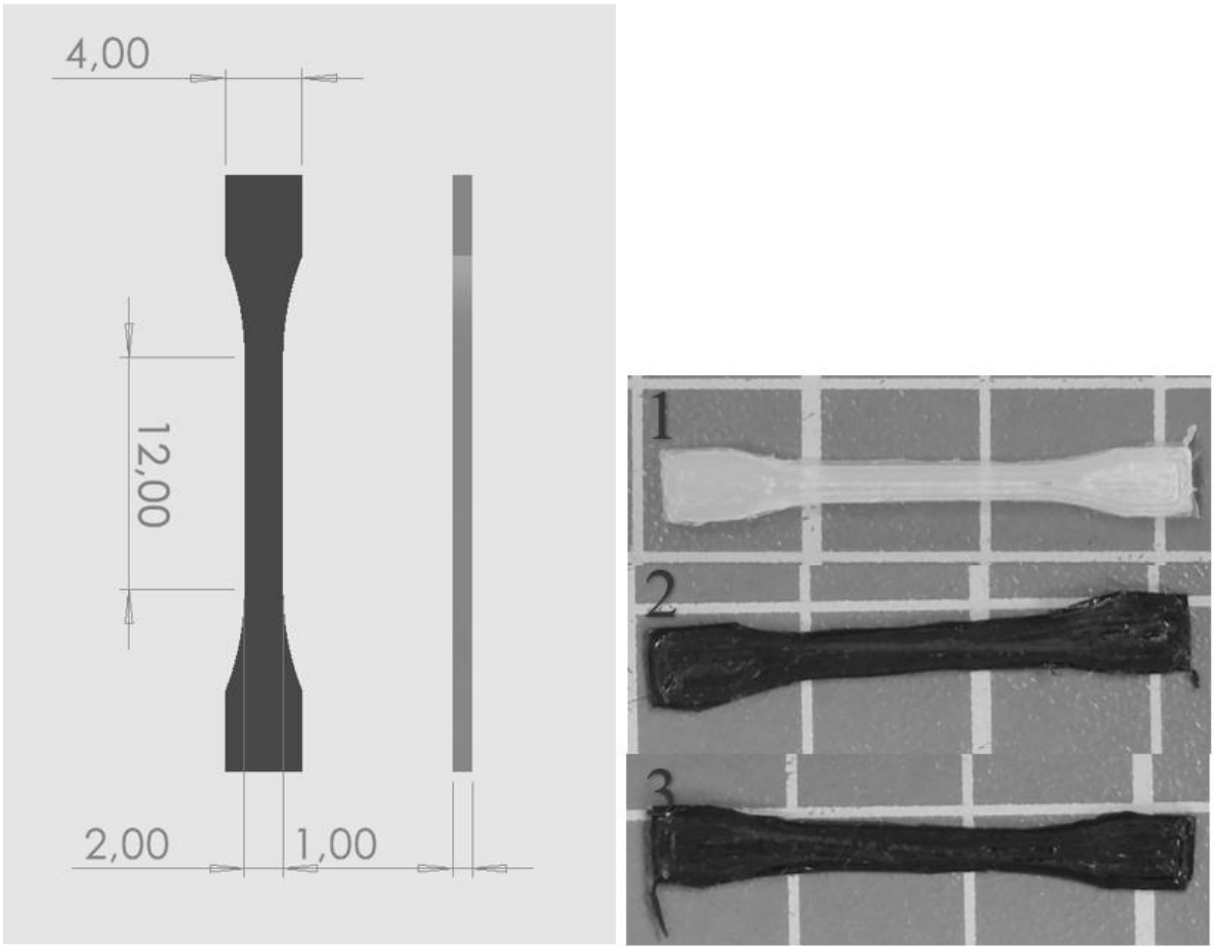

Figure 18 Scheme of sample for mechanical testing (left) and macrographs of 3D printed samples: HDPE (1), µGC composite (2) and sµGC composite (3)

Melt mass-flow rate (MFR) of the neat HDPE and the composite filaments was determined using CEAST plastometer (by CEAST/Instron, USA) with accordance to ISO 1133-1 standard. Cut filament, previously obtained in the extrusion process, was used as a sample batch. The measurement was made at 190.0˚C and under load of 2.16 kg. The mass measurement for the materials was performed at five samples each, with the 20.0 second cut time. Collected data was used for calculating shear-rate (Eq.2) and viscosity (Eq.3) [90]

$$\dot{\gamma} = \frac{4MFR}{600\rho\pi R_n^3} \quad \text{(Eq.2)}$$

where: γ – shear rate [1/s], ρ – melt density (754.6 kg/cm^3 for neat HDPE and 766.8 kg/cm^3 for composite filaments), R_n – nozzle radius (0.9 mm);

$$\eta = \frac{R_n L g}{2\pi R_p^2 l \dot{\gamma}} \quad \text{(Eq.3)}$$

where: η – dynamic viscosity [Pa*s], L – load (2.16 kg), g – gravitational acceleration [m/s], R_p – piston radius (4.8 mm), l – nozzle length (7.7 mm).

The structural analysis by X-ray diffraction was performed on the Panalytical Empyrean diffractometer with Cu Kα anode and Kβ filter made from Ni. The test samples were HDPE, μGC composite and sμGC composite printouts. The scanning range was set between 10.0˚2θ and 50.0˚2θ. The characteristic peaks for PE crystal structure were fitted to measured spectrum using Guassian-Lorentzian equation [64]. The fitting parameters were calculated by using Origin Software. The obtained fitted peaks profiles were used to calculate the crystallites size (Eq.4) and the polymer crystallinity (Eq.5):

$$L = \frac{K\lambda}{\beta cos\theta} \quad \text{(Eq. 4)}$$

where: L – crystallite size [Å], K – shape factor (0.89), λ – wavelength of XRD anode (1.5406 Å), β – peak FWHM [rad], θ –peak centre [rad];

$$\chi = \frac{A_c}{A_A + A_c} * 100\% \quad \text{(Eq. 5)}$$

where: χ – crystallinity [%], A_c – area of crystalline peaks, A_A – area of amorphous broadening.

To determine impact of GC at melting and crystallization process, the differential scanning calorimetry (DSC) was performed. The research was performed for neat HDPE, μGC composite and sμGC composite filaments. The DSC was performed with use of 2920 DSC V2.6A (TA Instruments, New Castle, USA). The measuring range was between 0.0˚C and 200.0˚C with 10K/min heating and cooling rate under a nitrogen atmosphere with a nitrogen flow rate of 50 ml/min. Samples of approximately 10 mg were encapsulated in standard non-hermetic aluminium pans. The two cycles of heating and cooling were applied for single test. First cycle was used to remove a thermal history of the material and determine the crystallization temperature (T_c) and the crystallization enthalpy (ΔH_c). Second cycle was used to determine the melting temperature (T_m) and the melting enthalpy (heat of fusion, ΔH_m) in accordance with ISO 11357-3 standard. The obtained data and the heat of fusion of 100% crystalline HDPE (ΔH_m^0= 293.0 J/g) was used to calculate crystallinity according to Eq. 6:

$$X_c(\%) = \frac{\Delta H_m}{\Delta H_m^0 - (1-\varphi)} \cdot 100 \quad \text{(Eq. 6)}$$

where: χ_c – crystallinity from DSC [%], ΔH_m – heat of fusion [J/g], ΔH_m^0 – heat of fusion of 100% crystalline HDPE [J/g], φ – mass percentage of reinforcement.

The tribological tests, performed in order to obtain the friction coefficient (COF) and mass wear of the materials, were conducted at ambient condition under technically dry friction conditions using a pin-on-block tribo-tester set up (Fig. 19) constructed and available at Faculty of Materials Engineering, Silesian University of Technology (Katowice). The samples were cylindrical shaped with 20.0 mm in diameter and: 2.0 mm in height for 3D printed samples and 7.0 mm in height for hot pressed samples. For each test, the sample was positioned in the direction providing the printed paths at 45˚ to the sliding movement. This angle was chosen as the best performing in accordance with other studies [91]. In the test, the normal force of 10.0 N was used and the sliding speed was 0.1 m/s. The test was conducted over sliding distance of 1000.0 meters. The two different counterparts were used alternatively: alumina ball and stainless-steel ball, both 5.0 mm in diameter. During tribological tests, the friction load was measured continuously by using a strain gauge connected with an analogue-digital converter and recorder. The obtained data was used to calculate the friction coefficient. The samples were weight before and after the test. The mass wear rate was calculated with following equation:

$$W = \frac{m_0 - m_1}{m_0} * 100 \quad \text{(Eq. 7)}$$

where: W – mass wear rate [%], m_0 – sample mass before test [g], m_1 – sample mass after test [g].

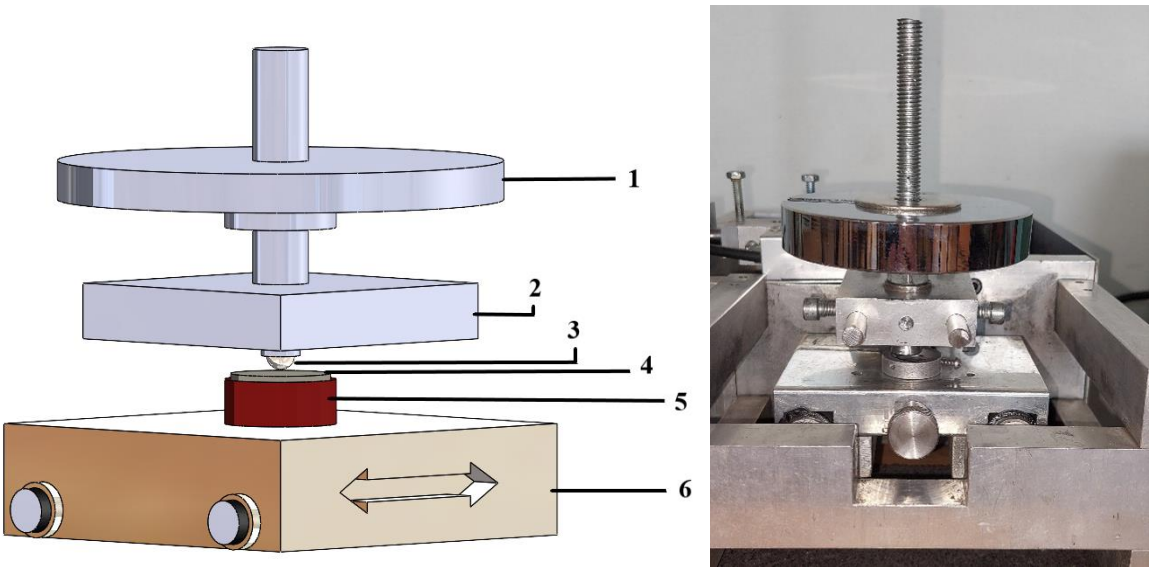

Figure 19 Scheme of tribo-tester set up: 1—Load, 2—strain gauge holder, 3—counterpart (ball), 4—sample, 5—sample holder, 6—moveable plate; on the right side – photo of the real stand

3.2.3. Results

The morphology of selected prepared composite granules is presented in Fig. 20 and Fig. 21. The micrographs exhibit that each time most of the granule surface is covered with powder, however some areas without powder and with excess of powder are visible. This might be a result of poor adhesion of GC and n-Al_2O_3 to HDPE. Also, the alumina particles tend to agglomerate forming a particle with 4.0 μm and below in diameter, which are distributed between the GC particles.

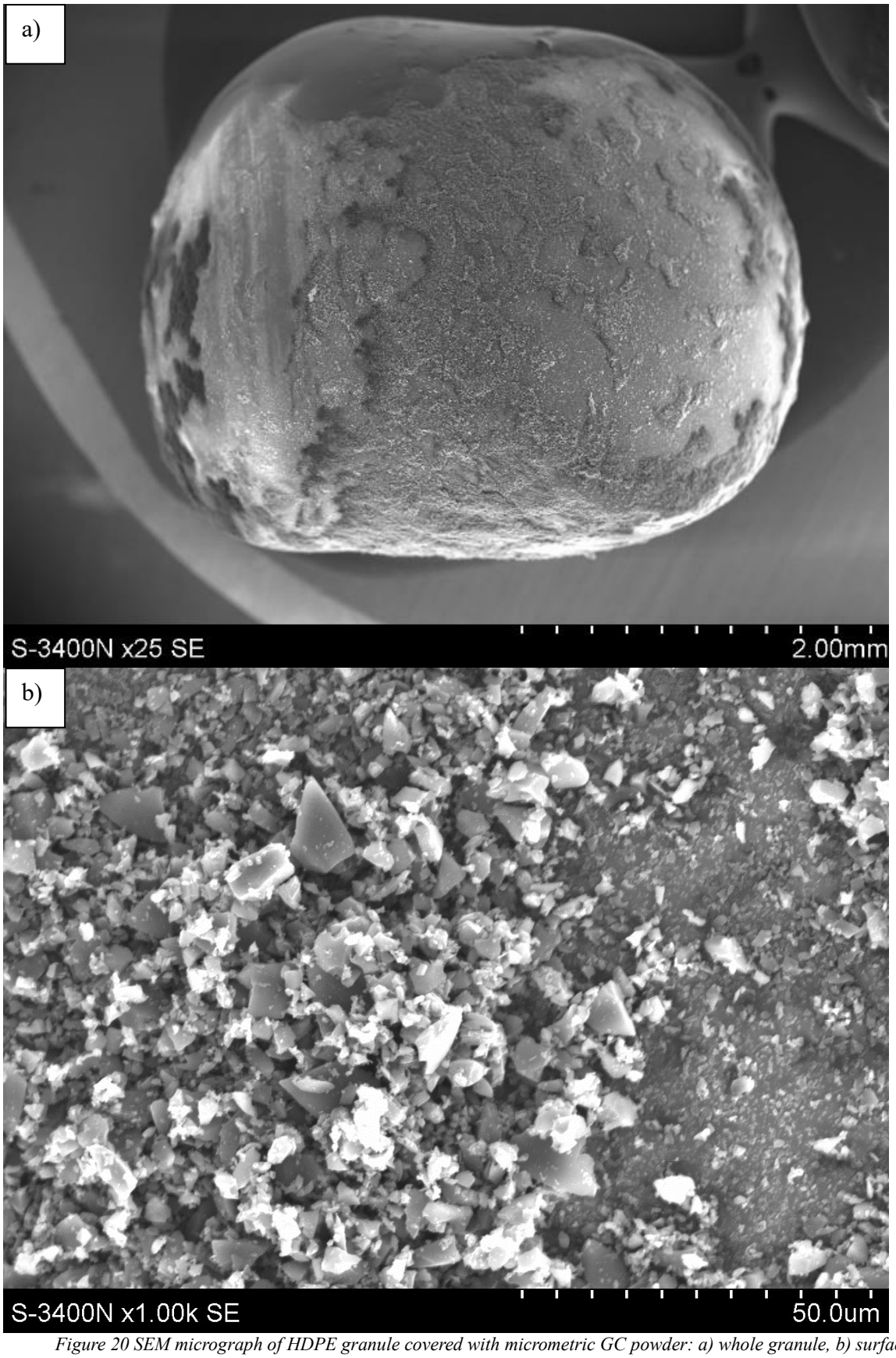

Figure 20 SEM micrograph of HDPE granule covered with micrometric GC powder: a) whole granule, b) surface fragment

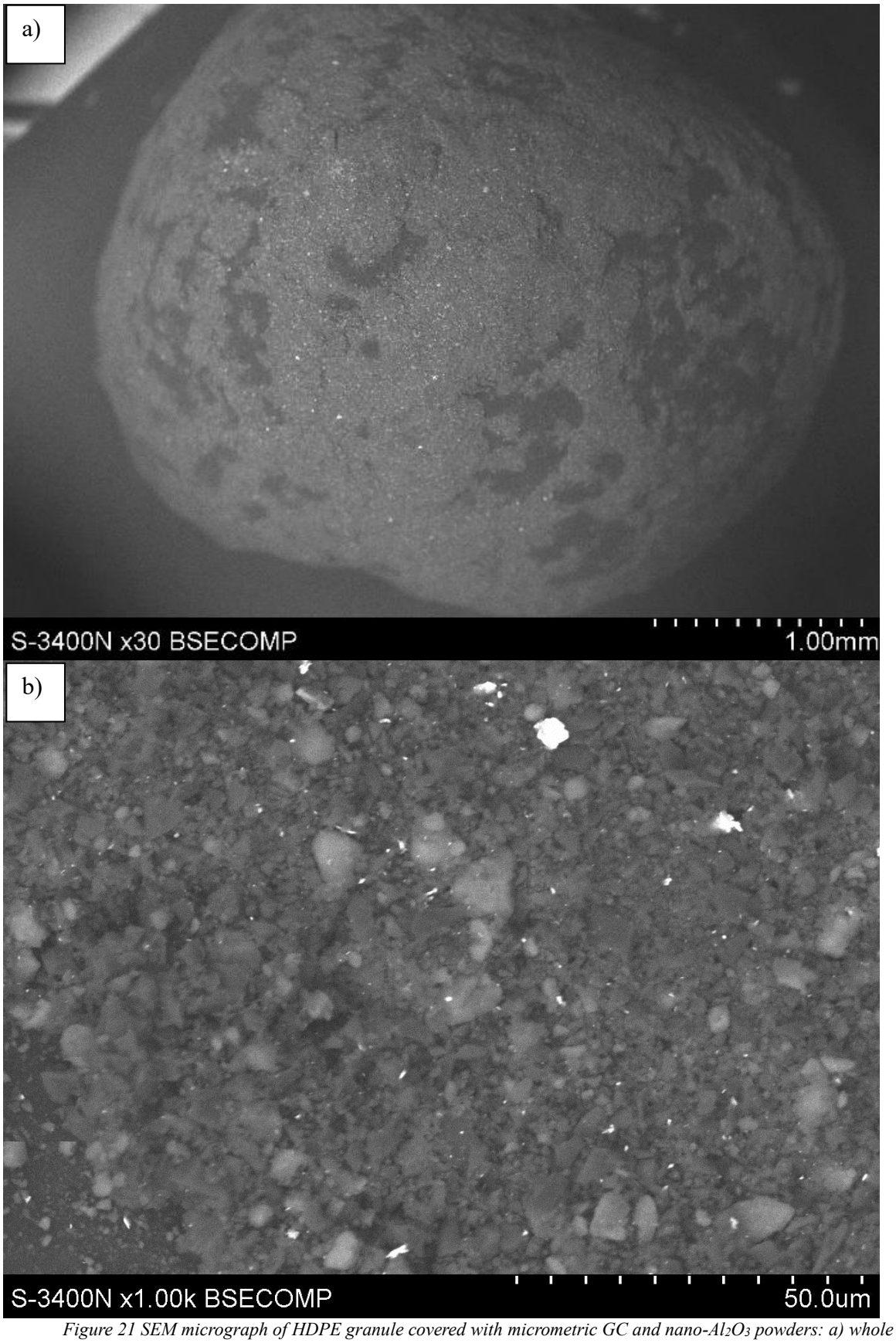

Figure 21 SEM micrograph of HDPE granule covered with micrometric GC and nano-Al_2O_3 powders: a) whole granule, b) surface fragment

The examples of 3D printed parts are presented in Fig. 22. The challenges of HDPE 3D printing come from two things: high crystallinity and chemical structure. The first one causes sudden shrinkage during fast cooling. The molten HDPE has density of 0.820 g/cm^3 [64], while the crystallites have 0.985 g/cm^3. The final density, assuming 80% of crystallinity, is 0.955 g/cm^3. In theory, this result in around 14.0% of volume shrinkage, which is unavoidable without any crystallization inhibitors. In result, that phenomenon causes lifting of print edges (warping or warpage), cracks (delamination) between layers and detaching from print surface. Additionally, due to latent heat of crystallization and poor thermal conductivity of PE, the excess of heat makes a printout central area one molten piece during printing, which results in poor reproduction of details. To minimize the impact of the above mentioned effects, the use of a brim, a draft shield, and minimal cooling was required. The brim compensates some of warping and draft shield, by "closing" warm air around print, reduces cracking. Use of cooling during print helps to accelerate removing of heat from printout central area.

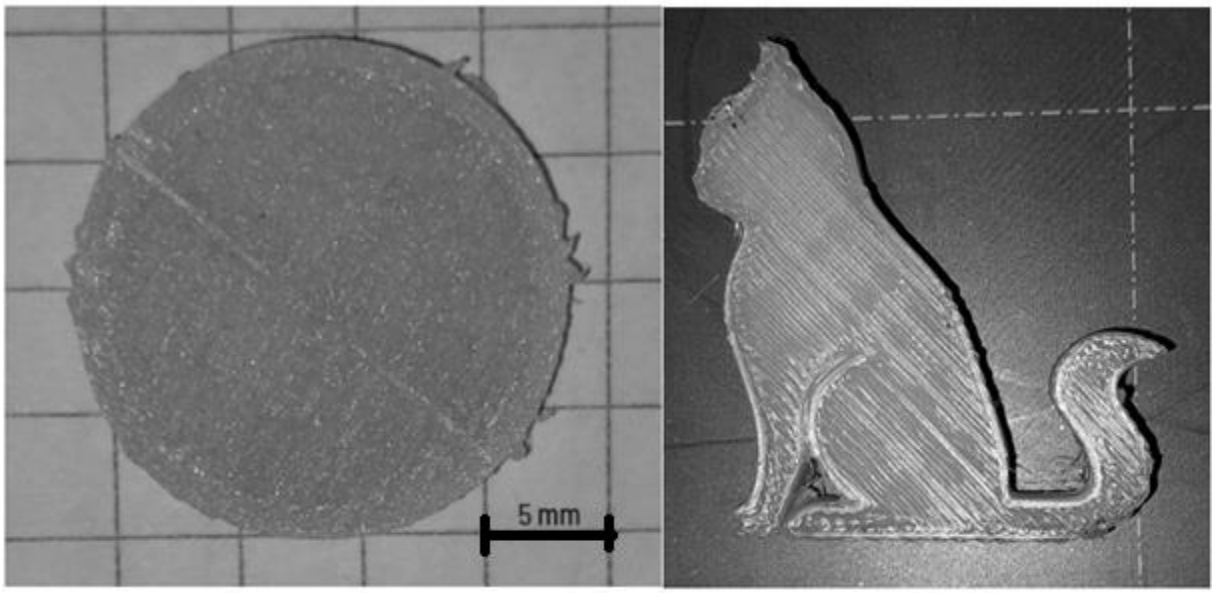

Figure 22 Macrograph of exemplary FDM 3D printed HDPE parts

The adhesion to a print bed was another challenge. The HDPE is known as strongly polar and chemically resistant polymer and many substances do not stick to it surface easily. This – for instance - makes gluing of HDPE parts difficult. Similar effect is observed during 3D printing. One of the most important things during FDM process is adhesion between the overlaid thermoplastic path and the print bed surface. The HDPE does not adhere to most of the bed materials used in printers (such as: glass, SiC, PEI, PVA glue layer). In the field most popular bed surface for HDPE 3D printing is PE or PP packing tape. However, the usage of Styrene-ethylene-butylene-styrene copolymer (SEBS) was presented in literature [76]. By

comparing the chemical structure of PE and SEBS (Fig. 23), the argument that print bed surface should have similar chemical groups to HDPE can be made.

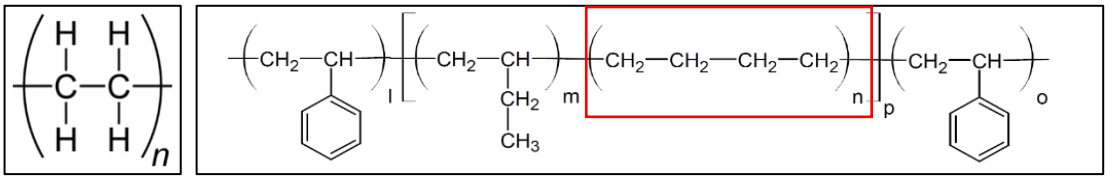

Figure 23 Chemical structure of PE (left) and SEBS (right)

The other commonly used polymer containing ethylene group is polyethylene terephthalate (PET, Fig. 24), which is also one of the most popular materials for 3D printing. To evaluate viability of PET as a print bed surface, the 3D printed thin rafts was used and compared with regular PE packing tape. Different printing temperatures were tested. The result of test show that PET can be used as a print bed surface (Fig. 25) in printing temperature range between 200˚C and 240˚C. However, the technological difficulty is changing filament after raft printing. The leftovers of PET were visible (colour change) in few first layers and cleaning the nozzle after switching filaments discourage of using this material as printing surface.

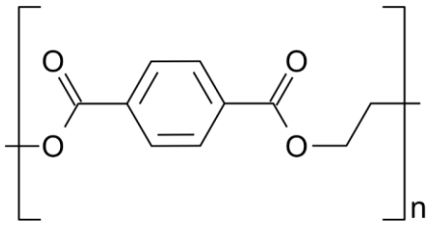

Figure 24 Chemical structure of PET

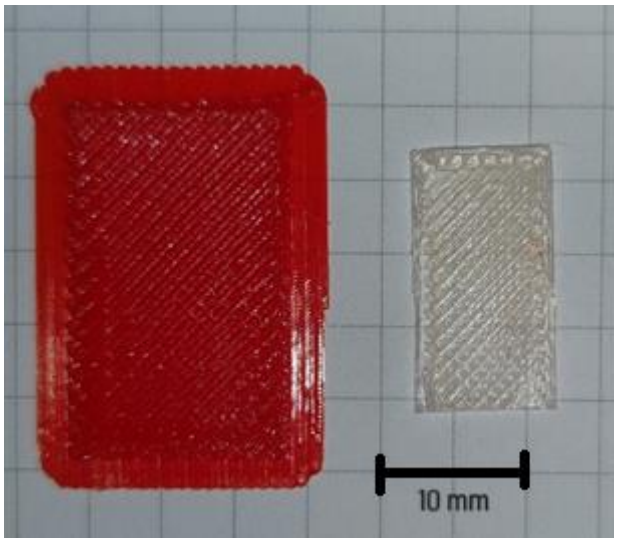

Figure 25 3D printed PET raft (left) and HDPE sample (right)

The PE packing tape performed well, however above 200˚C it melts and aderes to the first layer of the print and became damaged during print detaching (Fig. 26). Thus, the printing temperature of 200˚C was chosen in further printing.

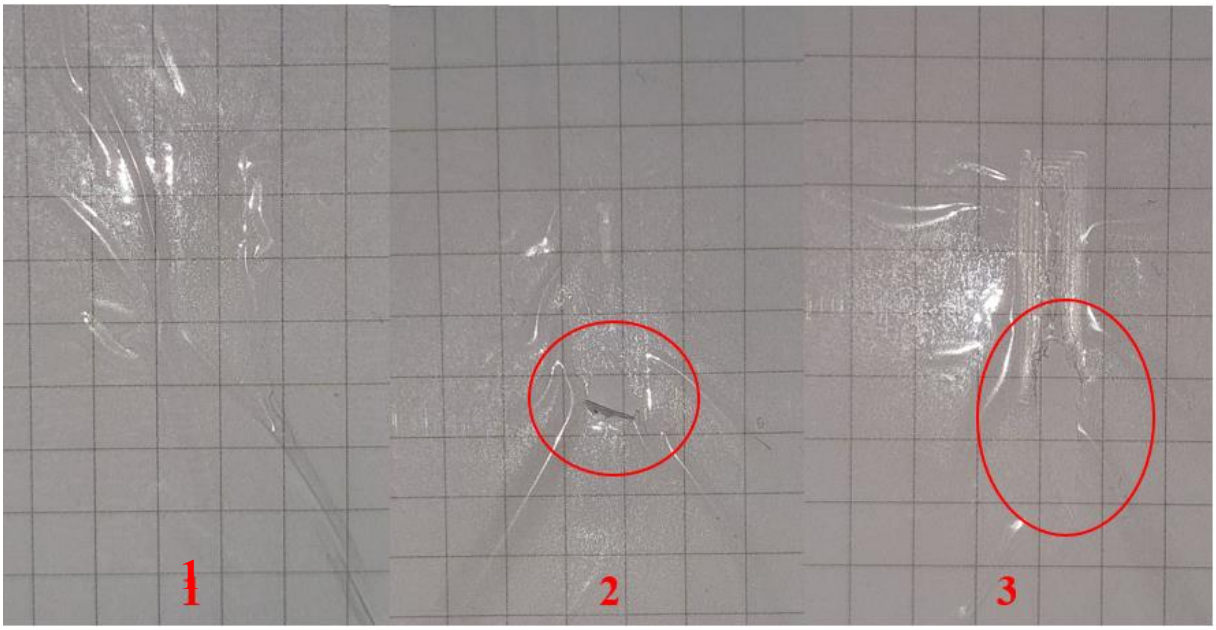

Figure 26 PE packing tape after printing: 1 – 200˚C, 2 – 220˚C, 3 – 240˚C, red circle – damaged area

The results of mechanical tests are presented in Fig. 27 and Table 10. They show that printed samples have lower tensile strength than value reported by HDPE producer (for the equivalent injected samples). Also, the composites with GC reinforcement have higher R_m and E than neat HDPE. However, the composite with µGC exhibit the highest values. The cross-sections of the composite samples after tensile tests are visible in the Fig. 28 and Fig. 29.

The mechanism of reinforcement behavior during tension is visible in the form of powder particles being pulled out from the polymer matrix, resulting in holes or voids within the matrix. This phenomenon is observed in both composites. In the sμGC composite, the voids are smaller and more evenly distributed throughout the cross-section. In the case of the μGC composite, some particles with fractured surfaces can be observed, indicating that larger diameter GC particles can partially bear the load during tension. However, the presence of voids suggests poor adhesion between the GC particles and the matrix. The sμGC particles may have a weaker bond to the HDPE matrix compared to the μGC ones and due to lower diameter, they are more easily pulled out. This explanation goes hand in hand with the results of the tests - μGC is stronger than sμGC. However, another explanation for the breakage of some particles in μGC may be the negative impact of the scale effect. In the case of larger particles, there is simply a greater probability of defects occurring in the material, which are the beginning of the failure process. In smaller particles this probability is lower, therefore in the (relatively small) analysed population we do not observe particle cracks in the sμGC composite. However, the overall increase in strength of the composites compared to neat HDPE may be attributed to the synergistic effect of load bearing during tension, energy dissipation due to debonding particle from matrix and changes in the crystal structure of the matrix.

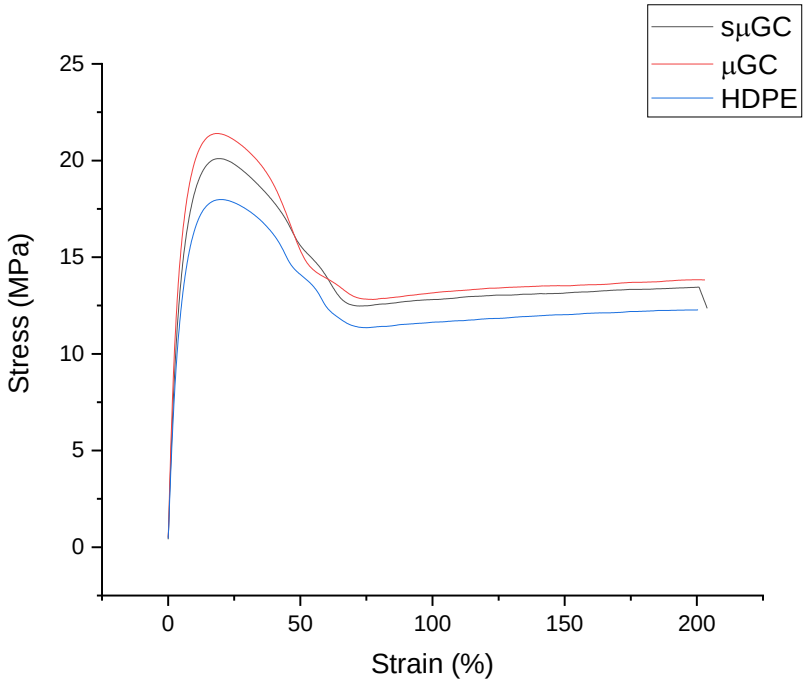

Figure 27 Representative curves of static tensile test

Table 10 Results of static tensile test

Sample	Tensile strength (R_m) [MPa]	Young's modulus (E) [MPa]
HDPE	17.99 ± 0.23	335.61 ± 14.03
μGC	21.41 ± 0.32	483.06 ± 23.69
sμGC	20.10 ± 0.33	395.78 ± 40.66

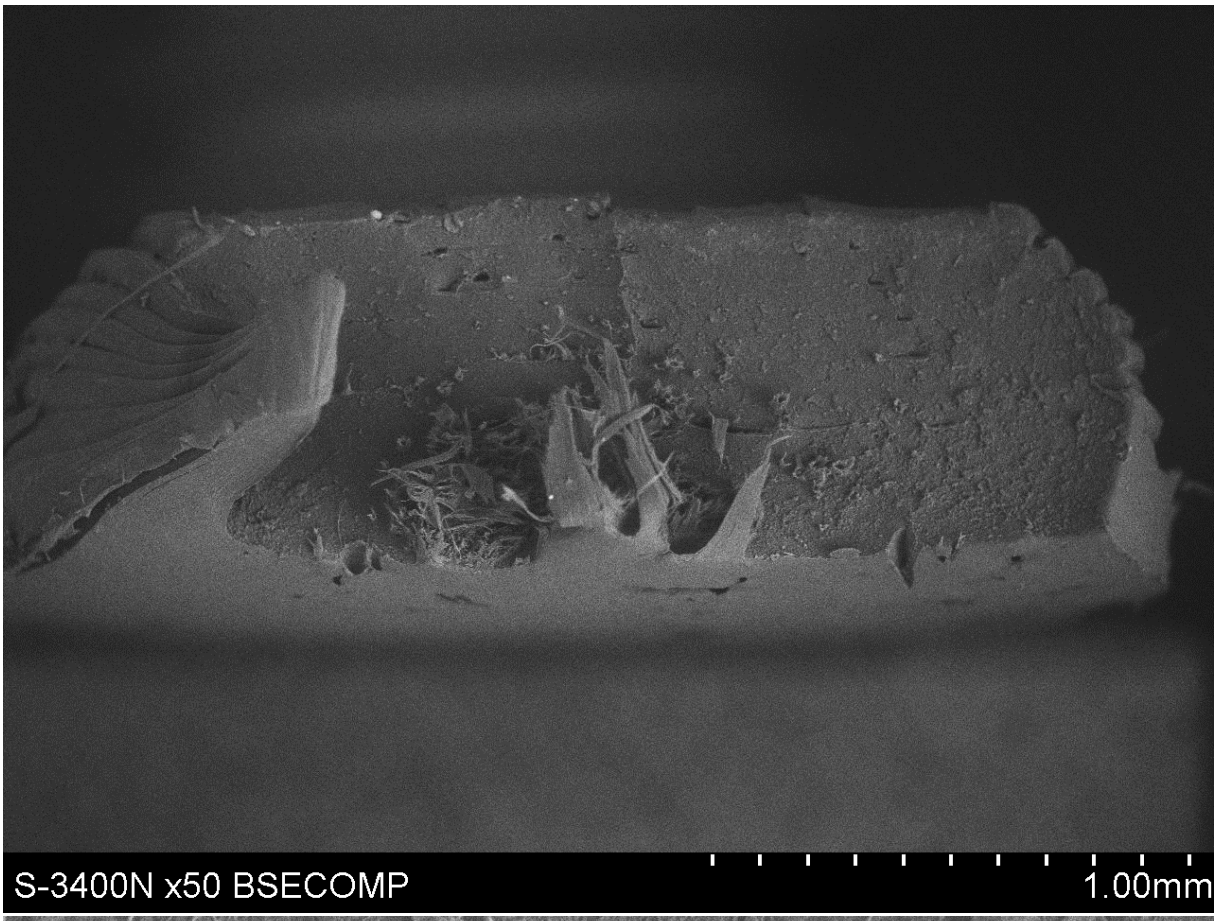

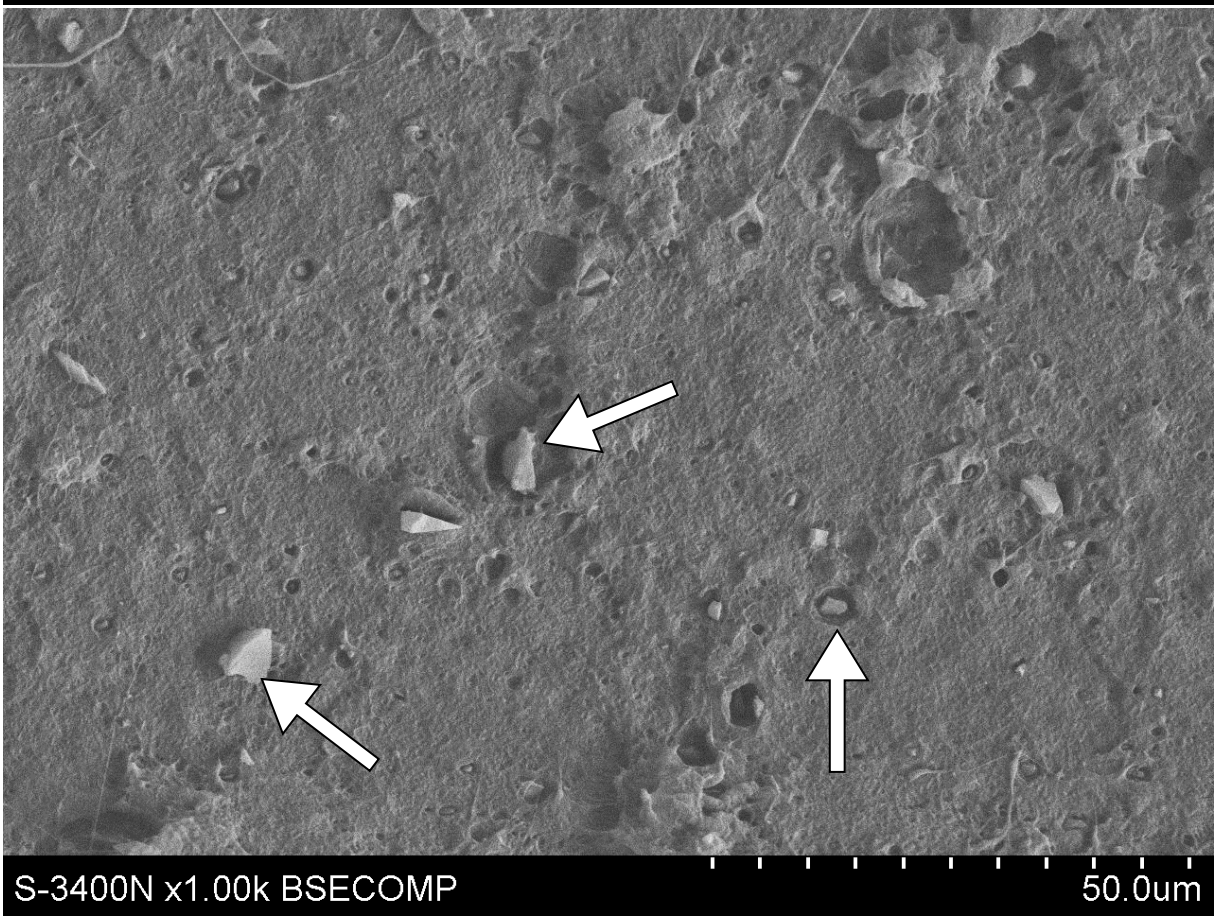

Figure 28 SEM micrographs of the cross-section of μGC sample at different magnifications

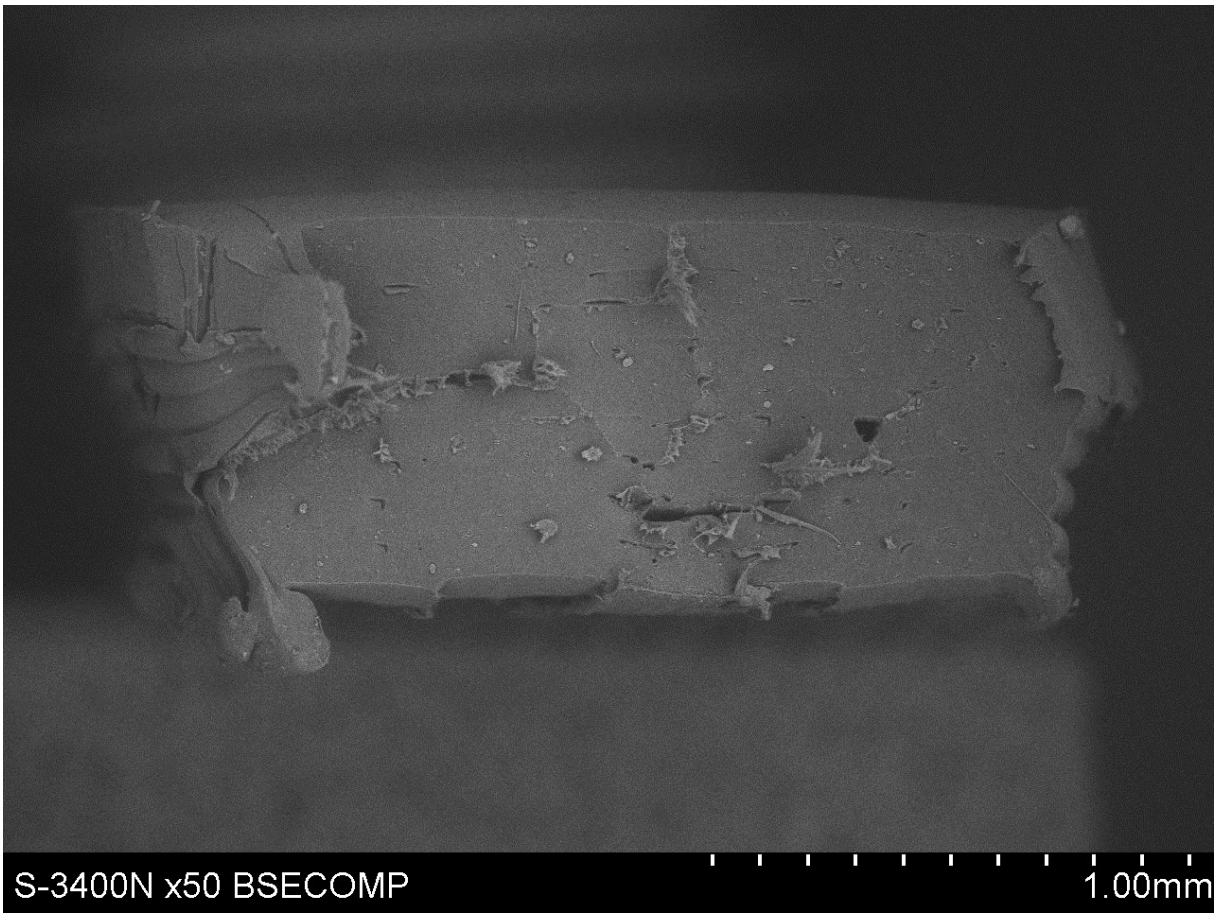

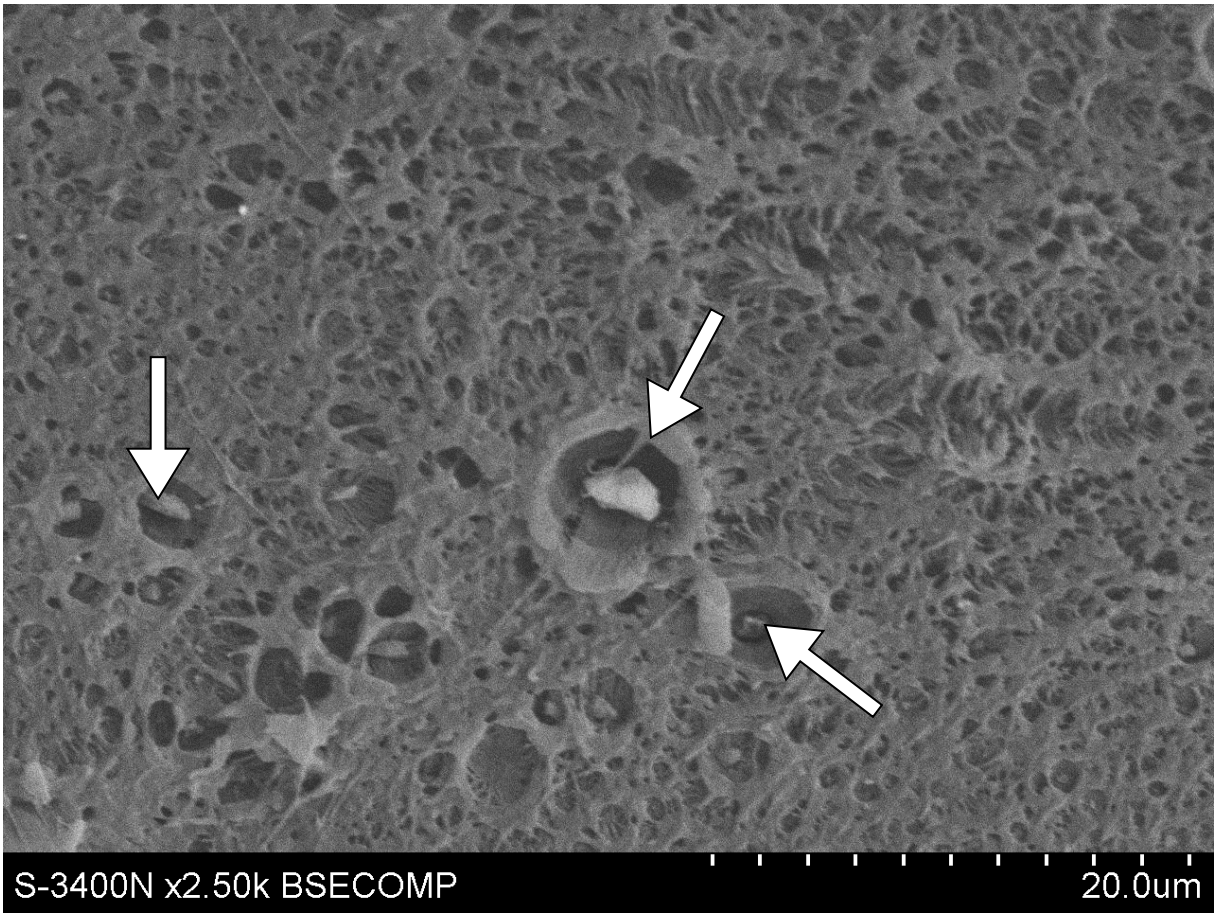

Figure 29 SEM micrographs of the cross-section of sμGC sample at different magnifications

The results of MFI and viscosity calculations are presented at Fig. 30 and Fig. 31. The addition of GC decreased the melt flow index value. However, statistical analysis shows that only sμGC is significantly different from neat HDPE. In case of dynamic viscosity calculation, the composite filament shows significantly higher viscosity value than neat HDPE, which was confirmed by statistical analysis. The above observation can be explained by limiting polymer chain movement possibilities by GC particles. The bigger impact in this regard has sμGC due to smaller size of particles, closer to molecular level of structure, in comparison with the μGC.

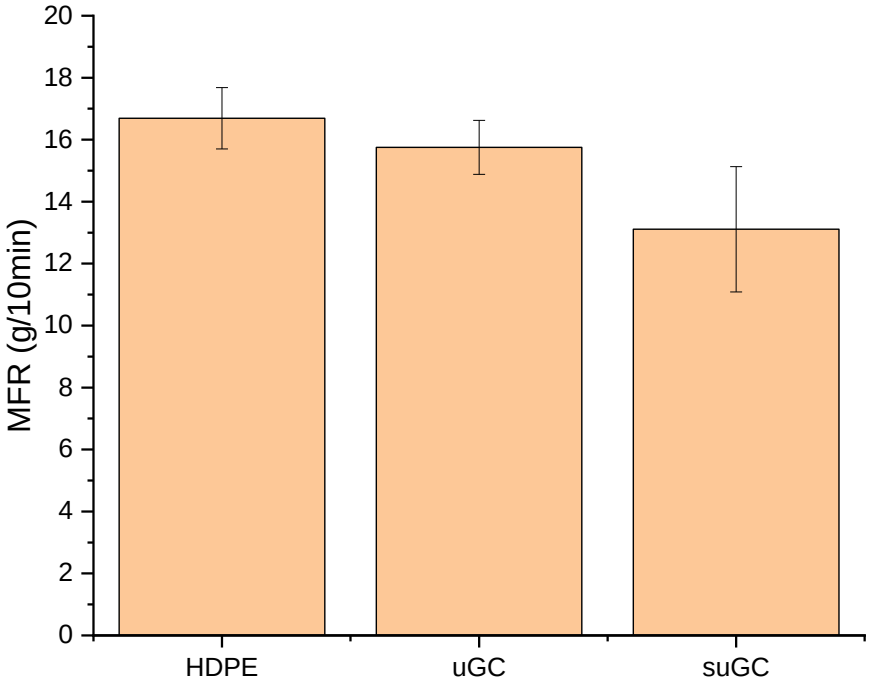

Figure 30 The MFI results for neat HDPE and composite filaments

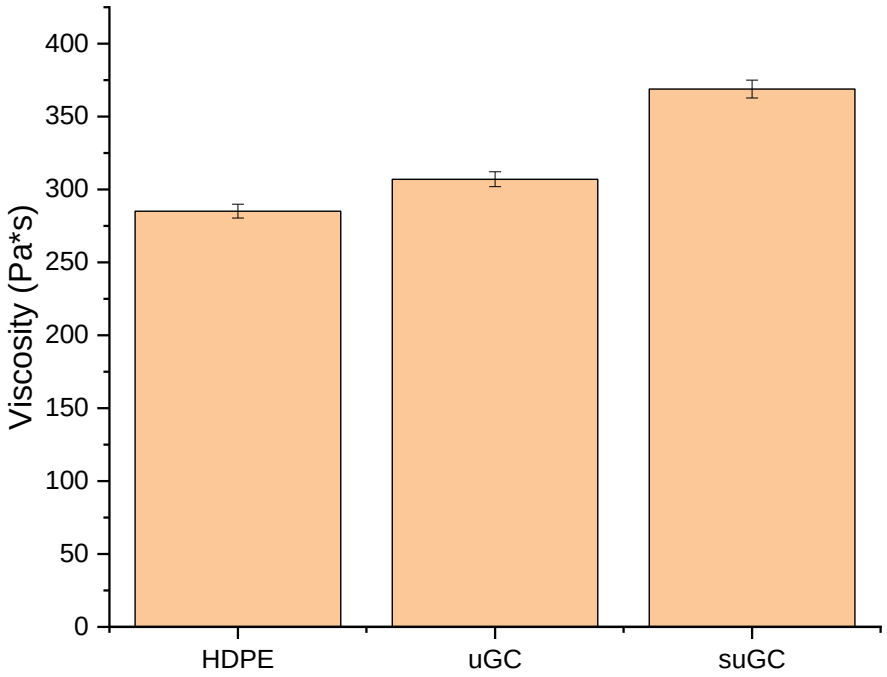

Figure 31 Dynamic viscosity results for neat HDPE and composite filaments

The results of XRD analysis are presented in Fig. 32 and Table 11. The main PE crystalline peaks which are visible, correspond to planes (110) and (200). The peaks positions for the composite samples show a shift towards lower 2θ values, which can be concluded as a decrease of crystallite sizes. This is supported by apparent crystallite size calculation. The lowest values of crystallite size for L_{110} and L_{200} was reported for sμGC. The reinforcement particles acting as surface for heterogenous nucleation of PE-orthorhombic phase. The lower value of crystallite size is also the result of the suppressed crystal growth caused by the presence of GC particles. The sμGC composite exhibites the lowest value of crystallite size due to higher dispersion level than in μGC composite. The calculated crystallinity is presented in Fig. 33. It shows that crystallinity is slightly higher for the composite samples, and the highest value was reported for μGC composite.

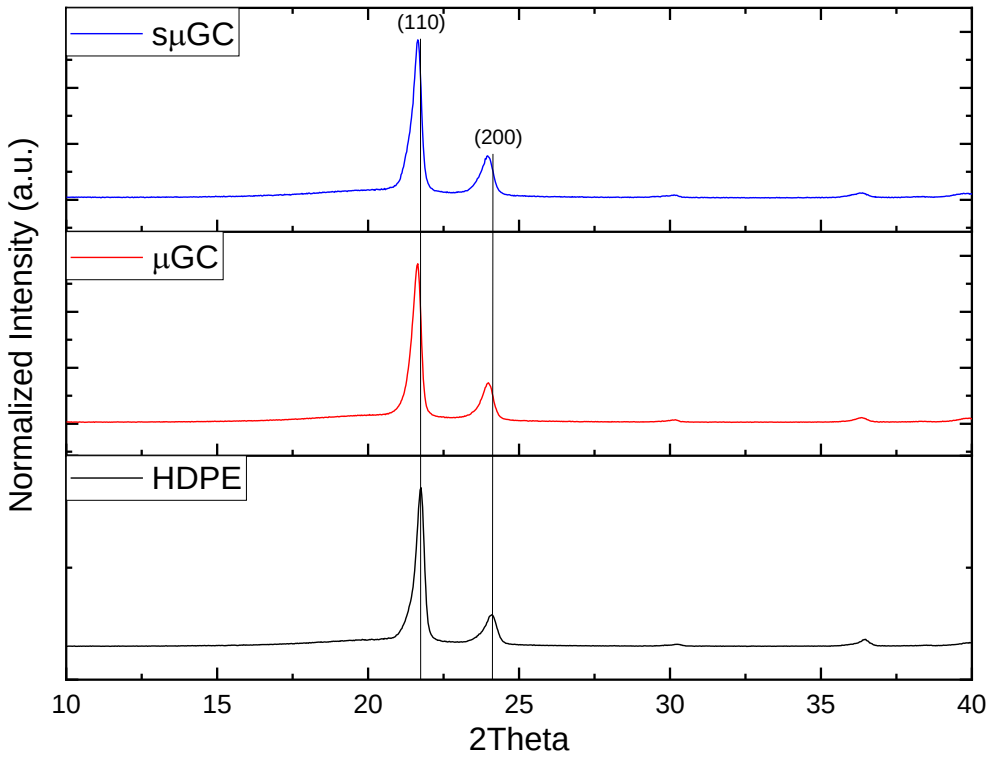

Figure 32 XRD spectrum of FDM 3D printed samples – neat HDPE and its composites with μGC and sμGC particles

Table 11 Results of apparent crystallite size calculation for neat HDPE and its composites with μGC and sμGC particles

Sample	Peak position [°2θ]	B [°2θ]	L [Å]	(hkl)
HDPE – 3D	21.7170	0.3201	241.02	110
	24.0537	0.4768	161.14	200
μGC – 3D	21.6047	0.3332	231.58	110
	23.9487	0.4537	169.37	200
sμGC – 3D	21.6170	0.3456	223.31	110
	23.9302	0.4841	158.75	200

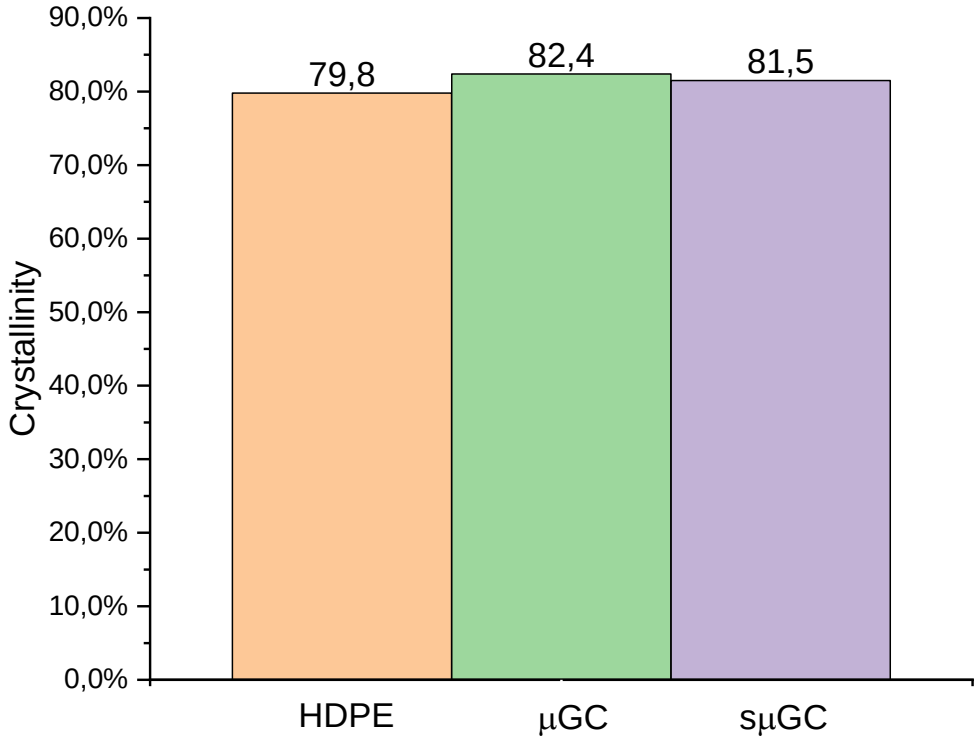

Figure 33 Crystallinity results from XRD for neat HDPE and its composites with µGC and sµGC particles

The results of thermal analysis are presented in Fig. 34 and Table 12. The slight decrease in melting point (both first and second melting cycle) for composite filaments was observed. However, the first melting cycle was used to remove the thermal history of the materials, thus is not needed to interpret this part. Although, the slight decrease in T_{m2} for sµGC composite might be related to chain compaction and crystal imperfections caused by limitation of polymer chains mobility by the particles. This effect is not observed in µGC composite, which suggest that larger particles do not impede the crystal structure formation as much as the smaller particles. This is confirmed by XRD apparent crystallite size calculation and observed changes in viscosity. The significant increase in crystallization onset temperature suggests that both µGC and sµGC particles act as heterophase nucleates for HDPE crystallites. The highest increase was observed for sµGC, which is related to most probably higher specific surface area. The crystallinity calculation shows that sµGC composite is characterized by lower value of crystallinity than neat HDPE and µGC composite. This confirms the above mentioned interpretation. The smaller particles act as nucleates for HDPE, however due to easier dispersion than larger particles may impede crystal growth and negatively impact crystallinity. It is worth to notice that crystallinity calculated from DSC results does not match crystallinity calculated

from XRD. This difference between the methods' results has already been reported in literature [64].

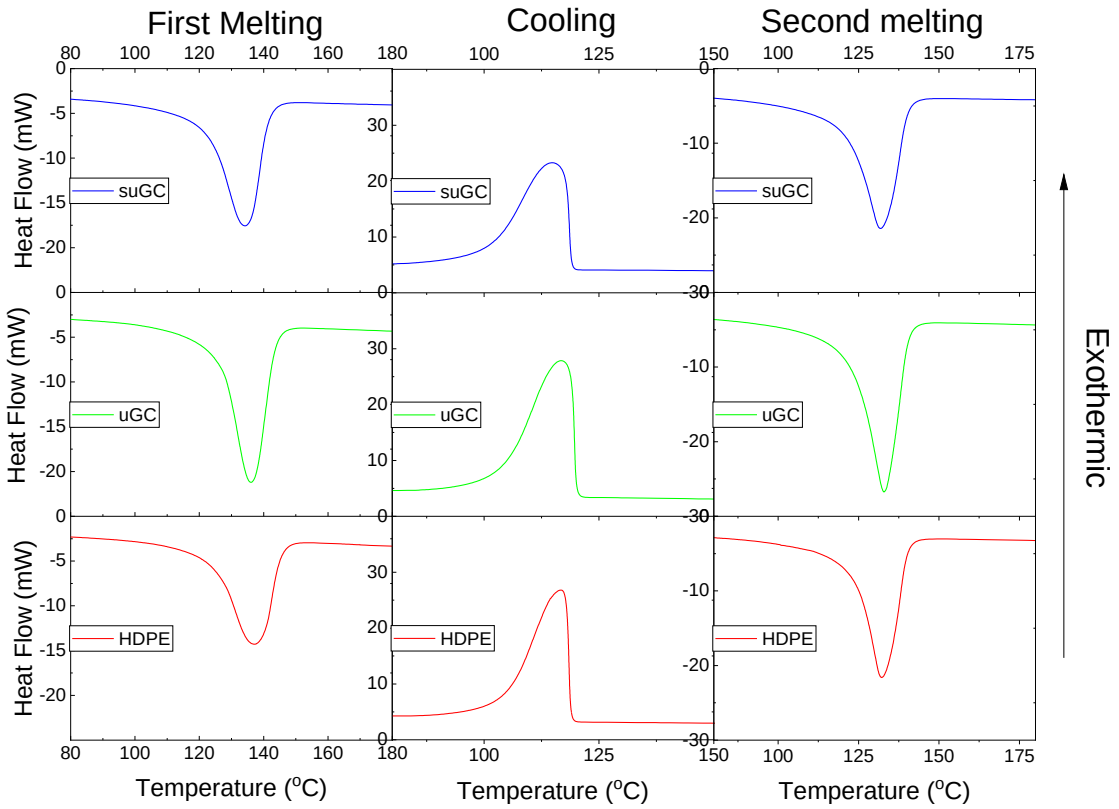

Figure 34 DSC results: left column - 1st melting cycle, middle column - crystallization, right column - 2nd melting cycle.

Table 12 Results of DSC analysis: T_{m1} – melting point during first melting cycle, $T_{c,\,on}$ – crystallization onset, T_c – crystallization temperature, $T_{m,\,on}$ – melting onset during second melting cycle, T_{m2} – melting point during second melting cycle, ΔH_m – enthalpy of melting. χ_m – crystallinity from melting

Sample	T_{m1} [°C]	$T_{c,\,on}$ [°C]	T_c [°C]	$T_{m,on}$ [°C]	T_{m2}	ΔH_m [J/g]	χ_m
HDPE	136.89	118.83	116.78	123.08	132.18	186.00	63.5%
µGC	135.93	120.03	116.96	122.37	132.89	188.80	65.9%
sµGC	134.23	121.65	114.81	120.60	131.86	174.70	61.0%

The relation between friction coefficient (CoF) and sliding distance are presented in Fig. 35-38. The friction coefficient for composites was reported slightly higher than those for neat HDPE sample. The highest CoF was reported for samples with n-Al_2O_3, which correlate with wear rate results (Table 13 and Table 14). However, in all combination (counterpart material, manufacturing process) addition of GC reinforcement stabilize CoF curves over whole sliding distance. The ware rate for 3D printed parts is most often higher than those for the hot-pressed samples.

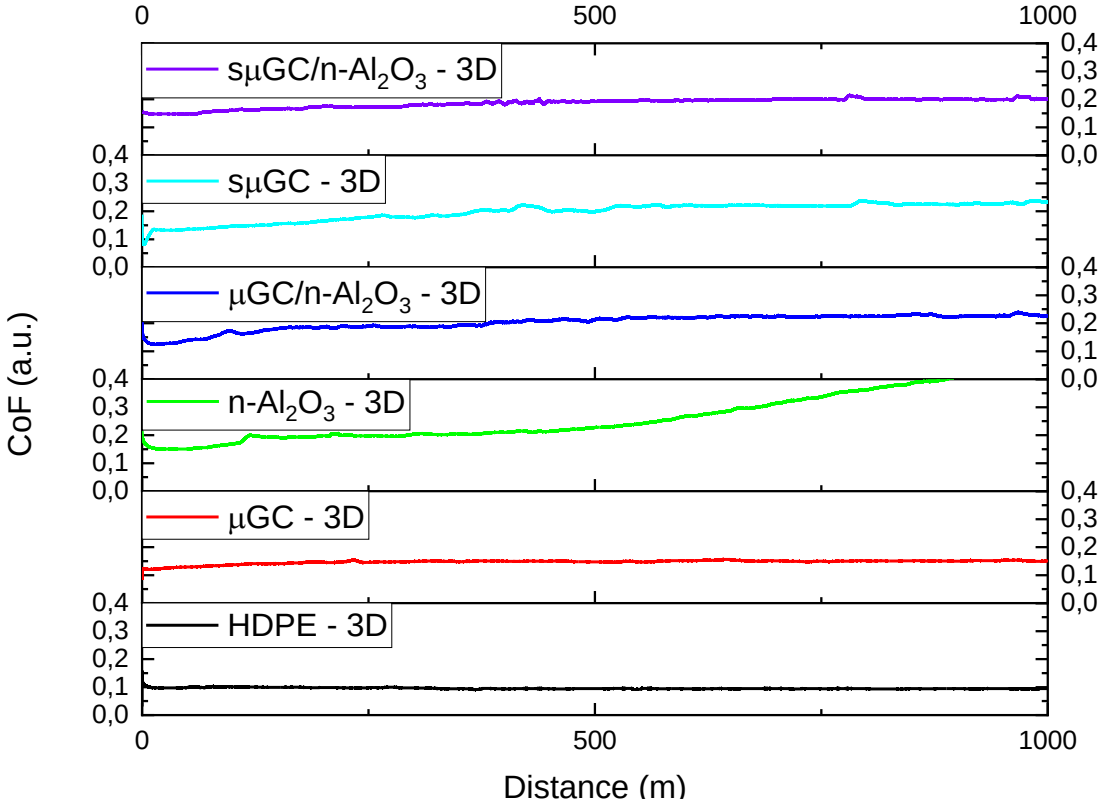

Figure 35 Coefficient of friction vs. distance for 3D printed samples with alumina ball countersample

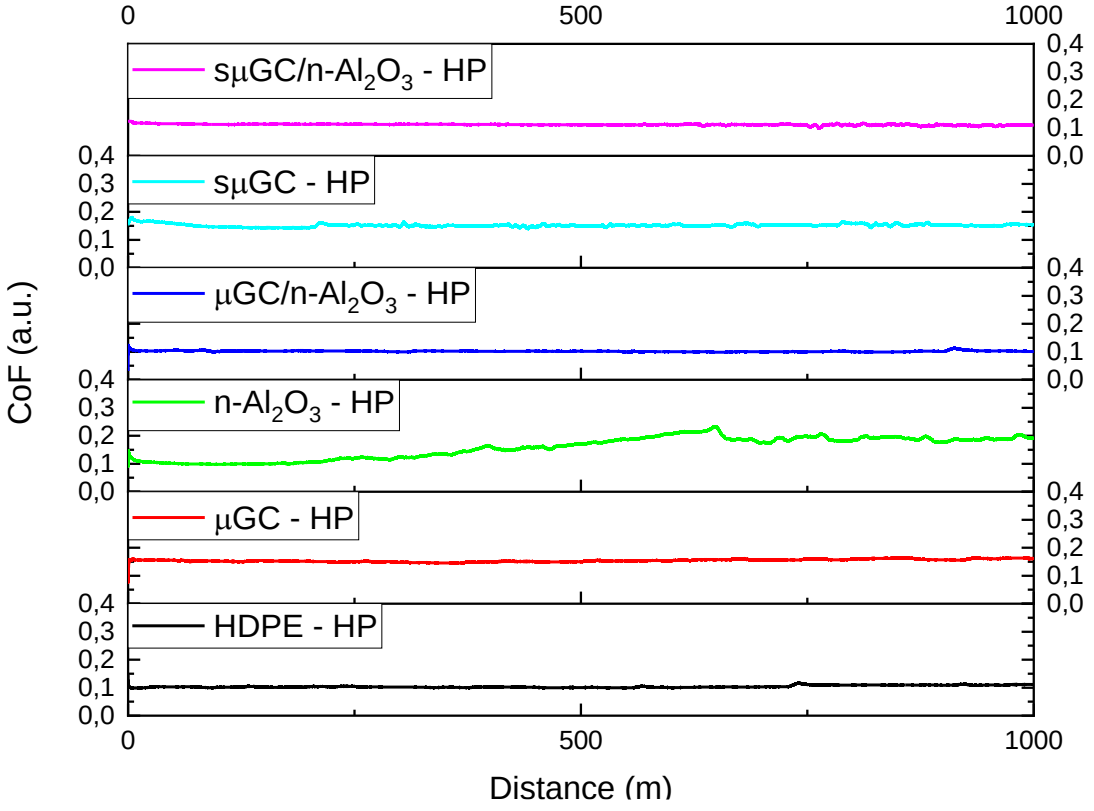

Figure 36 Coefficient of friction vs. distance for hot-pressed samples with alumina ball countersample

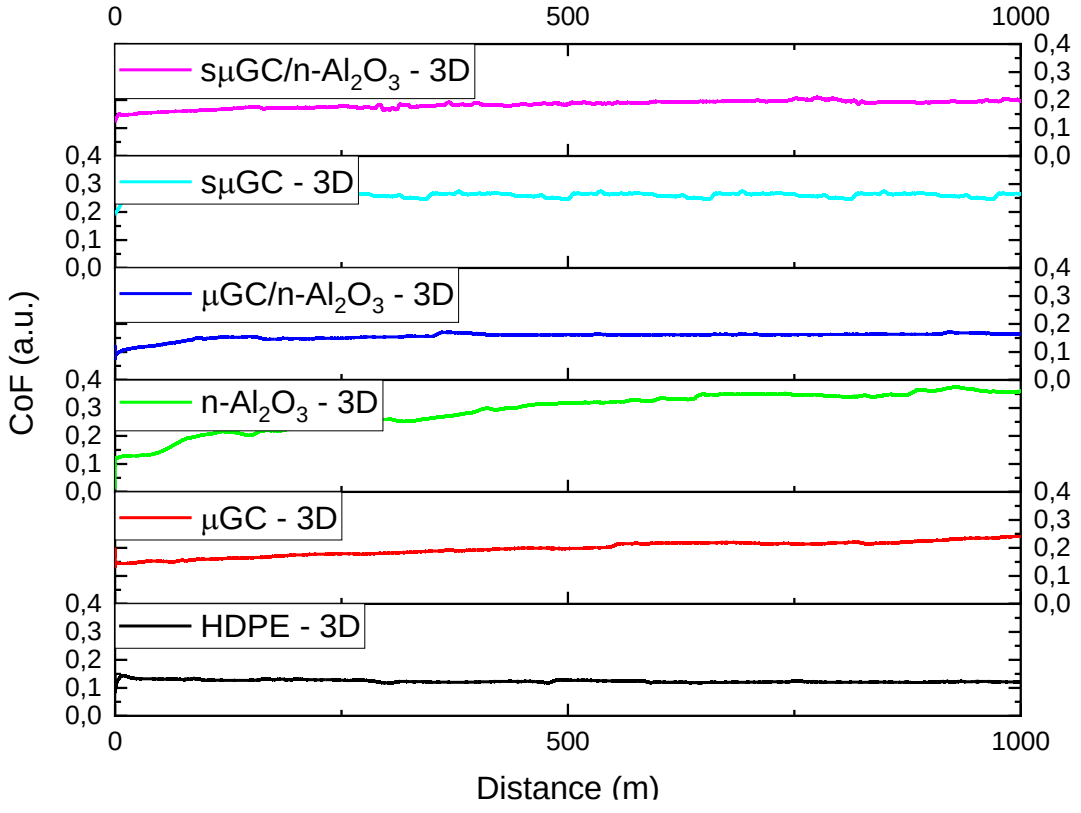

Figure 37 Coefficient of friction vs. distance for 3D printed samples with steel ball countersample

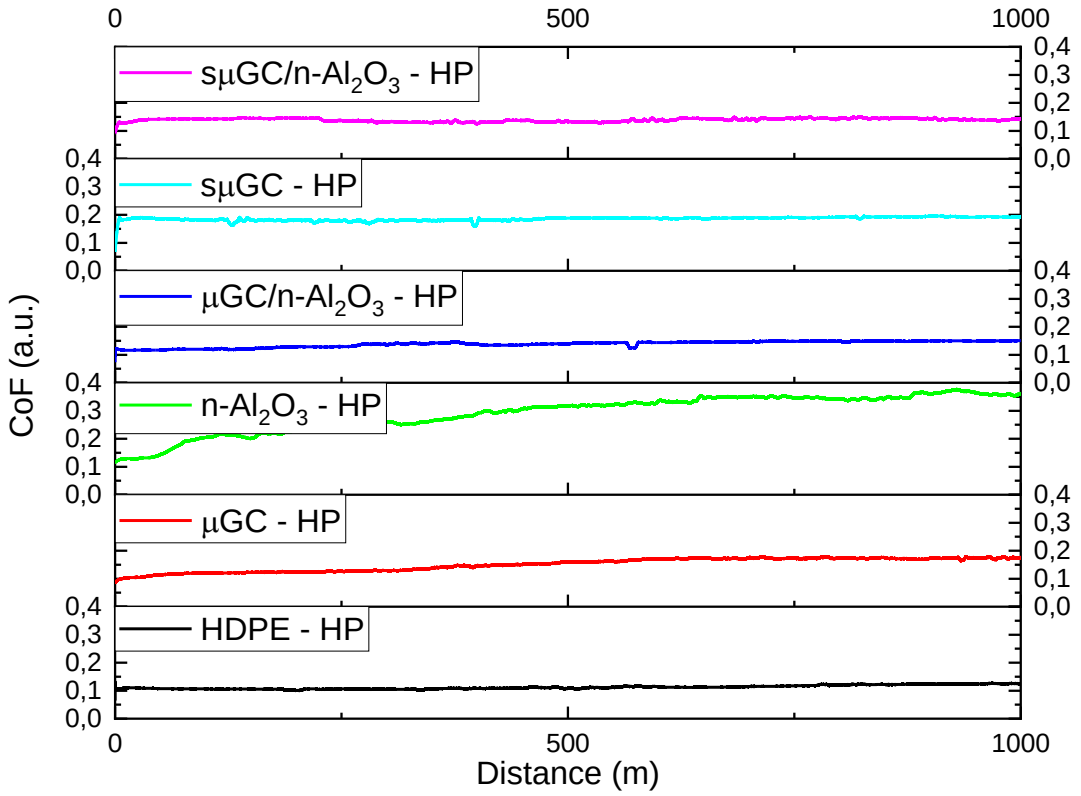

Figure 38 Coefficient of friction vs. distance for hot-pressed samples with steel ball countersample

Table 13 Results of friction coefficient and mass wear rate for samples wear versus alumina ball.

Sample name	Hot Pressed		3D printed	
	CoF	Wear rate	CoF	Wear rate
HDPE	0.10±0.03	0.00%	0.10±0.03	0.00%
uGC	0.15±0.05	0.00%	0.15±0.04	0.00%
Al2O3	0.19±0.07	0.30%	0.36±0.14	2.60%
uGC/Al2O3	0.10±0.03	0.10%	0.21±0.08	0.60%
suGC	0.15±0.05	0.10%	0.22±0.08	0.80%
suGC/Al2O3	0.11±0.03	0.00%	0.20±0.07	0.40%

Table 14 Results of friction coefficient and mass wear rate for samples wear versus steel ball.

Sample name	Hot Pressed		3D printed	
	CoF	Wear rate	CoF	Wear rate
HDPE	0.11±0.03	0.00%	0.12±0.04	0.10%
uGC	0.17±0.05	0.00%	0.20±0.07	0.50%
Al2O3	0.35±0.13	0.30%	0.34±0.12	2.10%
uGC/Al2O3	0.14±0.04	0.00%	0.16±0.05	0.10%
suGC	0.19±0.06	0.10%	0.26±0.09	1.40%
suGC/Al2O3	0.14±0.04	0.10%	0.19±0.07	0.80%

The chosen wear tracks of tested samples are presented in Fig. 39-45. In the neat HDPE sample, the dominant mechanism is plastic deformation of the polymer matrix. There are visible particles from alumina ball and HDPE debris attached to the surface. They are wear products formated during friction. Some of HDPE debris are also attached to surface of alumina ball (Fig.46). In the case of n-Al_2O_3 composites, plastic deformation along with microcutting was determined. The most probable explanation is cracking and pulling out of alumina particles from the matrix, which then cut the surface before being squished back into the polymer. For composites with μGC and sμGC, plastic deformation is visible along with slight plastic flow and wear particles attached to the surface. However, the wear tracks with GC are smoother, and the effects of plastic flow are less visible than on neat HDPE. This might be a result of carbon tribo-film formation (Fig. 46). In this case, the carbon layer acts as a solid lubricant and might prevent further wear. The mechanism described above was observed for both alumina and steel counterparts. However, the difference was visible for the composite containing both GC and n-Al_2O_3. In both cases, plastic deformation and plastic flow of the matrix were observed. Also, in both samples, the alumina particles most probably wore out from the surface and reattached to the polymer matrix. However, more alumina fellings is visible in the sample than the steel fellings worn during the test against the steel counterpart. This suggests that the alumina particles cracked and were not pressed into the matrix but instead remained loosely attached to the worn surface. In the case of the alumina counterpart, the particles seem to form agglomerates that were pressed into the matrix.

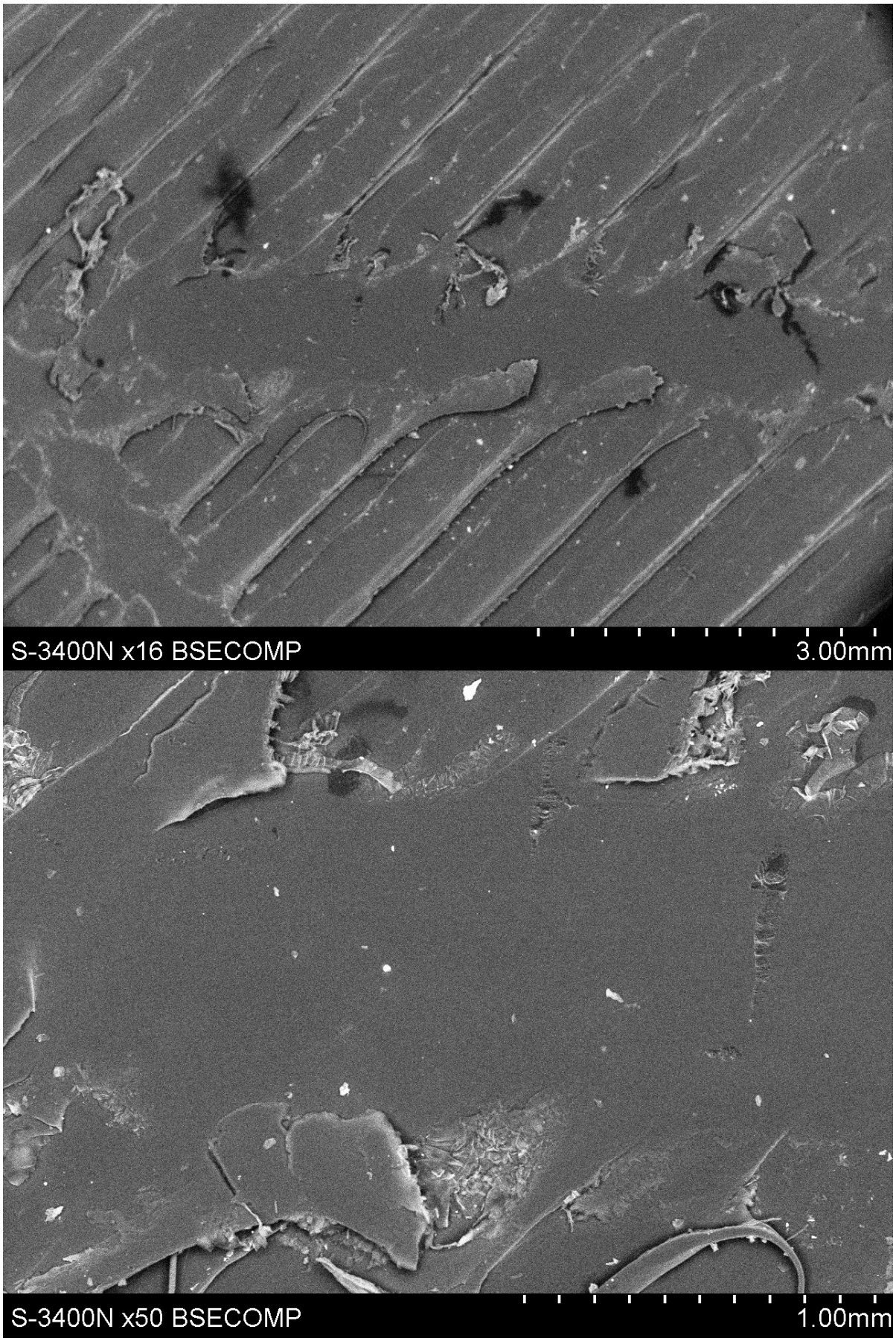

Figure 39 SEM micrograph wear track of 3D printed HDPE sample after friction test with alumina ball counterpart

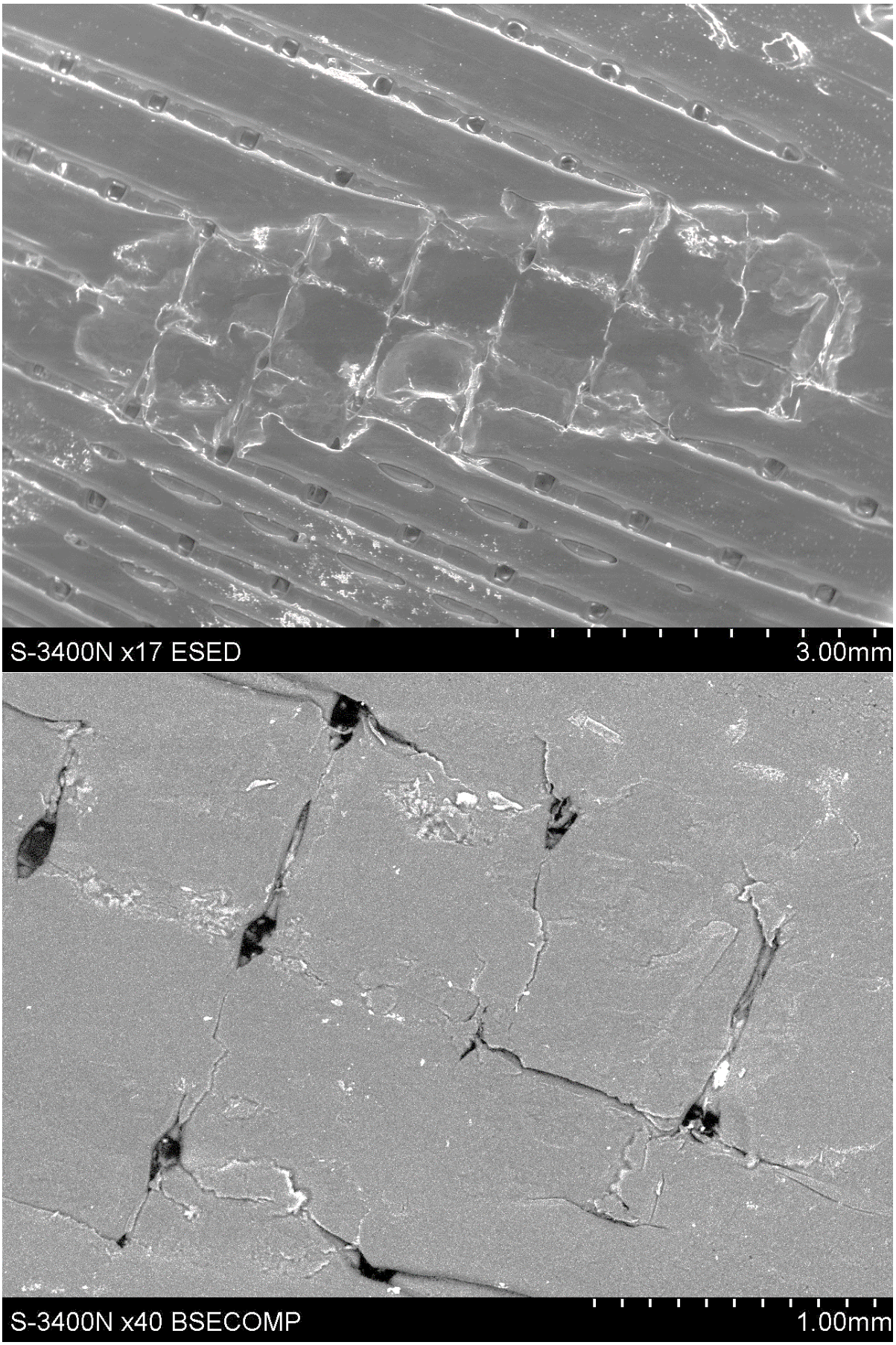

Figure 40 SEM micrograph wear track of 3D printed HDPE after friction test with steel ball counterpart

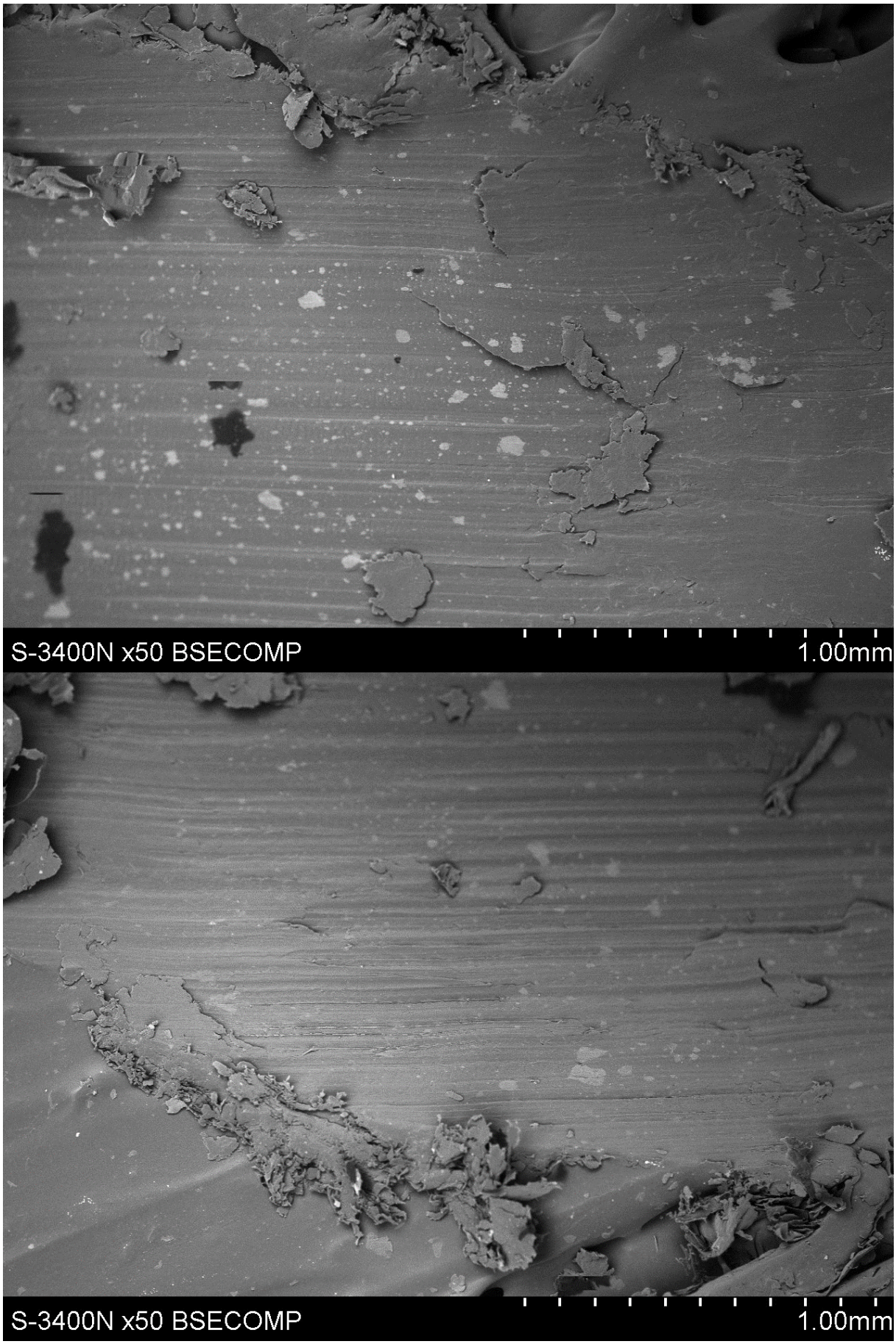

Figure 41 SEM micrograph wear track of n-Al_2O_3 sample after friction test with alumina ball counterpart

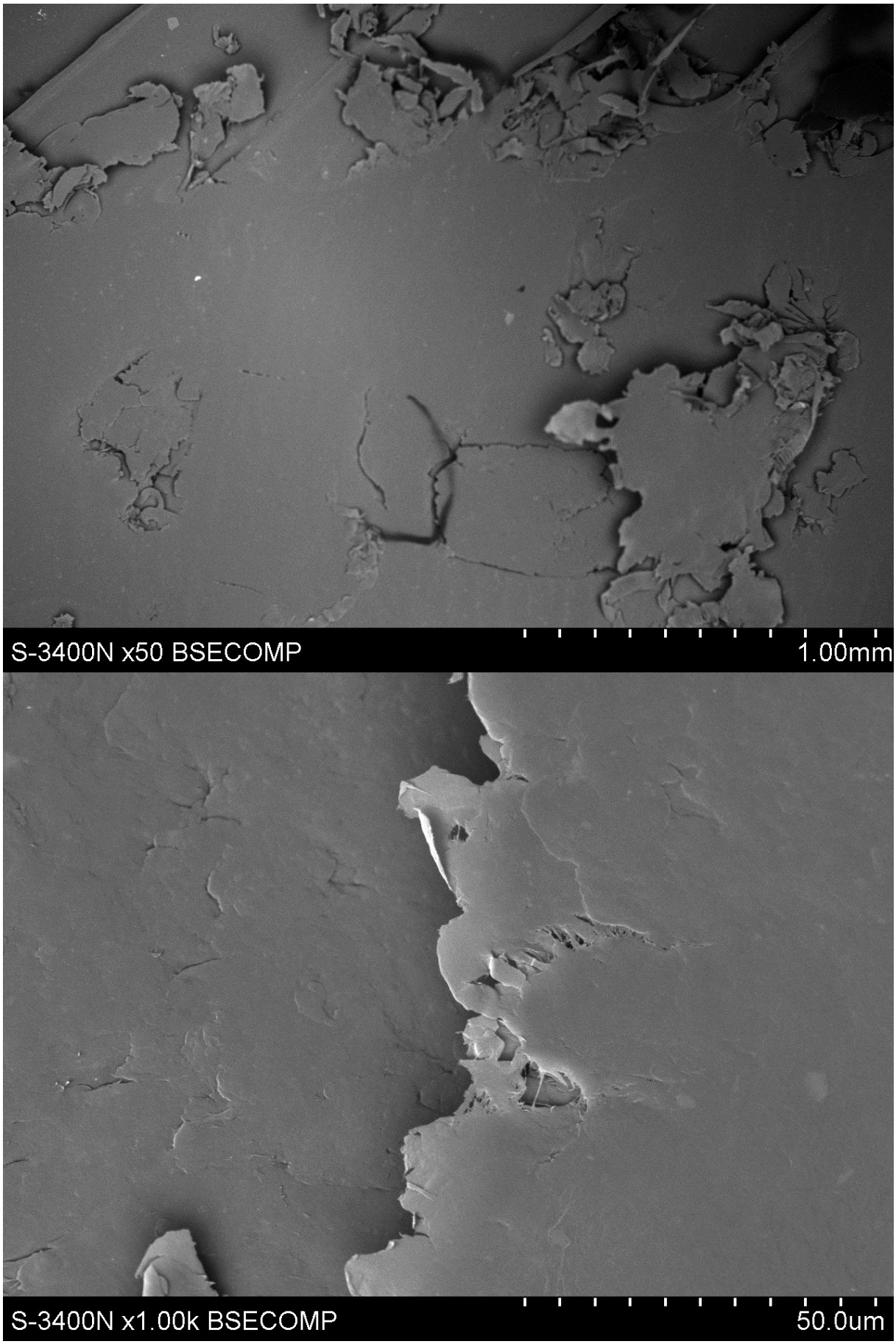

Figure 42 SEM micrograph wear of µGC sample after friction test with alumina ball counterpart

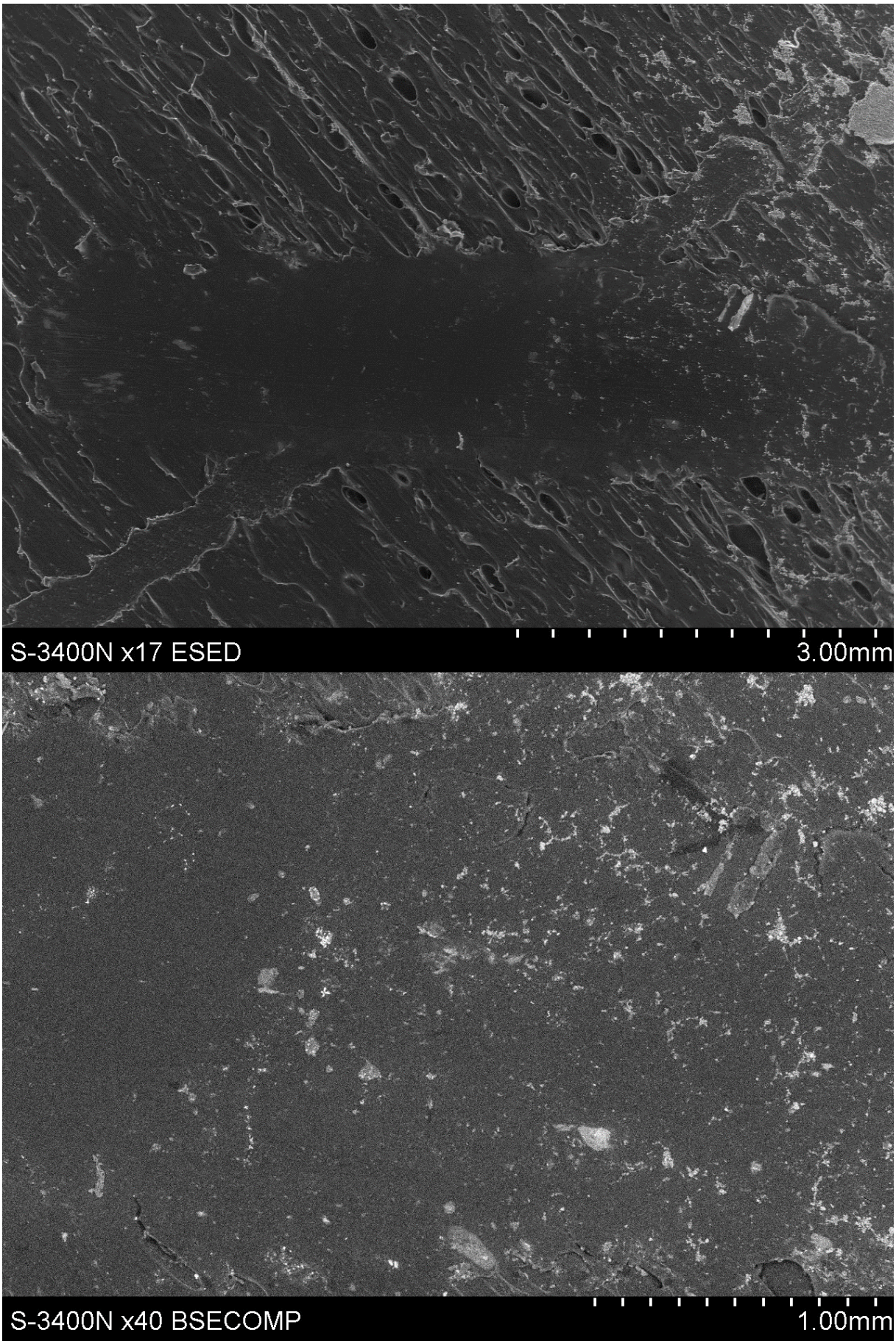

Figure 43 SEM micrograph wear of μGC/Al_2O_3 sample after friction test with steel ball counterpart

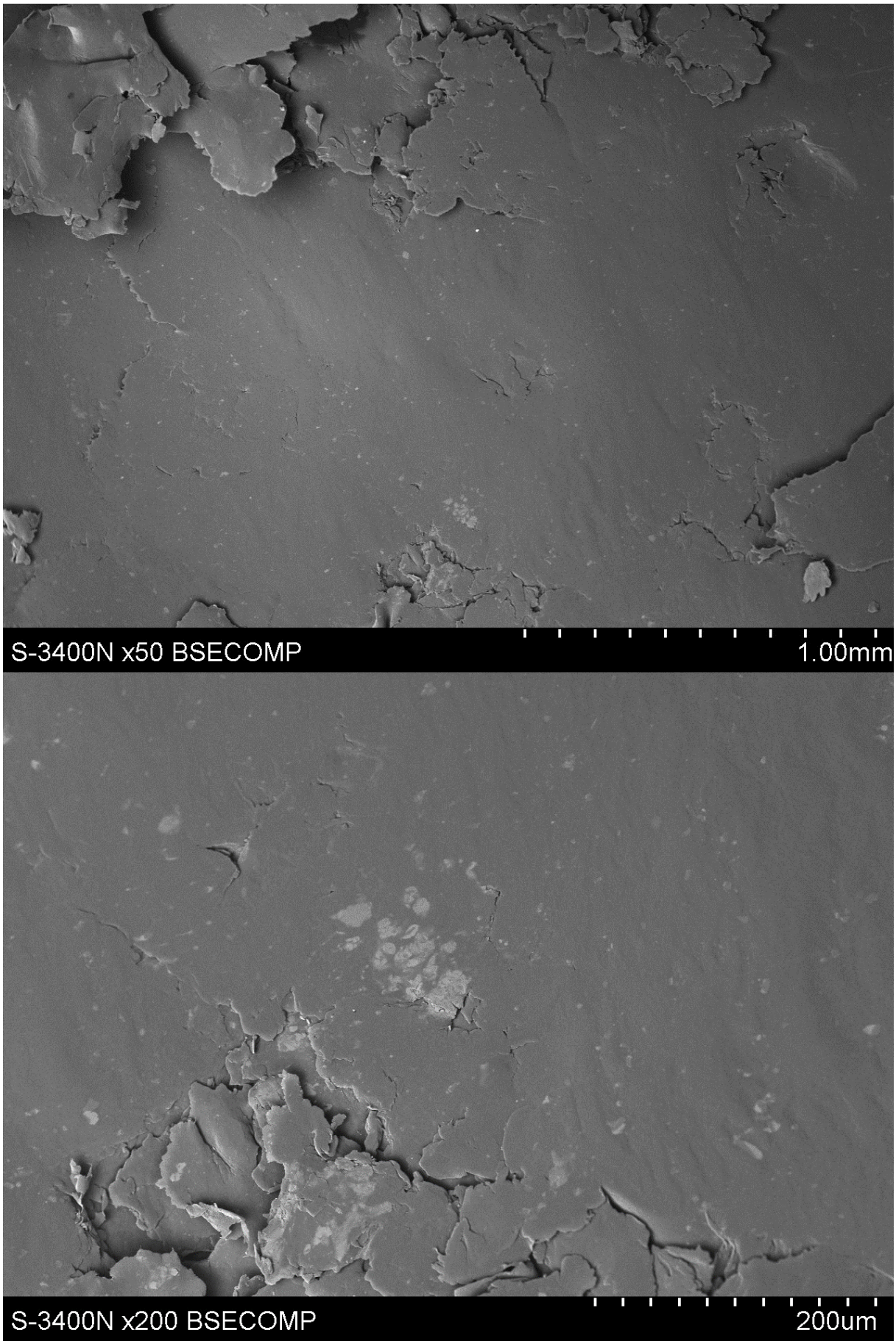

Figure 44 SEM micrograph wear track of µGC/Al2O3 sample after friction test with alumina ball counterpart

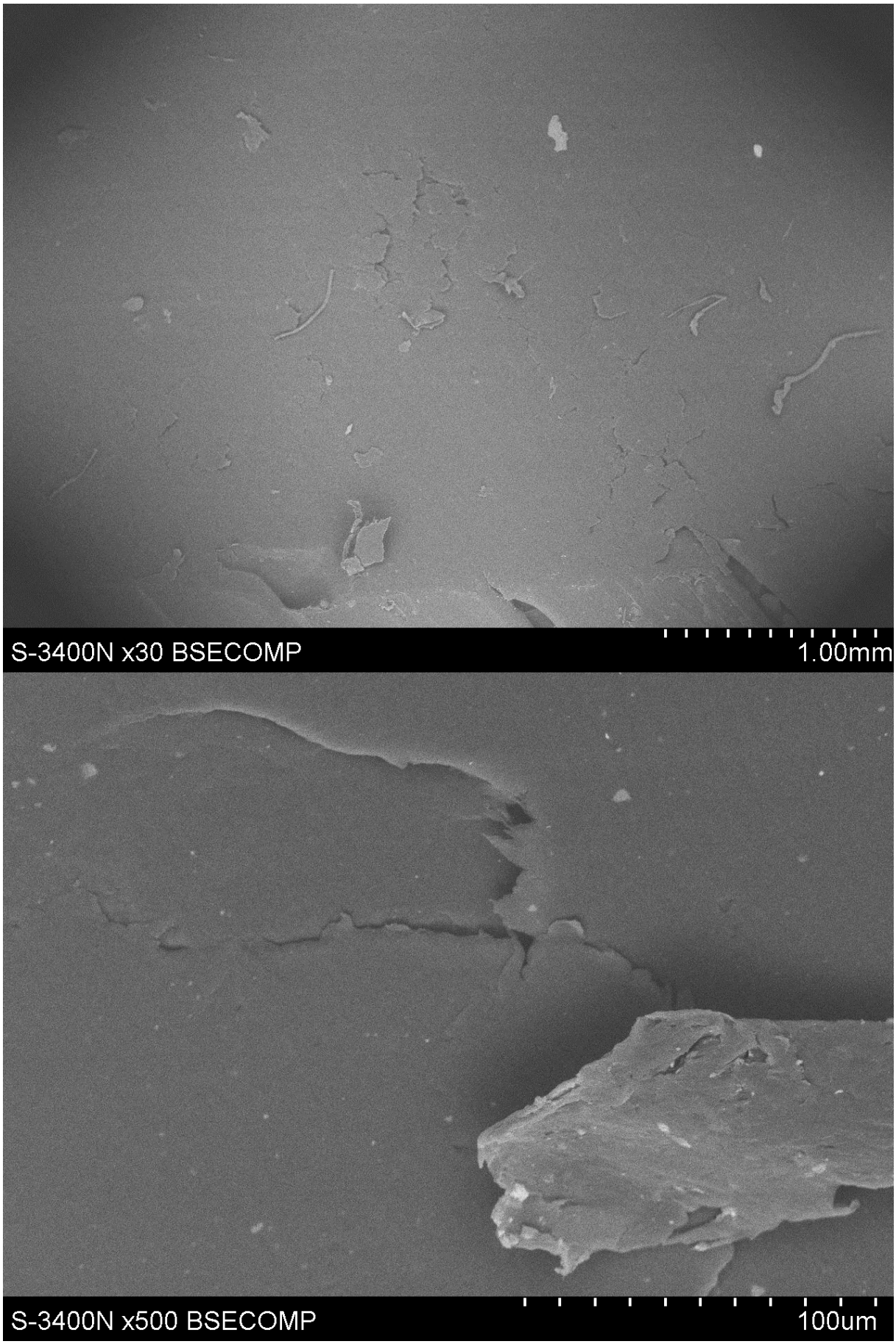

Figure 45 SEM micrograph wear track of sμGC sample after friction test with alumina ball counterpart

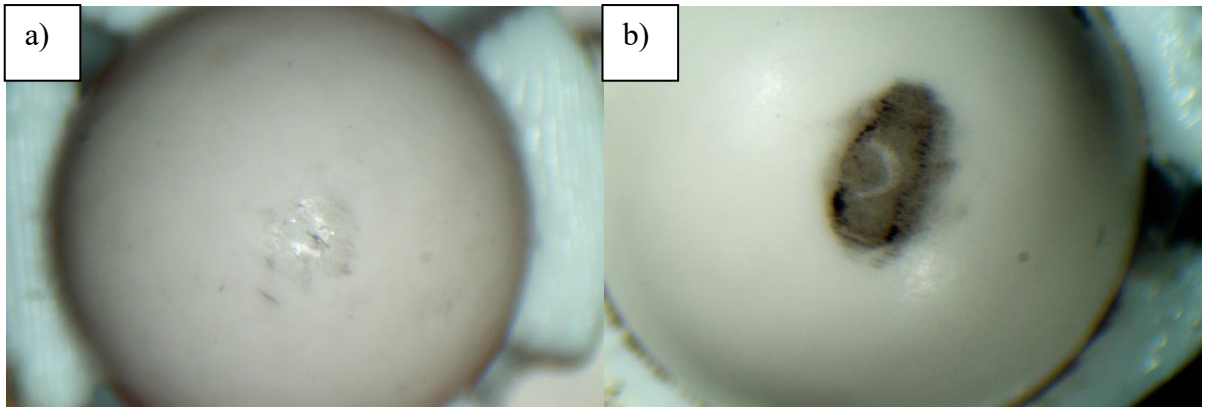

Figure 46 Macrograph of alumina ball surface after wear test: a) neat HDPE, b) µGC composite.

The difference in this behavior might be correlated with different plastic flow. The steel ball has higher conductivity than the alumina ball, which leads to more efficient heat dissipation from the friction surface, resulting in reduced plastic flow and hence more loosely attached alumina particles. In both cases, the formation of a carbon tribo-film should occur, which is suggested by both the wear rate and CoF. The proposed mechanism is visualised in Fig. 47.

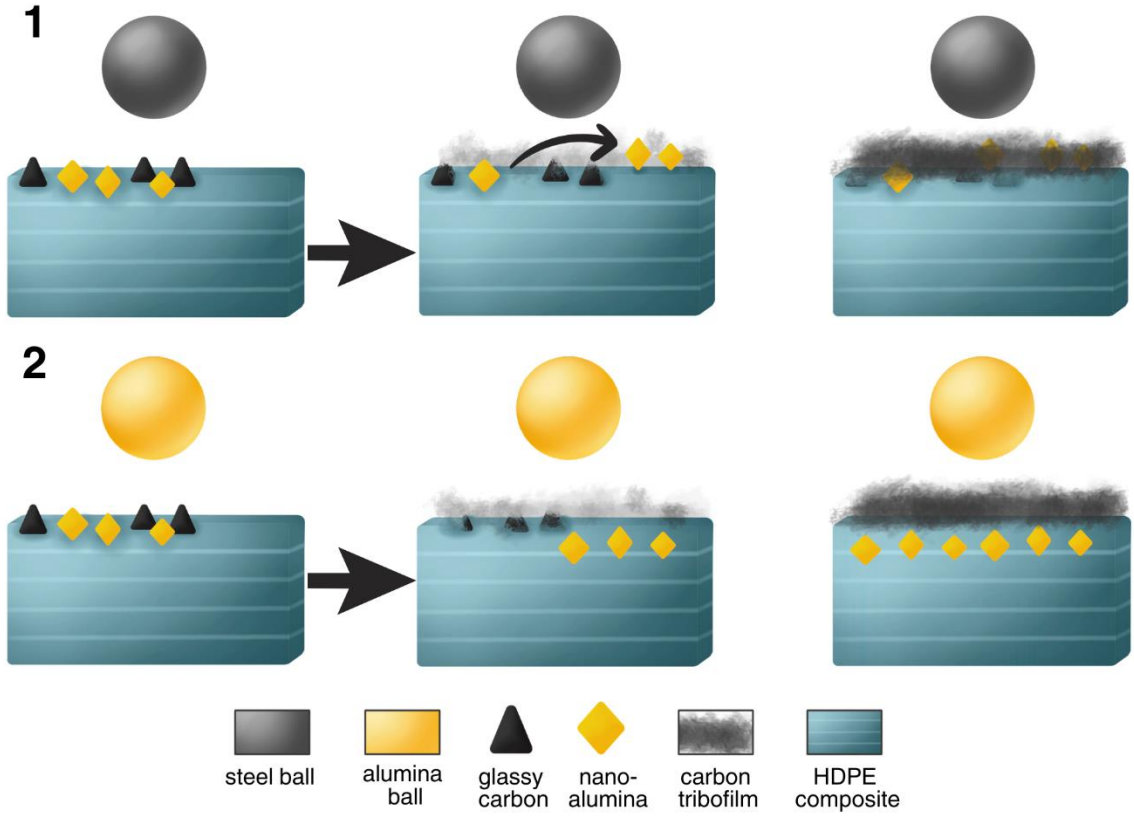

Figure 47 Scheme of proposed wear behaviour in composites with GC and n-Al_2O_3 particles: 1 – formation of carbon film with alumina particles attached to the surface, 2 - formation of carbon film with alumina particles pushed into the surface

3.3 Piezoelectric composites

3.3.1 Materials preparation

The two types of samples were prepared: the first for electrical conductivity testing and the second for piezoelectric response test. The composites for conductivity tests were prepared in two series containing μGC or sμGC at various volume content (φ). The composites were prepared by dissolving HDPE in xylene (Warchem, Warsaw, Poland) and mixing with the filler with use of magnetic stirrer. The procedure of preparing composites was as follow:

1. Mixing HDPE with GC powder in glass bottle.
2. Addition of xylene to the reaction bottle. The mass proportion of xylene added to HDPE was 6:1.
3. Deagglomeration of GC powder by ultrasonic mixing.
4. Putting the reaction bottle to oil bath.
5. Heating up mixture to 150.0˚C until HDPE dissolves.
6. Moving the reaction bottle in oil bath to magnetic stirrer.
7. Slow ramping of stirring speed up to 300 RPM.
8. Stirring for 5 min.
9. Pouring the mixture to glass beaker and leaving for12 hours to dry.
10. Grinding the obtained powder (Fig. 48).
11. Drying at 150.0˚C by 10 minutes to remove leftover of xylene.

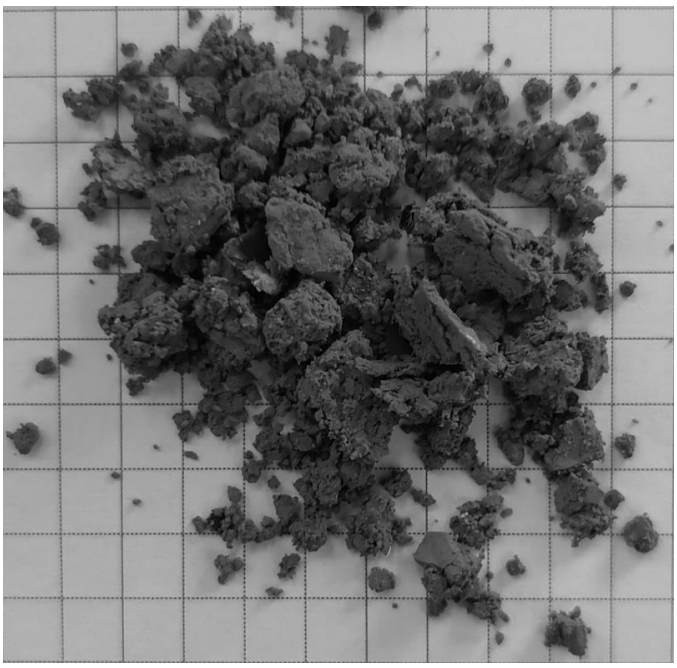

Figure 48 Macrograph of HDPE/GC composite powder after drying

The obtained compositions are presented in Table 15. The samples for conductivity test were hot-pressed with the same process parameters as those described in Chapter 3.2.1.

Table 15 The compositions of composites for conductivity testing

GC, vol%	µGC	sµGC
1.0	µ1R	sµ1R
2.0	µ2R	sµ2R
3.0	µ3R	sµ3R
5.0	µ5R	sµ5R
7.0	µ7R	sµ7R
10.0	µ10R	sµ10R
12.0	µ12R	sµ12R
14.0	µ14R	sµ14R
16.0	µ16R	sµ16R
18.0	µ18R	sµ18R
20.0	µ20R	sµ20R

The samples for piezoelectric response tests were prepared using antimony sulfoiodide (SbSI) nanowires xerogel. The xerogel was manufactured and provided by Institute of Physics – Centre for Science and Education at Silesian University of Technology. The procedure of obtaining SbSI xerogel is described within previous studies [86], [92]. The composites with SbSI were prepared with the same procedure as composites for conductivity test – the 11-step procedure is described above. However, due to the sensitivity of SbSI to prolonged exposure to elevated temperatures, the xerogel was added immediately after reaching a stirring speed of 300 RPM during the ramping process (step 7 of the procedure). Then, the obtained composite was cut into small pieces and extruded with the same procedure as described in Chapter 3.2.1. The obtained filament and the composition are presented in Table 16 and in Fig. 49.

Table 16 The hybrid HDPE-GC-SbSI composites compositions: ω - % mass content, φ - %volume content

Component	SbSI		SbSI/µGC		SbSI/sµGC	
	ω	φ	ω	φ	ω	φ
HDPE	80.0%	95.3%	72.7%	89.6%	72.7%	89.6%
SbSI	20.0%	4.7%	18.2%	4.4%	18.2%	4.4%
µGC	-	-	9.1%	6.0%	-	-
sµGC	-	-	-	-	9.1%	6.0%

Figure 49 Piezoelectric composite filaments based on HDPE filled with: SbSI, SbSI/µGC and SbSI/sµGC

The piezoelectric composite filaments were used for FDM printing 3D samples for piezoelectric test. The used FDM 3D printing process was described in Chapter 3.2.1. However, the printing temperature was raised to 220˚C due to drastic drop of MFR in comparison with neat HDPE. Also, the single layer height was increased to 0.20 mm. The sample dimensions were 15x30x0.6 mm and the schematic representation is presented in Fig. 50.

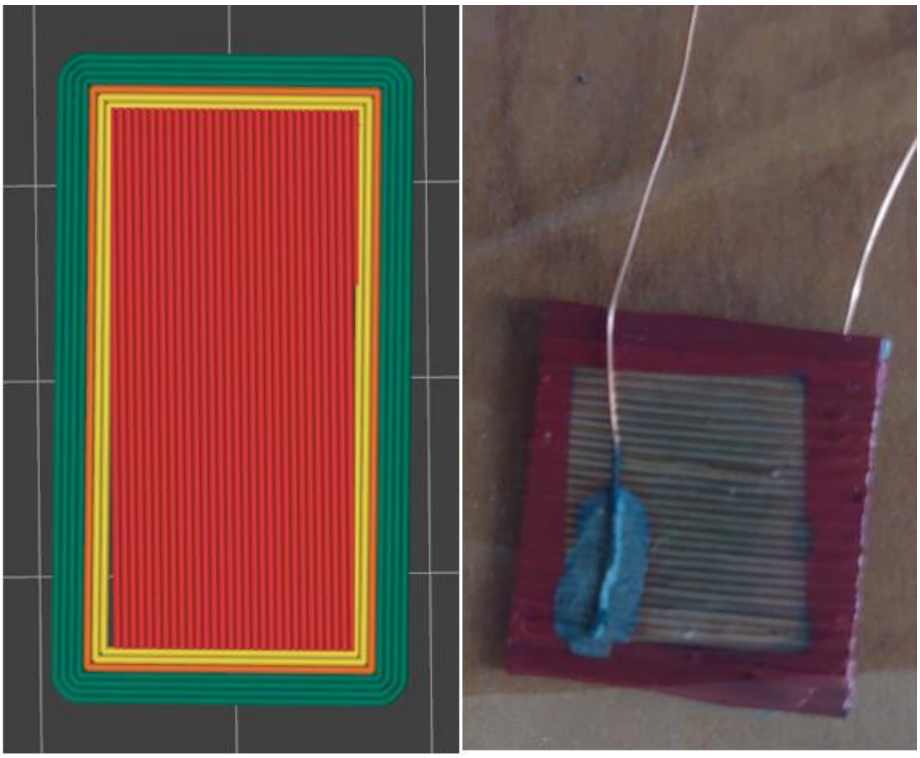

Figure 50 Scheme of FDM 3D printed sample for piezoelectric test (left) and real photo of fabricated and instrumented sample (right)

3.3.2 Research methodology

The conductivity test for HDPE/GC composites was measured using Keysight 6430 (Keithley Instruments, Cleveland, USA). The gold electrodes were deposited on the top and bottom surfaces of each sample and then a copper wire were attached to each surface (see Fig. 50). The voltage vs. current characteristic was measured by changing the applied voltage. The range of voltage variation was selected depending on the sample. The sample resistance was determined by applying linear regression to obtained data. The conductivity (σ) was calculated by following equation:

$$\sigma = \frac{L}{RA} \qquad \text{(Eq. 8)}$$

where: R - sample resistance [ohm], A - electrode area (~2.18*10^{-4} m^2), L - sample thickness [m].

The percolation threshold was found by fitting the experimental results to the Eq.9:

$$\sigma = \sigma_0(\varphi - \varphi_c)^t \qquad \text{(Eq. 9)}$$

where: σ_0 – adjustable parameter [S/m], φ – the volume fraction of glassy carbon, φ_c – percolation threshold, t – critical exponent. The fitting was performed in the range for which $\sigma \sim (\varphi - \varphi_c)$ relation becomes linear.

To observe the SbSI nanowires distribution in the polymer matrix, extruded filaments were cooled down in liquid nitrogen and broken mechanically in order to obtain possibly smooth surface of the cross-section. The cross-section of extruded material was investigated with use of the Hitachi S-3400N microscope at 15.0 kV acceleration voltage and under low vacuum conditions.

The piezoelectric response was measured with Keysight DSOX3054T digital oscilloscope (Keithley Instruments, Cleveland, USA). The samples were prepared with the same procedure as samples for the conductivity tests. The stress to the samples was applied by using a pneumatic gun (Zoraki HP-01-2). The pressure of air stream was regulated by number of pumping. The output pressures were 4.86, 11.54 and 17.03 bar. The piezoelectric response (output voltage) over time was registered. The detailed description of this original method has been previously posted within the work [93]. The obtained data was used to calculate power density per area (P_s), which was determined using following equation:

$$P_s = \frac{1}{R_o A} \int_{t_0}^{t_1} U^2 dt \qquad \text{(Eq. 10)}$$

where: R_o – oscilloscope internal impedance (1MΩ), A – air stream surface area (23.76 mm^2), t_0/t_1 – peak's start and end position [s], U – voltage [V].

3.3.3 *Results – electric conductivity and piezoelectric response*

The Fig. 51 and Table 17 present the results of conductivity tests. The sμGC composite exhibits higher conductivity than the samples with μGC. Also, the composites with sμGC have lower percolation threshold. This effect probably relates to better distribution of conductive filler in polymer matrix. That allows more effective formation of conductive path within the material and hence higher conductivity and lower percolation threshold for the sμGC composite.

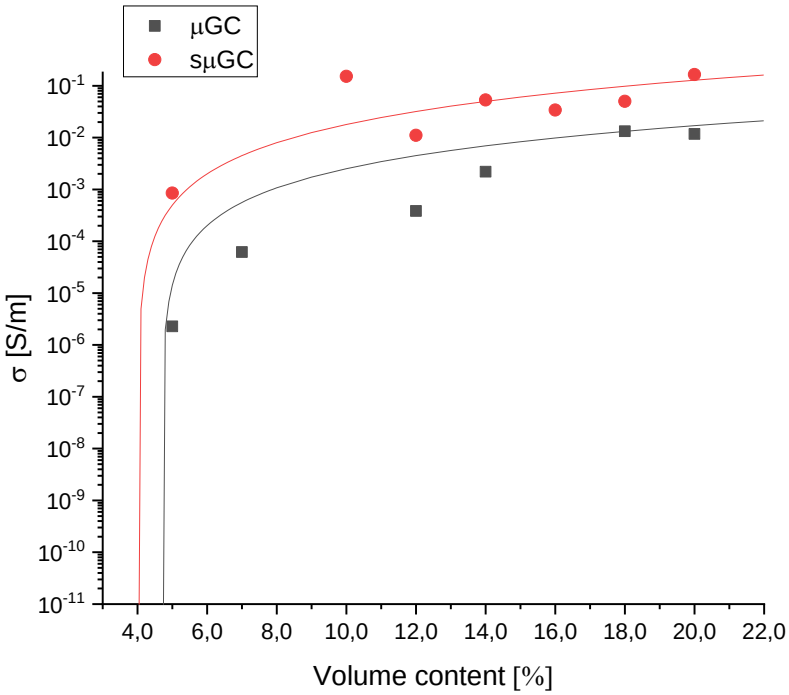

Figure 51 Conductivity of the HDPE/GC composites

Table 17 Fitting parameters of the percolation curve – according to Equation 9

Sample type	Φ_c	t	σ_0 [S/m]
μGC	4.7 %	1.8	0.5
sμGC	4.0 %	2.0	5.0

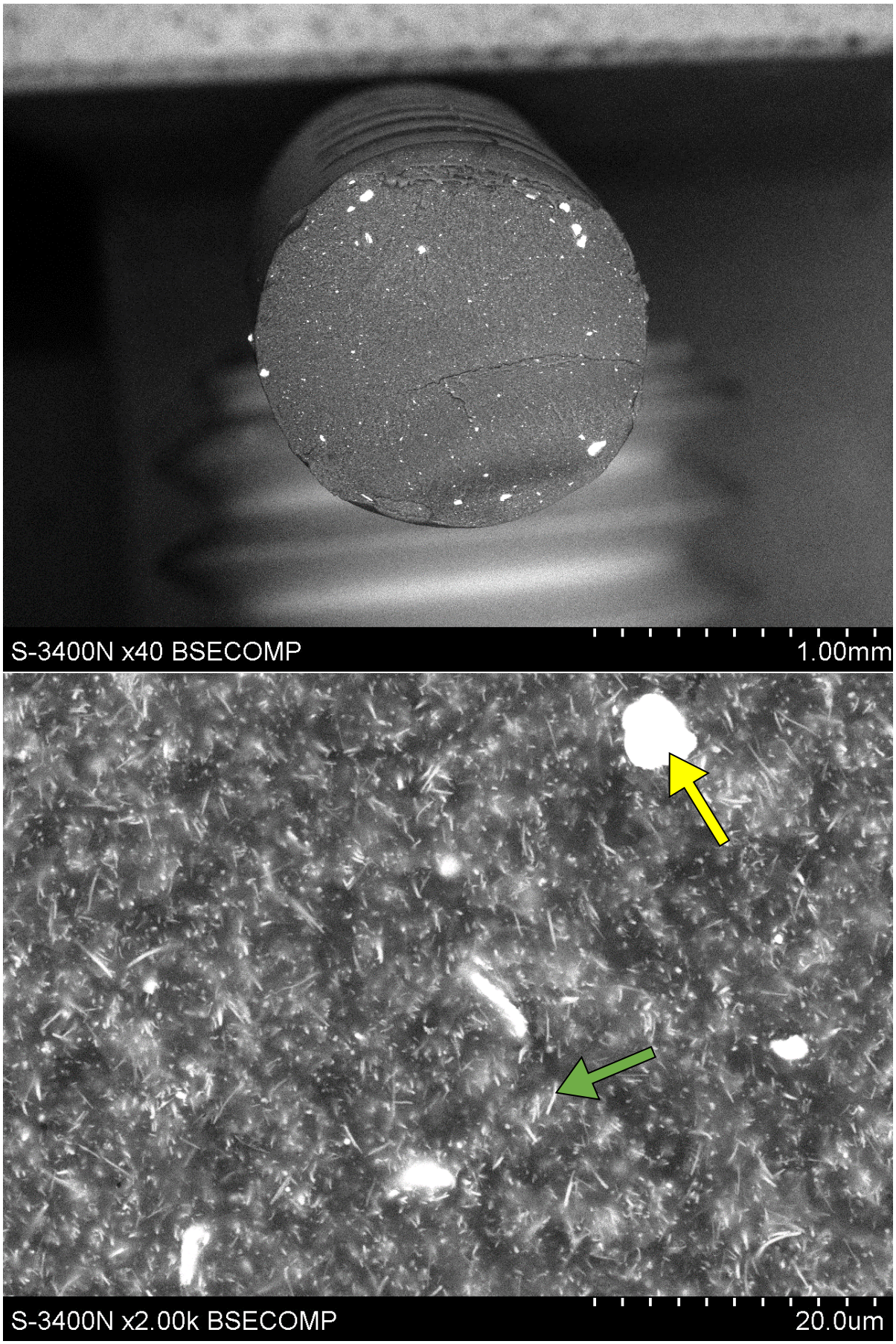

Figure 52 SEM micrograph of HDPE/SbSI composite filament cross-section observed at different magnification: yellow arrow – SbSI agglomerate, green arrow – SbSI single wire

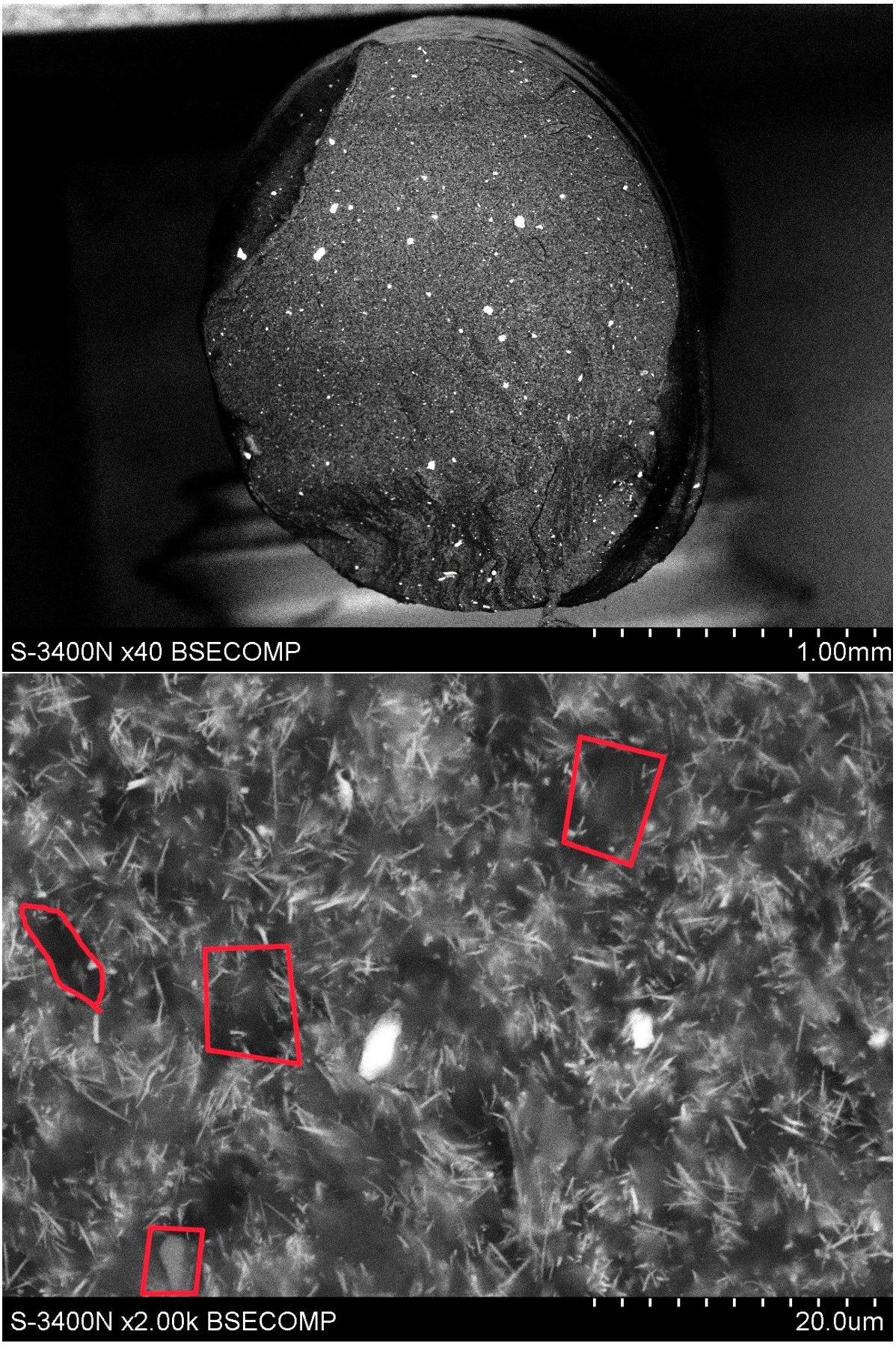

Figure 53 SEM micrograph of HDPE/SbSI/μGC hybrid composite filament cross-section observed at different magnification

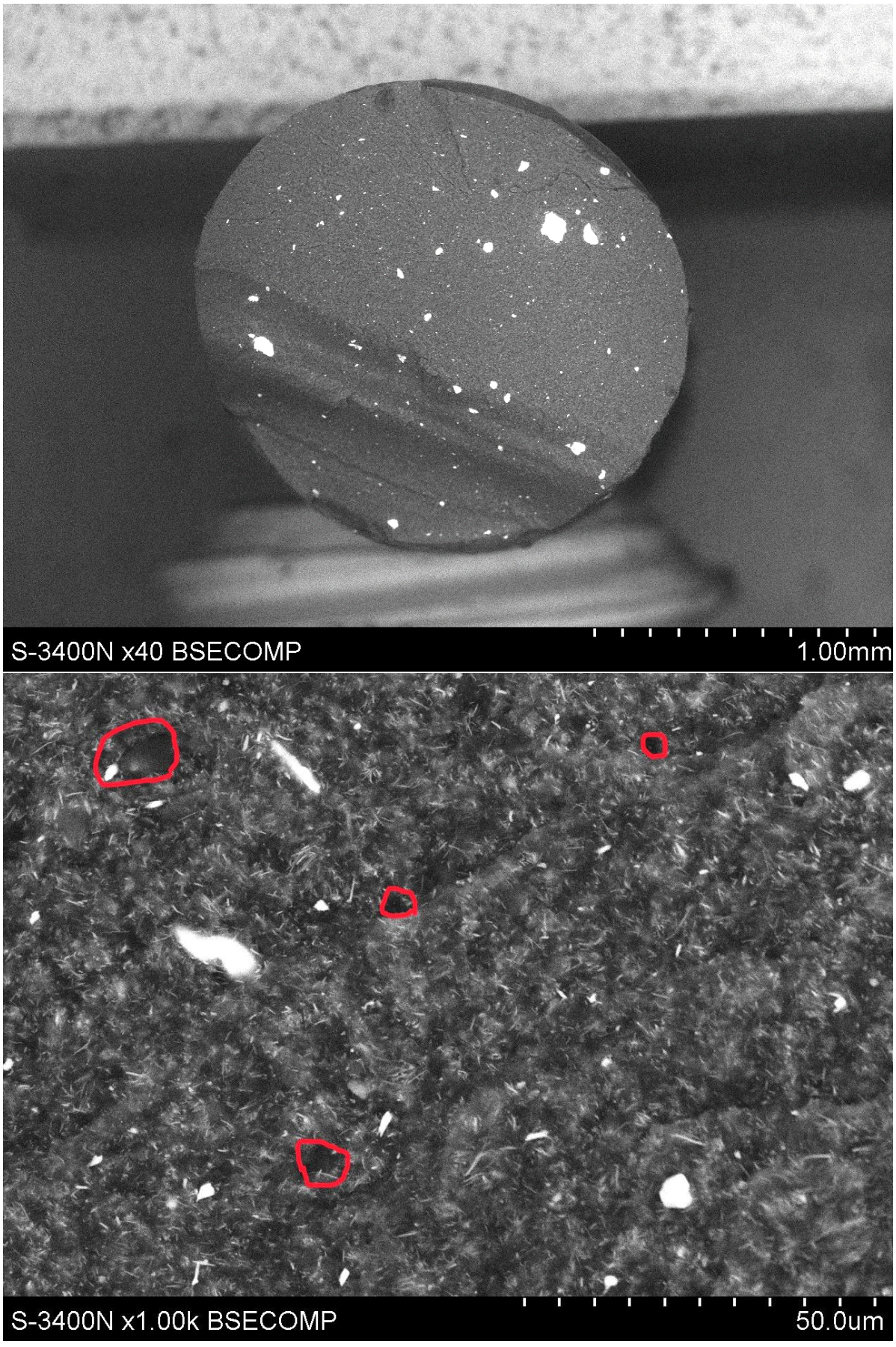

Figure 54 SEM micrograph of HDPE/SbSI/sμGC hybrid composite filament cross-section observed at different magnification

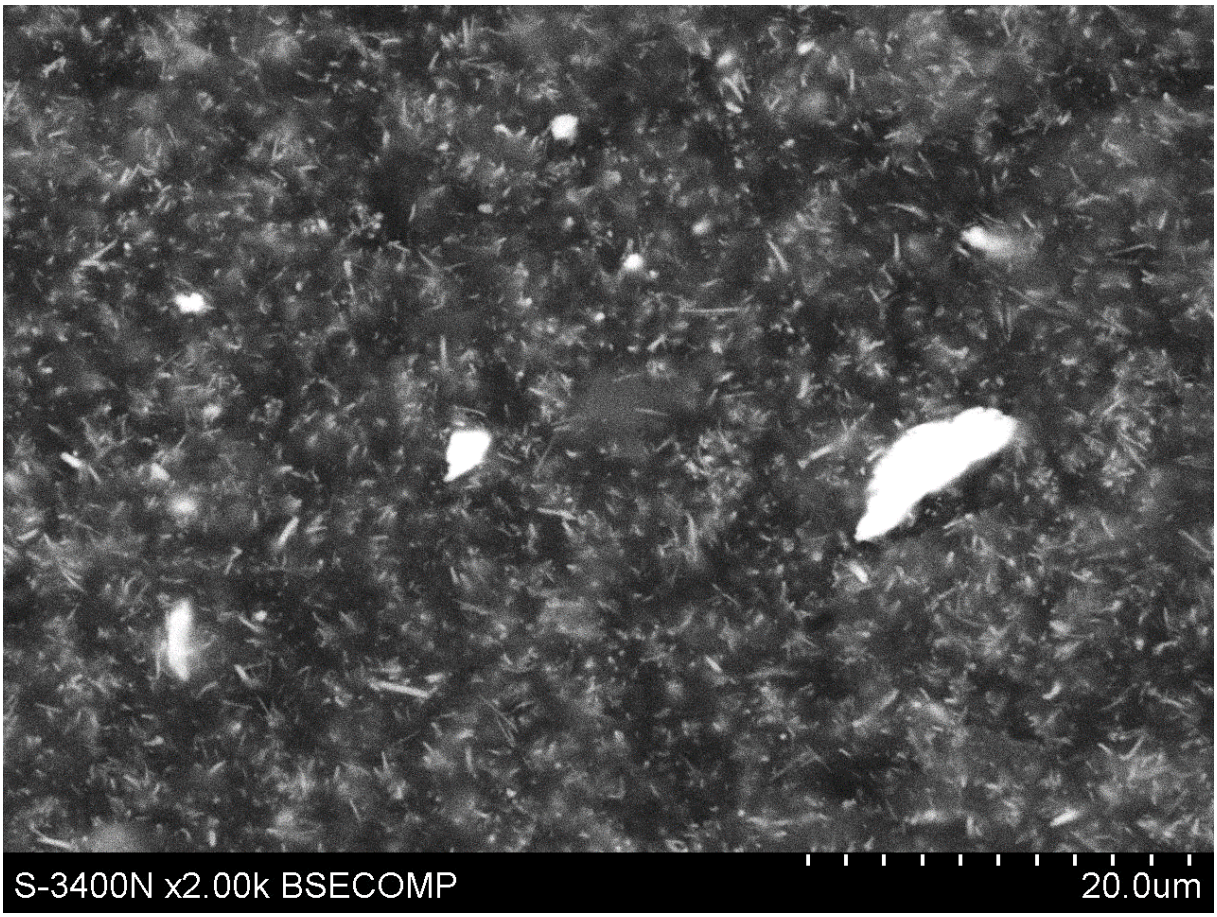

Figure 55 SEM micrograph of HDPE/SbSI/sμGC hybrid composite filament cross-section – big magnification

The cross-sections of the composite filaments containing SbSI are presented at Fig. 52-55. Part of the nanowires form large, agglomerated particles with diameters around 10.0 μm, but most of them is deagglomerated and scattered. It is evenly distributed across the filament diameter and does not have a specific orientation. For filaments containing GC particles, it is not possible to certainly distinguish them from HDPE matrix. This is due to the lack of contrast between GC and HDPE. Also, SbSI may cover some of the GC reinforcement, which additionally disturb observation. However, some spots (red marks in Fig. 53 and 54) may be larger GC particles or areas from which particles were pulled out from the matrix during sample preparation. The similar voids and areas were observed within the cross-sections after mechanical testing (Chapter 3.2.3).

Fig. 56-60. present the results of piezoelectric tests. The output voltage for all samples shows a linear relationship with the shock load pressure applied during tests (Fig. 56). This result demonstrates the effectiveness of the used method for measuring the piezoelectric response of the composite samples. The samples with GC addition (hybrid composites) generate higher voltage output than the samples filled with only SbSI. The highest value of output voltage was observed for the composites containing sμGC. This dependence is observed for all applied pressures (Fig. 57-59). This phenomenon is related to the increase in the matrix conductivity. However, since the amount of SbSI has not been changed in the polymer matrix, and only SbSI generates piezoelectric response, the voltage output should not increase. In the Fig. 61, an increase in the power generated by samples (over 8-times increase between the SbSI filled one and the sμGC/SbSI filled one) was observed. This suggests that the addition of conductive filler increases the amount of generated P_s from sample's surface.

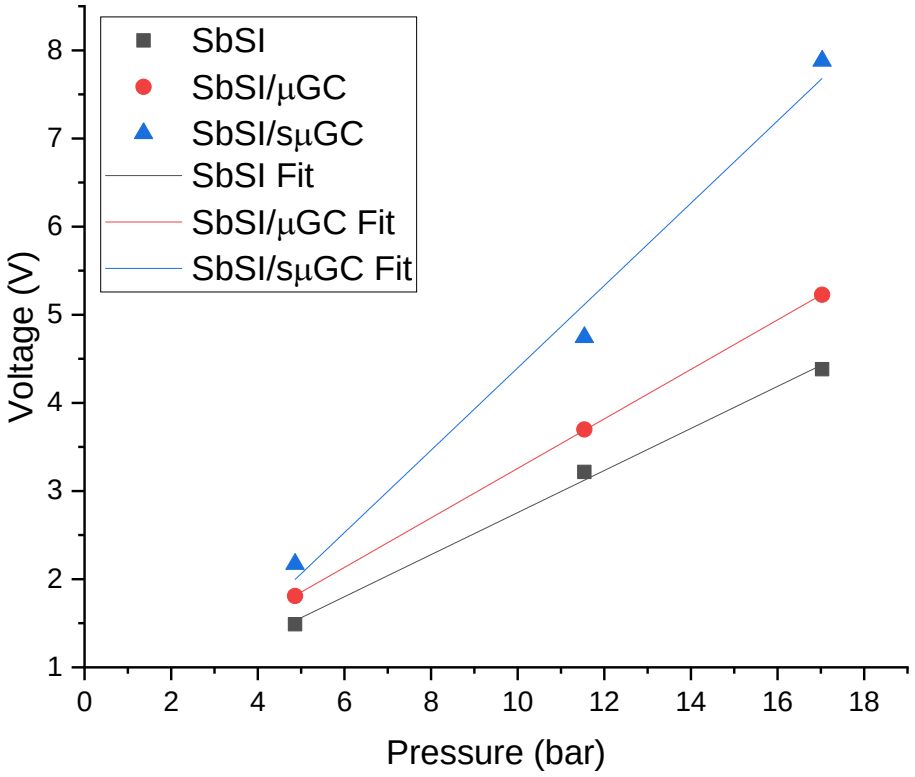

Figure 56 Results of output voltage dependence on test shock load pressure obtained for composites with different filling

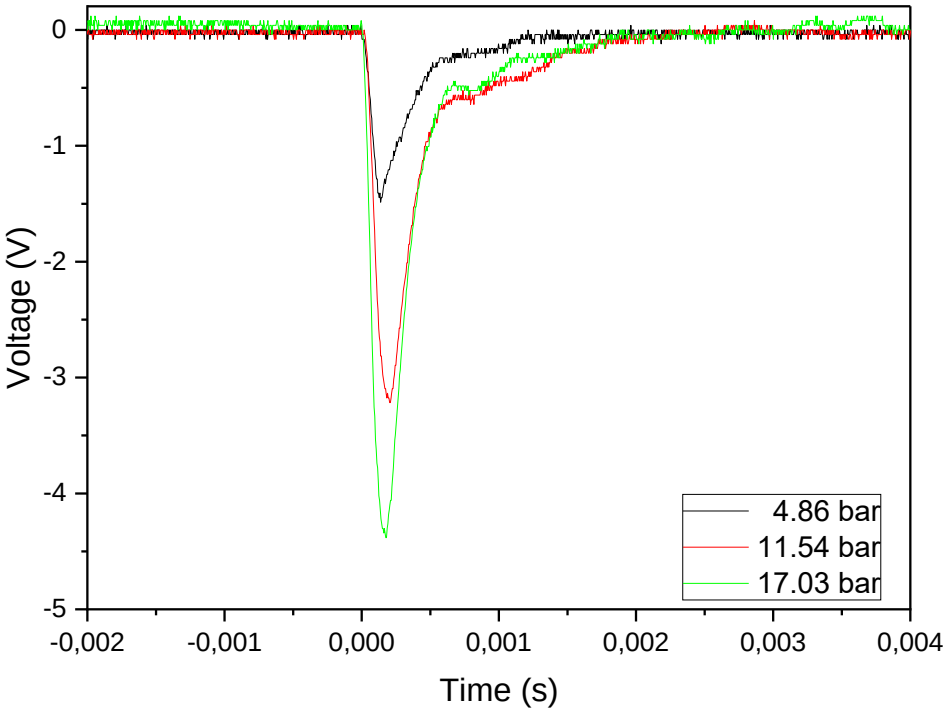

Figure 57 Results of output voltage of HDPE/SbSI composite

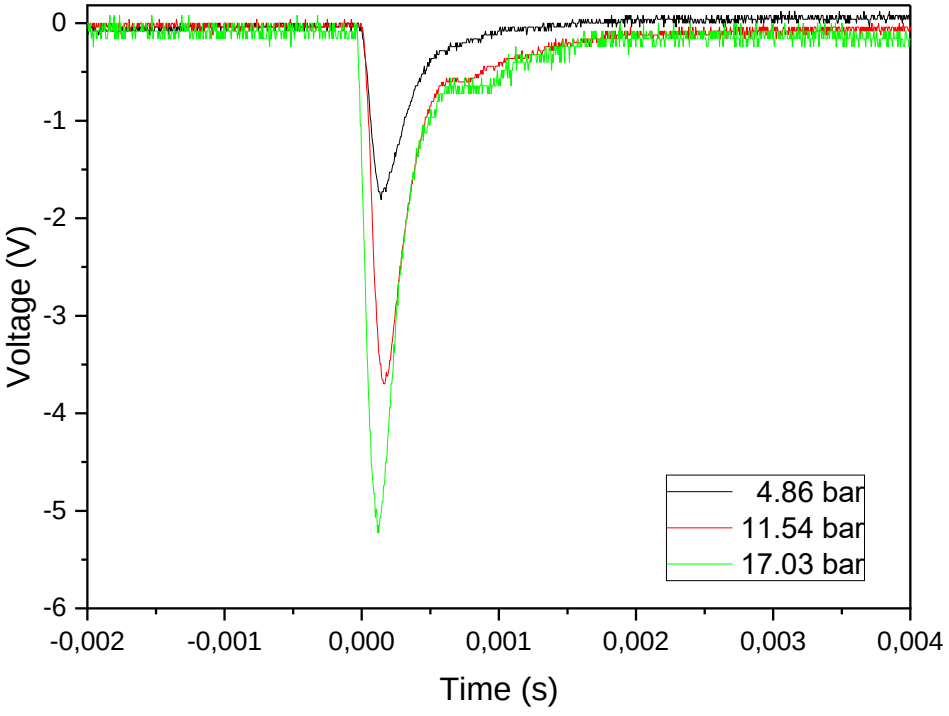

Figure 58 Results of output voltage of HDPE/μGC/SbSI composite

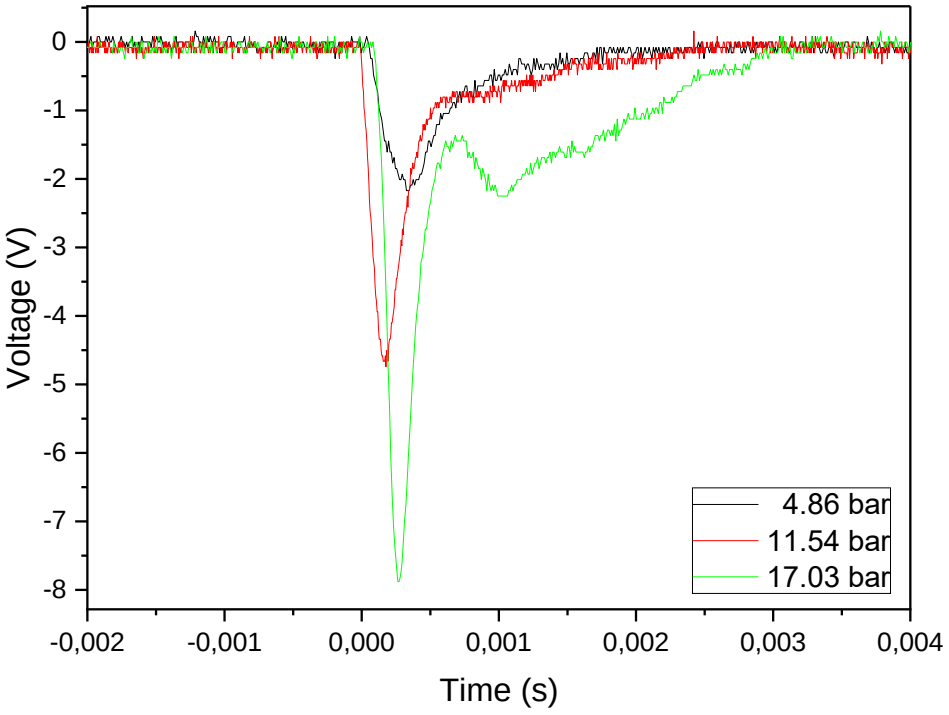

Figure 59 Results of output voltage of HDPE/sμGC/SbSI composite

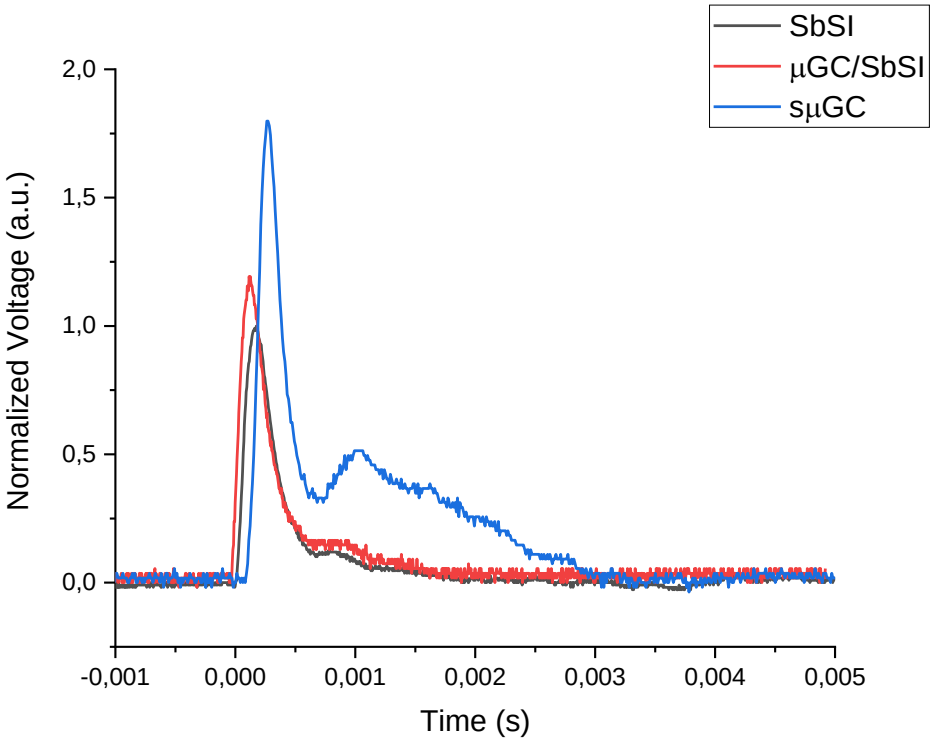

Figure 60 Results of output voltage comparison of composite at pressure 17.03 bar

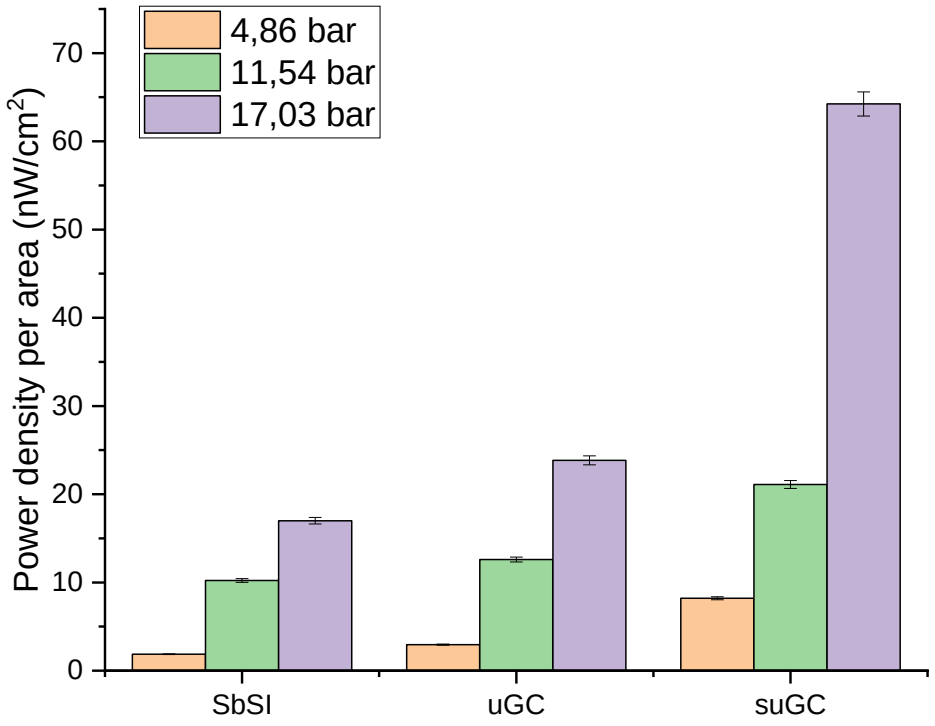

Figure 61 Results of power density per area of investigated composites

The hypothetic advantageous situation is for the power generated by the entire volume of the piezoelectric sample after applying stress to it. In such situation, the voltage should be the same for all tested samples. However, due to the high resistivity of the matrix in tested composites, charges cannot conduct through it. Due to the poor conductivity of HDPE, some part of power generated by the nanowires is lost. However, by enhancing the matrix conductivity with conductive particles, more charges generated by SbSI can be transferred though the matrix. This can be represented as an increase in the layer depth in which generated charges can be transferred outside to the electrodes and used. Thus, the increase in conductivity should be related to power generated by the composite sample. As the conductivity tests have shown, the sμGC reinforcement improves conduction in HDPE composites much better than μGC does. This might explain the increase in output voltage during piezoelectric tests, hence power generated by composites containing GC. Moreover, this also explains the better performance of composites with sμGC. The model presenting the proposed phenomena is presented in Fig. 62.

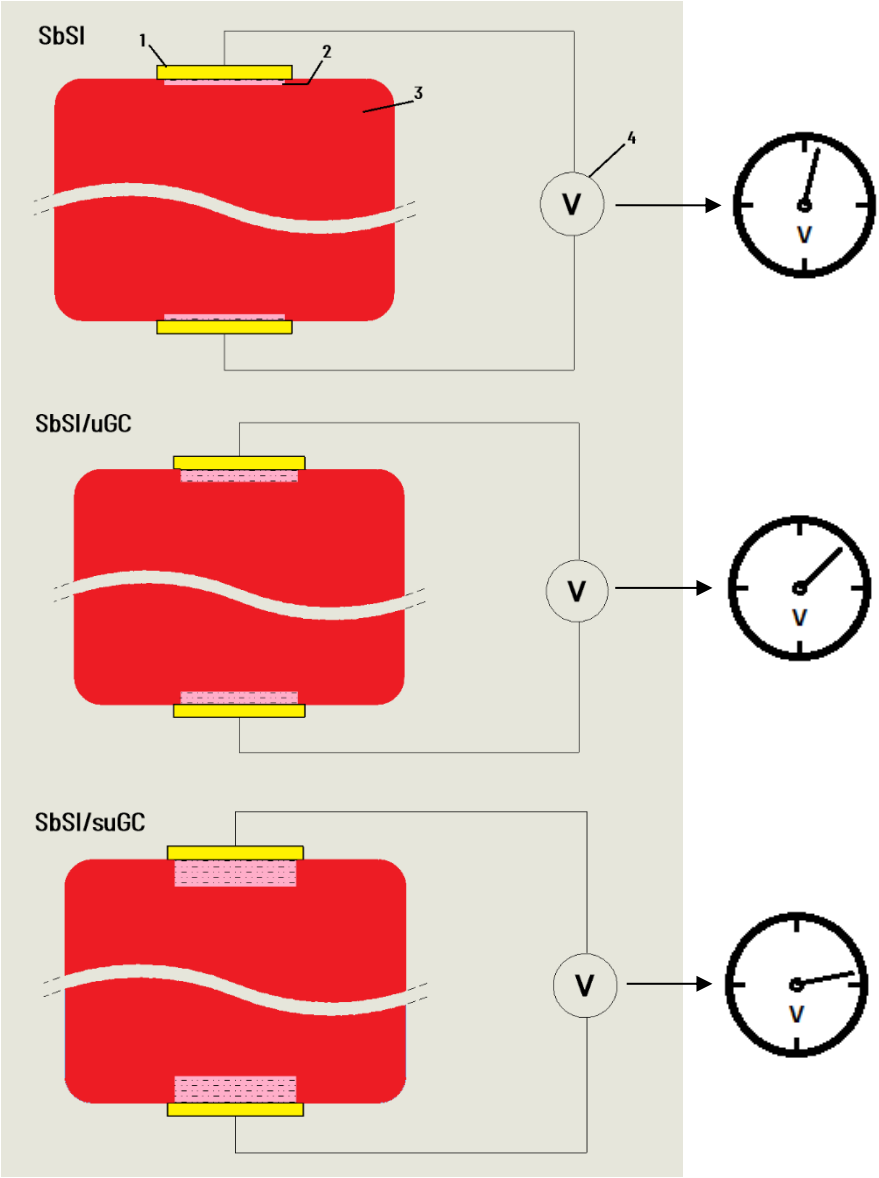

Figure 62 Schema of proposed piezoelectric layer depth change mechanism for investigated composites: 1 – gold electrode, 2 – layer of generated power, 3 – sample body, 4 – voltmeter

4 Summary and Conclusions

The investigation on HDPE matrix composites filled with glassy carbon was performed. The glassy carbon improved mechanical strength, enhanced the electric conductivity and wear resistance of the polymer matrix. However, depending on potential application a different GC grain size should be used. Due to difference in milling procedure, obtaining sμGC requires more energy than fabrication of μGC (occurs more costly in practice). In applications that require wear resistance or self-lubricating properties, the μGC perform as good as sμGC, so there is no need to use the reinforcement which is potentially more expensive. However, in application that require high conductivity or at least antistatic properties, the advantage of using sμGC over μGC is obvious. Due to smaller grain size, it can be distributed more evenly within the matrix, which leads to shorter percolation path and hence higher conductivity.

The performance of glassy carbon in heterophase (hybrid) composites as a secondary reinforcement was investigated. Depending on desired properties different grain size of GC can be used. In composite with n-Al_2O_3, GC can stabilize a friction coefficient and decrease mass wear rate of the composite. This is due to self-lubricating properties of GC. As mentioned above due to lack of significant difference in performance of composites containing μGC and sμGC, the more accessible is advised. In case of piezoelectric composites with SbSI, the use of sμGC can lead to significant increase in piezoelectric response - power generated by the composite during loading. This gives a potential for both energy harvesting elements and strain sensors.

The performed research can be summarized with seven main conclusions:

1. Developed and applied technological parameters allowed to obtain efficiently both HDPE/GC composite filaments and final elements by FDM 3D printing. That confirmed the dissertation thesis.
2. The addition of glassy carbon particles affects matrix crystallization and impede movement ease of polymer chains. It results in smaller crystallites and higher mechanical strength of the composites in comparison with neat HDPE.
3. The difference in the performance of the composites is dependent on the size of glassy carbon particles. The micrometric glassy carbon (μGC) had a higher impact on mechanical strength than submicrometric glassy carbon (sμGC). Additionally, no significant difference in performance during friction was observed.

4. Due to differences in particle size, the submicrometric glassy carbon increases the conductivity of the HDPE matrix more than the micrometric glassy carbon.
5. The addition of glassy carbon to composites with nano-alumina results in a decrease in wear rate and the stabilization of the coefficient of friction over distances. The glassy carbon particles size does not impact these effects significantly.
6. The HDPE composites with antimony sulfoiodide (SbSI) exhibit good dispersion of nanowire within polymer matrix. The addition of glassy carbon to the composites results in the increase in piezoelectric output voltage and piezoelectric power per area. An over 8-fold increase in generated power was observed for the composite containing submicrometric glassy carbon.
7. The obtained composites proved to be usable in FDM 3D printing technology. This makes a real potential for 3D printed parts for biomedical applications, wear resistance applications or strain sensors.

5 Literature

[1] V. Uskoković, “A historical review of glassy carbon: Synthesis, structure, properties and applications,” *Carbon Trends*, vol. 5. Elsevier Ltd, Oct. 01, 2021. doi: 10.1016/j.cartre.2021.100116.

[2] S. YAMADA and H. SATO, “Some Physical Properties of Glassy Carbon,” *Nature*, vol. 193, no. 4812, pp. 261–262, Jan. 1962, doi: 10.1038/193261b0.

[3] S. Sharma, “Glassy Carbon: A promising material for microand nanomanufacturing,” *Materials*, vol. 11, no. 10. MDPI AG, Sep. 28, 2018. doi: 10.3390/ma11101857.

[4] P. J. F. Harris, “New Perspectives on the Structure of Graphitic Carbons,” *Critical Reviews in Solid State and Materials Sciences*, vol. 30, no. 4, pp. 235–253, Oct. 2005, doi: 10.1080/10408430500406265.

[5] P. J. F. Harris, “Structure of non-graphitising carbons,” *International Materials Reviews*, vol. 42, no. 5, pp. 206–218, Sep. 1997, doi: 10.1179/imr.1997.42.5.206.

[6] M. Hokao, S. Hironaka, Y. Suda, and Y. Yamamoto, “Friction and wear properties of graphite/glassy carbon composites,” *Wear*, vol. 237, no. 1, pp. 54–62, Jan. 2000, doi: 10.1016/S0043-1648(99)00306-3.

[7] J. C. Lewis and F. C. Cowlard, “VITREOUS CARBON AS A CRUCIBLE MATERIAL FOR SEMICONDUCTORS,” Slate Electronics Pergamon Press, 1963.

[8] J. A. Katerberg and A. C. Anderson, “Low-Temperature Specific Heat, Thermal Conductivity, and Ultrasonic Velocity of Glassy Carbons*,” 1978.

[9] L. A. Pesin, “Review Structure and properties of glass-like carbon,” *J Mater Sci*, vol. 37, pp. 1–28, 2002, doi: 10.1023/A:1013100920130.

[10] M. W. Williams and E. T. Arakawa, “Optical properties of glassy carbon from 0 to 82 eV,” *J Appl Phys*, vol. 43, no. 8, pp. 3460–3463, 1972, doi: 10.1063/1.1661738.

[11] W. Sarna, “RVC - reticulated vitreous carbon. Structure, precursor polymer materials, process of manufacturing and applications,” *INŻYNIERIA MATERIAŁOWA*, vol. 1, no. 2, pp. 35–47, Apr. 2016, doi: 10.15199/28.2016.2.6.

[12] F. D. Origo *et al.*, “Acid catalyst influence on the polymerization time of polyfurfuryl alcohol and on the porosity of monolithic vitreous carbon,” *J Appl Polym Sci*, vol. 133, no. 20, May 2016, doi: 10.1002/app.43272.

[13] E. G. R. dos Anjos *et al.*, “Processing and characterization of polypropylene (PP)/ethylene–vinyl acetate (EVA) blend-based glassy carbon (GC) composites,” *SN Appl Sci*, vol. 2, no. 8, p. 1381, Aug. 2020, doi: 10.1007/s42452-020-3190-5.

[14] K. Tadyszak, J. Litowczenko, Ł. Majchrzycki, P. Jeżowski, K. Załęski, and B. Scheibe, “Sucrose based cellular glassy carbon for biological applications,” *Mater Chem Phys*, vol. 239, Jan. 2020, doi: 10.1016/j.matchemphys.2019.122033.

[15] J. Myalski and B. Hekner, “GLASSY CARBON FOAMS AS SKELETON REINFORCEMENT IN POLYMER COMPOSITE,” *Composites Theory and Practice*, vol. 17, pp. 41–46, 2017.

[16] Y. A. Levendis and R. C. Flagan, “SYNTHESIS, FORMATION AND CHARACTERIZATION OF MICRON-SIZED GLASSY CARBON SPHERES OF CONTROLLED PORE STRUCTURE,” 1989.

[17] I. C. Oyama, G. P. M. Souza, M. C. Rezende, L. S. Montagna, and F. R. Passador, “A new eco-friendly green composite for antistatic packaging: Green low-density polyethylene/glassy carbon,” *Polym Compos*, vol. 41, no. 7, pp. 2744–2752, Jul. 2020, doi: 10.1002/pc.25572.

[18] A. Olszówka-Myalska, J. Myalski, and A. Botor-Probierz, “Effect of glassy carbon particles on wear resistance of AZ91E matrix composite,” *Solid State Phenomena*, vol. 176, pp. 127–138, Jun. 2011, doi: 10.4028/www.scientific.net/SSP.176.127.

[19] M. S. dos Santos, L. S. Montagna, M. C. Rezende, and F. R. Passador, “A new use for glassy carbon: Development of LDPE/glassy carbon composites for antistatic packaging applications,” *J Appl Polym Sci*, vol. 136, no. 11, p. 47204, Mar. 2019, doi: 10.1002/app.47204.

[20] L. de S. Vieira, “A review on the use of glassy carbon in advanced technological applications,” *Carbon N Y*, vol. 186, pp. 282–302, Jan. 2022, doi: 10.1016/j.carbon.2021.10.022.

[21] “Scopus.” Accessed: Jul. 23, 2023. [Online]. Available: https://www.scopus.com/results/results.uri?sort=plf-f&src=s&st1=HDPE&st2=carbon&sid=c76bb75f77003bb65d03b9b3eb2868ac&sot=b&sdt=b&sl=27&s=%28KEY%28HDPE%29+AND+KEY%28carbon%29%29&origin=searchbasic&editSaveSearch=&yearFrom=2000&yearTo=Present&sessionSearchId=c76bb75f77003bb65d03b9b3eb2868ac&limit=10

[22] E. Zittel and F. J. Miller, “A Glassy-Carbon Electrode for Voltammetry.”

[23] M. Wala, D. Łubiarz, N. Waloszczyk, and W. Simka, “Plasma Electrolytic Oxidation of Titanium in Ni and Cu Hydroxide Suspensions towards Preparation of Electrocatalysts for Urea Oxidation,” *Materials*, vol. 16, no. 6, p. 2191, Mar. 2023, doi: 10.3390/ma16062191.

[24] Y. Yi *et al.*, “Electrochemical corrosion of a glassy carbon electrode,” *Catal Today*, vol. 295, pp. 32–40, Oct. 2017, doi: 10.1016/j.cattod.2017.07.013.

[25] I. Matijašević, M. Kulizić, L. Bacetić, D. Gavrilović, R. Baošić, and A. Lolić, “Polyglycine Modified Glassy Carbon Electrode for Ibuprofen Determination,” *ChemistrySelect*, vol. 8, no. 24, Jun. 2023, doi: 10.1002/slct.202300827.

[26] K. Promsuwan *et al.*, “Polyaniline-coated glassy carbon microspheres decorated with nano-palladium as a new electrocatalyst for methanol oxidation,” *Journal of Electroanalytical Chemistry*, vol. 928, p. 116995, Jan. 2023, doi: 10.1016/j.jelechem.2022.116995.

[27] J. Vazquez-Samperio, P. Acevedo-Peña, A. Guzmán-Vargas, E. Reguera, and E. Cordoba-Tuta, “Incorporation of heteroatoms into reticulated vitreous carbon foams derived from sucrose to improve its energy storage performance,” *Int J Energy Res*, vol. 45, no. 4, pp. 6383–6394, Mar. 2021, doi: 10.1002/er.6193.

[28] P. Choryłek, “Vertebroplasty and kyphoplasty – advantages and disadvantages used bone cement of PMMA,” *Journal of Achievements in Materials and Manufacturing Engineering*, vol. 1–2, no. 92, pp. 36–49, Jan. 2019, doi: 10.5604/01.3001.0013.3186.

[29] N. T. Acuña, V. Güiza-Argüello, and E. Córdoba-Tuta, “Reticulated Vitreous Carbon Foams from Sucrose: Promising Materials for Bone Tissue Engineering Applications,” *Macromol Res*, vol. 28, no. 10, pp. 888–895, Sep. 2020, doi: 10.1007/s13233-020-8128-7.

[30] R. Mishra, B. Pramanick, T. K. Maiti, and T. K. Bhattacharyya, “Glassy carbon microneedles—new transdermal drug delivery device derived from a scalable C-MEMS process,” *Microsyst Nanoeng*, vol. 4, no. 1, p. 38, Dec. 2018, doi: 10.1038/s41378-018-0039-9.

[31] M. HOKAO and S. HIRONAKA, “Friction Properties of Cluster Diamond/Glassy Carbon Composites.,” *Journal of the Ceramic Society of Japan*, vol. 108, no. 1263, pp. 979–984, 2000, doi: 10.2109/jcersj.108.1263_979.

[32] M. Godzierz and A. Olszówka-Myalska, “INFLUENCE OF CASTING PROCEDURE ON WEAR OF MAGNESIUM MATRIX COMPOSITES REINFORCED WITH CARBON OPEN-CELLED FOAM,” *Composites Theory and Practice*, vol. 19, no. 2, pp. 64–70, 2019.

[33] A. Olszówka-Myalska, J. Myalski, and B. Hekner, “Tribological Characteristics of the Magnesium Matrix-Glassy Carbon Particles Composite Manufactured by Different Casting Methods,” *Conference Papers in Science*, vol. 2015, pp. 1–8, May 2015, doi: 10.1155/2015/919308.

[34] A. Olszówka-Myalska, J. Myalski, M. Godzierz, and P. Wrześniowski, “Magnesium matrix composite with open-celled carbon foams obtained by powder metallurgy,” *Archives of Metallurgy and Materials*, vol. 63, no. 2, pp. 825–831, 2018, doi: 10.24425/122409.

[35] A. Olszówka-Myalska, M. Godzierz, J. Myalski, and P. Wrześniowski, “Magnesium Matrix Composite with Open-Celled Glassy Carbon Foam Obtained Using the Infiltration Method,” *Metals (Basel)*, vol. 9, no. 6, p. 622, May 2019, doi: 10.3390/met9060622.

[36] A. Posmyk and J. Myalski, “COMPOSITES INCLUDING FOAM INSERTS DESIGNED FOR COMBUSTION ENGINE CYLINDER LINERS,” *Composites Theory and Practice*, vol. 17, pp. 25–29, 2017, Accessed: Jul. 13, 2023. [Online]. Available: https://kompozyty.ptmk.net/pliczki/pliki/5_2017_t1_Posmyk.pdf

[37] A. Posmyk, J. Myalski, and H. Wistuba, “Properties of Aluminium-Ceramic Composite with Glassy Carbon as Solid Lubricant Designed for Automotive Applications / Właściwości Kompozytu Aluminiowo Ceramicznego Zawierajacego Węgiel Szklisty

Jako Smar Stały Przeznaczonego Dla Motoryzacji," *Archives of Metallurgy and Materials*, vol. 60, no. 4, pp. 2573–2578, Dec. 2015, doi: 10.1515/amm-2015-0416.

[38] J. MYALSKI, A. Posmyk, B. HEKNER, and M. GODZIERZ, "THE INFLUENCE OF GLASSY CARBON AND ITS FORMS ON TRIBOLOGICAL PROPERTIES OF ALUMINIUM MATRIX COMPOSITES," *Tribologia*, vol. 285, no. 3, pp. 79–87, Jun. 2019, doi: 10.5604/01.3001.0013.5437.

[39] A. Posmyk, J. Myalski, and B. Hekner, "Glassy Carbon Coating Deposited on Hybrid Structure of Composite Materials," *Archives of Metallurgy and Materials*, vol. 61, no. 2, pp. 1045–1050, Jun. 2016, doi: 10.1515/amm-2016-0176.

[40] B. Juszczyk, J. Kulasa, W. Malec, S. Malara, M. Czepelak, and L. Ciura, "Microstructure and tribological properties of the copper matrix composite materials containing lubricating phase particles," *Archives of Metallurgy and Materials*, vol. 59, no. 1, pp. 365–369, 2014, doi: 10.2478/amm-2014-0061.

[41] M. Kumar and V. Sharma, "3D printed bio-ceramic loaded PEGDA/vitreous carbon composite: Fabrication, characterization, and life cycle assessment," *J Mech Behav Biomed Mater*, vol. 143, p. 105904, Jul. 2023, doi: 10.1016/j.jmbbm.2023.105904.

[42] U. Szeluga *et al.*, "Influence of unique structure of glassy carbon on morphology and properties of its epoxy-based binary composites and hybrid composites with carbon nanotubes," *Compos Sci Technol*, vol. 134, pp. 72–80, Oct. 2016, doi: 10.1016/j.compscitech.2016.08.004.

[43] S. Pusz, U. Szeluga, B. Kumanek, S. Czajkowska, and J. Myalski, "Morphology and thermo-mechanical properties of epoxy composites with glassy carbon," in *14th International Multidisciplinary Scientific Geoconference (SGEM)*, Jun. 2014.

[44] J. Myalski *et al.*, "Glassy Carbon Open-Celled Foams as a Reinforcement in Polymer Matrix Composites Dedicated for Tribological Applications," *Materials*, vol. 16, no. 5, Mar. 2023, doi: 10.3390/ma16051805.

[45] P. Olesik, M. Kozioł, and J. Jała, "PROCESSING AND STRUCTURE OF HDPE/GLASSY CARBON COMPOSITE SUITABLE FOR 3D PRINTING," *Composite Theory and Practice*, vol. 20, no. 2, pp. 72–77, 2020.

[46] J. Myalski, M. Godzierz, and P. Olesik, “Effect of Carbon Fillers on the Wear Resistance of PA6 Thermoplastic Composites,” *Polymers (Basel)*, vol. 12, no. 10, p. 2264, Oct. 2020, doi: 10.3390/polym12102264.

[47] L. de Souza Vieira, L. S. Montagna, J. Marini, and F. R. Passador, “Influence of particle size and glassy carbon content on the thermal, mechanical, and electrical properties of PHBV/glassy carbon composites,” *J Appl Polym Sci*, vol. 138, no. 4, Jan. 2021, doi: 10.1002/app.49740.

[48] P. Olesik, M. Godzierz, M. Kozioł, J. Jała, U. Szeluga, and J. Myalski, “Structure and Mechanical Properties of High-Density Polyethylene Composites Reinforced with Glassy Carbon,” *Materials*, vol. 14, no. 14, p. 4024, Jul. 2021, doi: 10.3390/ma14144024.

[49] A. Posmyk and J. Myalski, “Coatings protecting against aviation piston engine seizure,” *Wear*, vol. 518–519, Apr. 2023, doi: 10.1016/j.wear.2023.204627.

[50] K. M. Seven, J. M. Cogen, and J. F. Gilchrist, “Nucleating agents for high-density polyethylene - A review,” *Polym Eng Sci*, vol. 56, no. 5, pp. 541–554, May 2016, doi: 10.1002/pen.24278.

[51] S. Nath, S. Bodhak, and B. Basu, “HDPE-Al2O3-HAp composites for biomedical applications: Processing and characterizations,” *J Biomed Mater Res B Appl Biomater*, vol. 88, no. 1, pp. 1–11, Jan. 2009, doi: 10.1002/jbm.b.31050.

[52] A. U. Chaudhry, S. P. Lonkar, R. G. Chudhary, A. Mabrouk, and A. A. Abdala, “Thermal, electrical, and mechanical properties of highly filled HDPE/graphite nanoplatelets composites,” in *Materials Today: Proceedings*, Elsevier Ltd, 2019, pp. 704–708. doi: 10.1016/j.matpr.2020.04.168.

[53] J. Pelto *et al.*, “Matrix morphology and the particle dispersion in HDPE nanocomposites with enhanced wear resistance,” *Polym Test*, vol. 77, Aug. 2019, doi: 10.1016/j.polymertesting.2019.105897.

[54] Y. Jamal Mahboba and M. Abdullah Al-Shammari, “Enhancing wear rate of high-density polyethylene (HDPE) by adding ceramic particles to propose an option for artificial hip joint liner,” in *IOP Conference Series: Materials Science and Engineering*, Institute of Physics Publishing, Nov. 2019. doi: 10.1088/1757-899X/561/1/012071.

[55] C. Dong, C. Yuan, X. Bai, and Y. Tian, “A novel approach to reduce deformation behaviors of HDPE polymer during friction,” *Appl Surf Sci*, vol. 503, Feb. 2020, doi: 10.1016/j.apsusc.2019.144311.

[56] S. Paszkiewicz, K. Pypeć, I. Irska, and E. Piesowicz, “Functional Polymer Hybrid Nanocomposites Based on Polyolefins: A Review,” *Processes*, vol. 8, no. 11, p. 1475, Nov. 2020, doi: 10.3390/pr8111475.

[57] X. Liang, Z. Guo, T. Jun, and C. Yuan, “Effect of modified glass fiber on tribological performance of water-lubricated bearing,” *Polym Test*, vol. 81, Jan. 2020, doi: 10.1016/j.polymertesting.2019.106153.

[58] A. Salem, W. Bensalah, and S. Mezlini, “Effect of hygrothermal aging on the tribological behavior of HDPE composites for bio-implant application,” *Polym Test*, vol. 94, Feb. 2021, doi: 10.1016/j.polymertesting.2020.107050.

[59] K. Mazur, P. Jakubowska, P. Romańska, and S. Kuciel, “Green high density polyethylene (HDPE) reinforced with basalt fiber and agricultural fillers for technical applications,” *Compos B Eng*, vol. 202, p. 108399, Dec. 2020, doi: 10.1016/j.compositesb.2020.108399.

[60] H. Kaczmarek, B. Królikowski, M. Chylińska, E. Klimiec, and D. Bajer, “Piezoelectric Films Based on Polyethylene Modified by Aluminosilicate Filler,” *Polymers (Basel)*, vol. 11, no. 8, p. 1345, Aug. 2019, doi: 10.3390/polym11081345.

[61] A. M. Reda, A. A. Azab, and G. M. Turky, “Gamma-ray shielding, electrical, and magnetic properties of α-Fe $_2$ O $_3$ /Al/HDPE nanocomposites,” *Phys Scr*, vol. 97, no. 9, p. 095303, Sep. 2022, doi: 10.1088/1402-4896/ac8458.

[62] S. Sanchez-Valdes, “Influence of maleated elastomer on filler dispersion, mechanical and antimicrobial properties of hybrid HDPE/clay/silver nanocomposites,” *J Adhes Sci Technol*, vol. 30, no. 9, pp. 1006–1016, May 2016, doi: 10.1080/01694243.2015.1136136.

[63] S. Paszkiewicz, A. Szymczyk, D. Pawlikowska, J. Subocz, M. Zenker, and R. Masztak, “Electrically and thermally conductive low density polyethylene-based nanocomposites reinforced by MWCNT or hybrid MWCNT/graphene nanoplatelets with improved thermo-oxidative stability,” *Nanomaterials*, vol. 8, no. 4, Apr. 2018, doi: 10.3390/nano8040264.

[64] E. Tarani, I. Arvanitidis, D. Christofilos, D. N. Bikiaris, K. Chrissafis, and G. Vourlias, “Calculation of the degree of crystallinity of HDPE/GNPs nanocomposites by using various experimental techniques: a comparative study,” *J Mater Sci*, vol. 58, no. 4, pp. 1621–1639, Jan. 2023, doi: 10.1007/s10853-022-08125-4.

[65] S. Dabees, V. Tirth, A. Mohamed, and B. M. Kamel, “Wear performance and mechanical properties of MWCNT/HDPE nanocomposites for gearing applications,” *Journal of Materials Research and Technology*, vol. 12. Elsevier Editora Ltda, pp. 2476–2488, 2021. doi: 10.1016/j.jmrt.2020.09.129.

[66] N. Faisal, “Mechanical behavior of nano-scaled graphene oxide reinforced high-density polymer ethylene for orthopedic implants,” *Biointerface Res Appl Chem*, vol. 10, no. 6, pp. 7223–7233, Dec. 2020, doi: 10.33263/BRIAC106.72237233.

[67] L. Zhang, C. Dong, C. Yuan, X. Bai, and Y. Tian, “The role of graphene nanoplatelets in the friction reducing process of polymer,” *Polym Compos*, vol. 43, no. 11, pp. 8213–8227, Nov. 2022, doi: 10.1002/pc.26991.

[68] S. Xu *et al.*, “Wear of carbon nanofiber reinforced HDPE nanocomposites under dry sliding condition,” *J Nanotechnol Eng Med*, vol. 3, no. 4, Nov. 2012, doi: 10.1115/1.4023244.

[69] S. Xu and X. W. Tangpong, “Review: Tribological behavior of polyethylene-based nanocomposites,” *Journal of Materials Science*, vol. 48, no. 2. Springer New York LLC, pp. 578–597, Jan. 01, 2013. doi: 10.1007/s10853-012-6844-x.

[70] G. Wu, J. Lin, Q. Zheng, and M. Zhang, “Correlation between percolation behavior of electricity and viscoelasticity for graphite filled high density polyethylene,” *Polymer (Guildf)*, vol. 47, no. 7, pp. 2442–2447, Mar. 2006, doi: 10.1016/j.polymer.2006.02.017.

[71] L. T. Hoang, M. Aghelinejad, S. N. Leung, and Z. H. Zhu, “High Density Polyethylene/Carbon Nanotube Nanocomposite Foams: Electrical Conductivity And Percolation Threshold,” in *Proceedings of The Canadian Society for Mechanical Engineering International Congress 2018 CSME International Congress 2018*, York University Libraries, May 2018. doi: 10.25071/10315/35413.

[72] Y. Mamunya *et al.*, “Pyroresistive Properties of Composites Based on HDPE and Carbon Fillers,” *Polymers (Basel)*, vol. 15, no. 9, p. 2105, Apr. 2023, doi: 10.3390/polym15092105.

[73] T. D. Ngo, A. Kashani, G. Imbalzano, K. T. Q. Nguyen, and D. Hui, "Additive manufacturing (3D printing): A review of materials, methods, applications and challenges," *Composites Part B: Engineering*, vol. 143. Elsevier Ltd, pp. 172–196, Jun. 15, 2018. doi: 10.1016/j.compositesb.2018.02.012.

[74] A. Haryńska *et al.*, "A comprehensive evaluation of flexible FDM/FFF 3D printing filament as a potential material in medical application," *Eur Polym J*, vol. 138, Sep. 2020, doi: 10.1016/j.eurpolymj.2020.109958.

[75] E. R. Cholleti, "A Review on 3D printing of piezoelectric materials," in *IOP Conference Series: Materials Science and Engineering*, Institute of Physics Publishing, Dec. 2018. doi: 10.1088/1757-899X/455/1/012046.

[76] C. G. Schirmeister, T. Hees, E. H. Licht, and R. Mülhaupt, "3D printing of high density polyethylene by fused filament fabrication," *Addit Manuf*, vol. 28, pp. 152–159, Aug. 2019, doi: 10.1016/j.addma.2019.05.003.

[77] E. Barba, J. B. Mietner, and J. R. G. Navarro, "Grafting of poly(stearyl acrylate) on cellulose fibers as 3D-printable HDPE composites," *Cellulose*, vol. 30, no. 4, pp. 2267–2278, Mar. 2023, doi: 10.1007/s10570-022-05021-7.

[78] N. Vidakis, M. Petousis, A. Maniadi, V. Papadakis, and A. Manousaki, "MEX 3D Printed HDPE/TiO2 Nanocomposites Physical and Mechanical Properties Investigation," *Journal of Composites Science*, vol. 6, no. 7, Jul. 2022, doi: 10.3390/jcs6070209.

[79] S. Kumar, M. R. Ramesh, M. Doddamani, S. M. Rangappa, and S. Siengchin, "Mechanical characterization of 3D printed MWCNTs/HDPE nanocomposites," *Polym Test*, vol. 114, Oct. 2022, doi: 10.1016/j.polymertesting.2022.107703.

[80] T. B. Freeman, M. A. Messenger, C. J. Troxler, K. Nawaz, R. M. Rodriguez, and S. K. S. Boetcher, "Fused filament fabrication of novel phase-change material functional composites," *Addit Manuf*, vol. 39, p. 101839, Mar. 2021, doi: 10.1016/j.addma.2021.101839.

[81] D. J. Horst, P. P. de Andrade Junior, C. A. Duvoisin, and R. de A. Vieira, "Fabrication of conductive filaments for 3d-printing: Polymer nanocomposites," *Biointerface Res Appl Chem*, vol. 10, no. 6, pp. 6577–6586, Dec. 2020, doi: 10.33263/BRIAC106.65776586.

[82] S. V. Panin, D. G. Buslovich, Y. V. Dontsov, S. A. Bochkareva, L. A. Kornienko, and F. Berto, “UHMWPE-Based Glass-Fiber Composites Fabricated by FDM. Multiscaling Aspects of Design, Manufacturing and Performance,” *Materials*, vol. 14, no. 6, p. 1515, Mar. 2021, doi: 10.3390/ma14061515.

[83] S. V. Panin *et al.*, “Comparative Analysis of Tribological and Mechanical Properties of Extrudable Polymer–Polymer UHMWPE Composites Fabricated by 3D Printing and Hot-Pressing Methods,” *Journal of Friction and Wear*, vol. 41, no. 3, pp. 228–235, May 2020, doi: 10.3103/S1068366620030125.

[84] P. Parsons, Z. Larimore, F. Muhammed, and M. Mirotznik, “Fabrication of low dielectric constant composite filaments for use in fused filament fabrication 3D printing,” *Addit Manuf*, vol. 30, p. 100888, Dec. 2019, doi: 10.1016/j.addma.2019.100888.

[85] A. S. Bhalla, R. E. Newnham, T. R. Shrout, and L. E. Cross, “Piezoelectric Sbsi: Polymer Composites,” *Ferroelectrics*, vol. 41, no. 1, pp. 207–211, May 1982, doi: 10.1080/00150198208210625.

[86] M. Nowak *et al.*, “Using of sonochemically prepared SbSI for electrospun nanofibers,” *Ultrason Sonochem*, vol. 38, pp. 544–552, Sep. 2017, doi: 10.1016/j.ultsonch.2017.03.042.

[87] B. Toroń, P. Szperlich, and M. Kozioł, “SbSI Composites Based on Epoxy Resin and Cellulose for Energy Harvesting and Sensors—The Influence of SBSI Nanowires Conglomeration on Piezoelectric Properties,” *Materials*, vol. 13, no. 4, p. 902, Feb. 2020, doi: 10.3390/ma13040902.

[88] M. Kozioł, B. Toroń, P. Szperlich, and M. Jesionek, “Fabrication of a piezoelectric strain sensor based on SbSI nanowires as a structural element of a FRP laminate,” *Compos B Eng*, vol. 157, pp. 58–65, Jan. 2019, doi: 10.1016/j.compositesb.2018.08.105.

[89] L. G. Austin and P. Bagga, “An analysis of fine dry grinding in ball mills,” *Powder Technol*, vol. 28, no. 1, pp. 83–90, Jan. 1981, doi: 10.1016/0032-5910(81)87014-3.

[90] K. J. Wilczynski, “Wyznaczanie krzywych lepkosci polimerowych kompozytów drzewnych na podstawie ograniczonej liczby pomiarów reometrycznych,” *Polimery/Polymers*, vol. 63, no. 3, pp. 213–218, Mar. 2018, doi: 10.14314/polimery.2018.3.5.

[91] P. Olesik, M. Godzierz, and M. Kozioł, “Preliminary Characterization of Novel LDPE-Based Wear-Resistant Composite Suitable for FDM 3D Printing,” *Materials*, vol. 12, no. 16, p. 2520, Aug. 2019, doi: 10.3390/ma12162520.

[92] K. Mistewicz *et al.*, “Determination of electrical conductivity type of SbSI nanowires,” *Mater Lett*, vol. 182, pp. 78–80, Nov. 2016, doi: 10.1016/j.matlet.2016.06.073.

[93] B. Toroń, P. Szperlich, M. Nowak, and A. Starczewska, “A novel method for measuring piezoelectric coefficients,” *Measurement (Lond)*, vol. 206, Jan. 2023, doi: 10.1016/j.measurement.2022.112274.

Attachment 1 List of Figures

Attachement 2 List of Tables

Attachement 3 Academic achievements

1. Khan, M. J., Moskal, G., Iqbal, A., Mikuśkiewicz, M., Pawlik, T., & Olesik, P. (2023). Hot corrosion behavior of single-layered Gd2Zr2O7, Sm2Zr2O7, and Nd2Zr2O7 thermal barrier coatings exposed to Na2SO4 + MgSO4 environment. Coatings, 13, 1–14. https://doi.org/10.3390/coatings13081311
2. Godzierz, M., Olesik, P., Otulakowski, Ł., Pawlik, T., Olszowska, K., Chaber, P., Masiuchok, O., Myalska-Głowacka, H., Smoleń, J., Toroń, B., Szperlich, P., Szeluga, U., & Pusz, S. (2022). Facile and highly efficient wet synthesis of nanocrystalline $BiFeOC_3$ particles by reverse co-precipitation method. Ceramics International, 49, 12126–12137. https://doi.org/10.1016/j.ceramint.2022.12.064
3. Godzierz, M., Toroń, B., Szperlich, P., Olesik, P., & Kozioł, M. (2022). X-ray diffraction and piezoelectric studies during tensile stress on epoxy/SbSI nanocomposite. Sensors, 22, 1–14. https://doi.org/10.3390/s22103886
4. Olesik, P., Stępień, K., Peryt, A., Siejka, P., Waluś, S., Witczak, W., Wójcik, K., & Wolanin, A. (2022). Selected properties of polypropylene-BaSO4 composites after UV exposure. Composites Theory and Practice, 22, 50–53.
5. Olesik, P., Peryt, A., Stępień, K., Frączek, V., Mackiewicz, K., Molka, W., Musiał, O., Różańska, W., & Jesionek, M. (2022). Selected properties of polypropylene-TiO2 composites after exposure to UV rays - preliminary study. Composites Theory and Practice, 22, 21–24.
6. Smoleń, J., Olesik, P., Jała, J., Adamcio, A., Kurtyka, K., Godzierz, M., Kozera, R., Kozioł, M., & Boczkowska, A. (2022). The use of carbon fibers recovered by pyrolysis from end-of-life wind turbine blades in epoxy-based composite panels. Polymers, 14, 1–14. https://doi.org/10.3390/polym14142925
7. Nowacki, B., Kowol, P., Kozioł, M., Olesik, P., Wieczorek, J., & Wacławiak, K. (2021). Effect of post-process curing and washing time on mechanical properties of mSLAPrintouts. Materials, 14, 1–14. https://doi.org/10.3390/ma14174856
8. Olesik, P., Godzierz, M., Kozioł, M., Jała, J., Szeluga, U., & Myalski, J. (2021). Structure and mechanical properties of high-density polyethylene composites reinforced with glassy carbon. Materials, 14, 1–10. https://doi.org/10.3390/ma14144024
9. Smoleń, J., Olesik, P., Jała, J., Myalska, H., Godzierz, M., & Kozioł, M. (2021). Application of mathematical and experimental approach in description of sedimentation of powder fillers in epoxy resin. Materials, 14, 1–15. https://doi.org/10.3390/ma14247520

10. Smoleń, J., Olesik, P., Gradoń, P., Chudy, M., Mendala, B., & Kozioł, M. (2021). The use of the ATD technique to measure the gelation time of epoxy resins. Materials, 14, 1–12. https://doi.org/10.3390/ma14206022
11. Smoleń, J., Godzierz, M., Olesik, P., Pawlik, T., & Kozioł, M. (2021). Utilization of CFRP waste as a filler in polyester resin-based composites. Journal of Composite Materials, 55, null. https://doi.org/10.1177/0021998321999098
12. Kozioł, M., Szperlich, P., Toroń, B., Olesik, P., & Jesionek, M. (2020). Assessment of the piezoelectric response of an epoxy resin/SbSInanowires composite filling FDM printed grid. Materials, 13, 1–14. https://doi.org/10.3390/ma13225281
13. Kozioł, M., Żuczek, N., Olesik, P., & Wieczorek, J. (2020). Preliminary analysis of concept of producing polymer concrete surface for outdoor terraces. Composites Theory and Practice, 20, 102–110.
14. Kozłowski, M., Khater, G., Olesik, P., & Mahmoud, M. (2020). Preparation and characterization of lightweight glass-ceramics based on industrial wastes. Journal of the Australian Ceramic Society, 56, 11–20. https://doi.org/10.1007/s41779-019-00438-z
15. Myalski, J., Godzierz, M., & Olesik, P. (2020). Effect of carbon fillers on the wear resistance of PA6 thermoplastic composites. Polymers, 12, 1–14. https://doi.org/10.3390/polym12102264
16. Olesik, P., Kozioł, M., & Jała, J. (2020). Processing and structure of HDPE/glassy carbon composite suitable for 3D printing. Composites Theory and Practice, 20, 72–77.
17. Olesik, P., Godzierz, M., & Kozioł, M. (2019). Preliminary characterization of novel LDPE-based wear-resistant composite suitable for FDM 3D printing. Materials, 12, 1–19. https://doi.org/10.3390/ma12162520
18. Olesik, P., Kozioł, M., Konik, D., & Jała, J. (2019). The use of shredded car windscreen waste as reinforcement of thermoplastic composites for 3D (FDM) printing. Composites Theory and Practice, 19, 30–33.
19. Czerska, E., Olesik, P., & Wiśniewski, K. (2018). Tłumienie włókien szkło-ceramicznych współdomieszkowanych Er3+ i Yb3+. Materiały Ceramiczne, R. 70, 233–241.
20. Olesik, P., Kozioł, M., Toroń, B., & Szperlich, P. (2018). Preliminary evaluation of producing polymer cladding on glass fiber designated for fiber lasers. Composites Theory and Practice, 18, 140–144.